Disk Regrowth in E/S0 Galaxies and its Environmental Dependence

Amanda J. Moffett

A dissertation submitted to the faculty of the University of North Carolina at Chapel Hill in partial fulfillment of the requirements for the degree of Doctor of Philosophy in the Department of Physics and Astronomy.

Chapel Hill
2014

Approved by:

Sheila Kannappan

Bruce Carney

Gerald Cecil

Andreas Berlind

John Wilkerson

Fabian Heitsch

© 2014
Amanda J. Moffett
ALL RIGHTS RESERVED

ABSTRACT

Amanda J. Moffett: Disk Regrowth in E/S0 Galaxies and its Environmental Dependence
(Under the direction of Sheila Kannappan)

This work is focused on the investigation of observational evidence for the predicted "disk regrowth" process, which may allow spheroid-dominated E/S0 galaxies to rebuild spiral disks resembling that of the Milky Way Galaxy. By combining analysis of several complementary galaxy samples, we derive new observational constraints on the frequency, significance, and conditions of E/S0 disk regrowth.

We find that UV-detected disks, which represent recent star formation activity, are exceptionally common in low-mass E/S0 galaxies, and we define a new class of UV-Bright (UV-B) disk E/S0s that is associated with significant ($\gtrsim$10% by mass) recent disk growth, blue optical outer-disk colors, and enhanced atomic gas content. These UV-B disks are closely linked to a particular class of low-mass, optically blue E/S0s that were previously hypothesized to host active disk regrowth. The detection of UV-B disks around nearly all low-mass, blue E/S0s supports this picture and reinforces the potential importance of mass scales in the disk regrowth process. We also find that another type of mass scale, involving the mass of the group halo in which a galaxy resides, appears to play an important role in disk regrowth. Below a group halo mass of $\sim 10^{11.5} M_{\odot}$, blue E/S0s, gas-dominated galaxies, and UV-B disks all become more common, which may imply that such low group halo mass environments are important for allowing disk regrowth to proceed. This picture is consistent with both the variations of E/S0 and spiral galaxy frequency as a function of environment, with spiral galaxy frequencies rising at low group halo mass, and the observed similarity between typical environments of E/S0 and spiral galaxies at low baryonic mass ($\lesssim 10^{10} M_{\odot}$). Finally, we find direct evidence for secondary stellar disks in the kinematics of 6 out of 24 S0 galaxies for which we can confidently assess the presence or absence of secondary disks, but due to the small number of identifications, we cannot yet draw firm conclusions about any preference for specific mass, environment, or color regimes among such galaxies.

ACKNOWLEDGEMENTS

I thank my advisor, Sheila Kannappan, for her steadfast guidance and encouragement. Through Sheila's example, I have learned more than I could have imagined about conducting research and leading an ambitious project. I have also become an experienced observer under her watch, learning how to write a compelling case for my science and deal with the ups and downs of weather, instruments, and data reduction. Sheila's investment in the education of students and passion for bringing astronomy research to audiences outside of UNC is inspiring, and I hope to always follow her example in striving to ignite the scientific curiosity of potential young astronomers and members of the public.

I would like to thank the rest of my committee (Bruce Carney, Gerald Cecil, Andreas Berlind, John Wilkerson, and Fabian Heitsch) for their time spent considering and offering helpful feedback on this research as well. I acknowledge the assistance of a number of collaborators with specific parts of this work in the individual chapters, but more generally I would like to thank my long-term collaborators Andrew Baker and Andreas Berlind for their advice and support. I would also like to thank all of my office mates and allies in observing for their influence throughout the years (Kathleen Eckert, David Stark, Erik Hoversten, Mark Norris, Amy Gonzalez, and Jo Ellen McBride). You have all helped me make it to this point, if only by lending a sympathetic ear to voiced frustrations or providing much-needed entertainment on long observing nights spent peering at clouds. I have learned a great deal from our discussions. I thank Lisa Wei for sharing her experience with me as well.

I would also like to thank everyone at UNC involved with SOAR and its instruments for their efforts to develop and maintain the capabilities that benefit us all, particularly Chris Clemens and his group for their work on the Goodman Spectrograph. I thank Gerald Cecil, Sheila Kannappan, and Kurtis Keller for teaching me about instrument design through our efforts to build an ADC for Goodman. I thank the SOAR telescope operators for their hard work and long hours that make it possible for us to access our SOAR resources remotely.

I acknowledge funding support from several sources during the completion of this thesis: *GALEX* GI grants NNX07AT33G and NNX09AF69G, *Spitzer* GO grant 30406, a Sigma Xi Grant-In-Aid of

Research, the NASA Harriett G. Jenkins Pre-doctoral Fellowship, a North Carolina Space Grant, and the UNC Royster Society of Fellows Dissertation Completion Fellowship (specifically funded by Ed and Carol Smithwick).

On a more personal level, I want to thank my first astronomy teacher and research advisor, Beverly Smith, for encouraging my passion for astronomy and helping me realize that I can pursue this passion as a career. To my SO, Matt Brown, I thank you for the partnership and support that has extended throughout the majority of my time in graduate school. You can consider this an IOU for many turns at washing the dishes.

Most of all, I would like to thank my parents. I quite literally could not have made it here without you. You made me who I am, with both the curiosity to pursue this path and the stubbornness to stick to it. Your love, support, and encouragement have been with me every step of the way, and I love you both more than I can express.

PREFACE

Our own home galaxy, the Milky Way, is the galaxy astronomers are capable of studying in the most detail and the one galaxy we might expect to understand the best. However, there are crucial aspects of the histories of the Milky Way Galaxy and other similar galaxies that we still do not understand well. Galaxies that physically resemble the Milky Way appear to be common in the universe, but their very abundance presents a puzzle for galaxy evolution models in which Milky-Way-like galaxy disks are frequently destroyed by violent mergers between galaxies. One way out of this apparent paradox is that while galaxy disks may frequently be destroyed by mergers they may also *regrow* at later times in a potentially repeating cycle of disk growth and destruction. In this thesis, we search for observational evidence of the predicted disk regrowth process in a population of galaxies that are thought to result from disk-destroying mergers.

The first project that forms part of this thesis (Chapter 2) was previously published as an article in *The Astrophysical Journal* with the title "Extended UV Disks and UV-Bright Disks in Low-Mass E/S0 Galaxies." My coauthors on this work are Sheila J. Kannappan, Andrew J. Baker, and Seppo Laine. Earlier version of this work have also been published in conference proceedings of the Astronomical Society of the Pacific and European Astronomical Society. The second project that forms part of this thesis (Chapter 3) is not yet published but will soon be submitted for publication. My coauthors on this work are Sheila J. Kannappan, Andreas A. Berlind, Kathleen D. Eckert, David V. Stark, David Hendel, Mark A. Norris, and Norman A. Grogin. The final project that forms part of this thesis (Chapter 4) is at an advanced stage, with results available for about half the sample. My coauthors on this work are Sheila J. Kannappan, Mark A. Norris, Erik A. Hoversten, Andreas A. Berlind, Kathleen D. Eckert, and David V. Stark.

TABLE OF CONTENTS

LIST OF FIGURES ..... **xii**

LIST OF TABLES ..... **xiii**

LIST OF ABBREVIATIONS AND SYMBOLS ..... **xiv**

CHAPTER 1: INTRODUCTION **1**

1.1 Background 1

1.2 Galaxy Samples 3

1.3 Research Approaches 5

1.4 Results Summary 6

CHAPTER 2: EXTENDED UV DISKS AND UV-BRIGHT DISKS IN LOW-MASS E/S0 GALAXIES **7**

2.1 Introduction 7

2.2 Sample and Data Reduction 9

2.3 Identifying Extended Star Formation 12

2.3.1 Prior Definitions 13

2.3.2 A New Purely Quantitative XUV Disk Definition 14

2.3.3 UV-Bright (UV-B) Disk Definition 16

2.4 XUV Disk Properties and Demographics 19

2.4.1 Extents and Ages 19

2.4.2 Demographics 20

2.4.3 Star Formation 23

2.5 UV-B Disk Properties and Demographics 23

2.5.1 Extents and Ages 23

2.5.2 Demographics 24

2.5.3 Star Formation 24

2.6 Discussion 24

2.6.1 High Frequencies of XUV and UV-B Disks 26
2.6.2 Ubiquity of XUVs Compared to UV-Bs 28
2.6.3 Relationship to Star Formation and HI Content 29
2.7 Conclusions 29
CHAPTER 3: ECO AND RESOLVE: GALAXY DISK GROWTH IN ENVIRONMENTAL CONTEXT **34**
3.1 Introduction 34
3.2 Samples 38
3.2.1 ECO catalog 38
3.2.2 RESOLVE-B 42
3.3 Methods 42
3.3.1 Imaging/Photometry 44
3.3.2 Color and Stellar Mass Estimation 45
3.3.3 The Red and Blue Sequences 45
3.3.4 Morphology Classification 46
3.3.5 Identification of UV Disks 48
3.3.6 Environment Metrics 49
3.3.7 Atomic Gas Mass Estimates 52
3.3.8 Completeness Corrections 56
3.4 Results 58
3.4.1 Traditional Morphology-Environment Relation - P(M|E) 59
3.4.2 Alternative Morphology-Environment Relation - P(E|M) 61
3.4.3 Extreme Gas Richness and Environment 66
3.4.4 UV Disk Growth and Environment 73
3.5 Discussion 73
3.5.1 Morphology-Environment Relations 73
3.5.2 The Regime of Extreme Gas Richness and Recent Disk Growth 76
3.6 Conclusions 77
CHAPTER 4: SECONDARY DISKS AND DISK REGROWTH IN RESOLVE S0S **81**

4.1 Introduction 81
4.2 Data and Methods 82
4.2.1 Sample 82
4.2.2 Observations and Data Reduction 84
4.2.3 Identification of Stellar-Stellar Counterrotation 87
4.3 Results and Discussion 88
4.4 Conclusions 106
CHAPTER 5: CONCLUSIONS AND FUTURE WORK **109**
APPENDIX A: RESOLVE MORPHOLOGY CLASSIFICATION **112**
BIBLIOGRAPHY **116**

LIST OF FIGURES

2.1 *GALEX* GI and archival E/S0 sample in color-stellar mass space. 10

2.2 Images and surface brightness profiles of NGC 4117, one of several XUV-disk galaxies identified on the red sequence. 11

2.3 FUV$-r$ color for selected composite stellar population models, illustrating issues with using this color as a clean young/old population divider. 17

2.4 NUV$-K$ color for selected composite stellar population models, illustrating NUV$-K$ cuts chosen for our analysis. 18

2.5 *GALEX* GI and archival E/S0 sample in color-stellar mass space showing UV disks identified according to three different classifications. 19

2.6 Optical outer-disk colors for sample E/S0s. 21

2.7 HI content versus NUV$-K$ color measured within the detected galaxy extent in the NUV. 22

2.8 Smoothed NUV contours overlaid on DSS-II red images of XUV-disk E/S0s. 25

2.9 Smoothed NUV contours overlaid on DSS-II red images of UV-B disk E/S0s that are not also XUV-disk E/S0s. 26

2.10 Smoothed NUV contours overlaid on DSS-II red images of E/S0s in our sample without XUV or UV-B disks. 27

3.1 The ECO catalog region in sky coordinates, with color coding according to group halo masses. 38

3.2 The ECO catalog region in RA vs. line-of-sight distance coordinates. 39

3.3 Illustration of the completeness and selection of the ECO catalog. 40

3.4 The distribution of galaxies by halo mass in the ECO, ECO+G, and RESOLVE-B samples. 43

3.5 Color vs. stellar mass for the ECO catalog sample. 46

3.6 Quantitative morphology metrics applied to by-eye classified galaxies in the RESOLVE and ECO samples. 47

3.7 Illustration of the recovery of real-space mock galaxy catalog group velocity dispersions after finger-of-God collapse. 53

3.8 Illustration of the finger-of-God collapse procedure applied to the ECO catalog. 54

3.9 Multiplicative completeness correction factors for each ECO galaxy. 56

3.10 Illustration of ECO catalog galaxy distributions in the group halo mass and galaxy baryonic mass space. 58

3.11 Illustration of the traditional morphology-environment relation in the ECO and RESOLVE-B samples. 59

3.12 Illustration of morphology-environment relations in the ECO sample for separate high- and low-mass samples. 60

3.13 Halo mass distribution for early and late type galaxies in the ECO sample..... 61

3.14 Variation in blue early type galaxy frequency as a function of stellar mass in the ECO sample. 62

3.15 Characteristic distribution of halo mass as a function of stellar mass for different galaxy types..... 64

3.16 Characteristic distribution of halo mass as a function of baryonic mass for different galaxy types..... 65

3.17 Characteristic distribution of environmental density (∼1.43 Mpc smoothing kernel) as a function of baryonic mass for different galaxy types..... 67

3.18 The environment-dependent frequency of HI gas-to-stellar mass ratios greater and less than one for ECO+A galaxies. 68

3.19 The frequency of HI gas-to-stellar mass ratios greater and less than one as a function of group halo mass for central and satellite galaxies..... 69

3.20 Characteristic distribution of HI gas-to-stellar mass ratio as a function of group halo mass for different galaxy types. 70

3.21 Halo mass distribution for blue early type galaxies in the ECO sample with different levels of HI gas. 71

3.22 Frequency and gas content of early-type UV-B disk hosts in the ECO+G sample. 72

4.1 RESOLVE deep S0 spectroscopy sample in the parameter spaces of model color vs. stellar mass and group halo mass vs. stellar mass. 83

4.2 Stellar cross-correlation profiles plus rotation and velocity dispersion measurements for observed targets in the RESOLVE deep S0 spectroscopy sample..... 89

4.3 Cross-correlation profiles plus rotation/velocity dispersion measurements (cont.)..... 90

4.4 Cross-correlation profiles plus rotation/velocity dispersion measurements (cont.)..... 91

4.5 Cross-correlation profiles plus rotation/velocity dispersion measurements (cont.)..... 92

4.6 Cross-correlation profiles plus rotation/velocity dispersion measurements (cont.)..... 93

4.7 Cross-correlation profiles plus rotation/velocity dispersion measurements (cont.)..... 94

4.8 Cross-correlation profiles plus rotation/velocity dispersion measurements (cont.)..... 95

4.9 Cross-correlation profiles plus rotation/velocity dispersion measurements (cont.)..... 96

4.10 Cross-correlation profiles plus rotation/velocity dispersion measurements (cont.)..... 97

4.11 Cross-correlation profiles plus rotation/velocity dispersion measurements (cont.)..... 98

4.12 Cross-correlation profiles plus rotation/velocity dispersion measurements (cont.)..... 99

4.13 Cross-correlation profiles plus rotation/velocity dispersion measurements (cont.). 100

4.14 Cross-correlation profiles plus rotation/velocity dispersion measurements (cont.). 101

4.15 Cross-correlation profiles plus rotation/velocity dispersion measurements (cont.). 102

4.16 Cross-correlation profiles plus rotation/velocity dispersion measurements (cont.). 103

4.17 Cross-correlation profiles plus rotation/velocity dispersion measurements (cont.). 104

4.18 Stellar and group halo mass distribution of counterrotating and non-counterrotating RESOLVE S0s. 104

4.19 Color distribution of counterrotating and non-counterrotating RESOLVE S0s. 105

A.1 Morphology training set classification comparison. 114

A.2 Evaluation of classification drift. 115

LIST OF TABLES

2.1 Summary of Relevant UV-disk Definitions 12

2.2 Summary of *GALEX* GI and Archival E/S0 Sample Properties 32

2.2 Summary of *GALEX* GI and Archival E/S0 Sample Properties 33

3.1 ECO Sample Properties 80

4.1 RESOLVE Deep S0 Spectroscopy Sample 108

LIST OF ABBREVIATIONS AND SYMBOLS

C_r	concentration index morphology metric
E	Elliptical galaxy
ECO	Environmental COntext catalog
FWHM	full width at half maximum
H_0	Hubble constant
KDC	kinematically decoupled core
KGB	Kannappan et al. 2009
K-S	Kolmogorov-Smirnov
M_b	galaxy bimodality mass
M_{bary}	galaxy stellar plus atomic gas mass
M_{halo}	group halo mass
M_{HI}	galaxy atomic gas mass
M_*	galaxy stellar mass
$M_\odot$	solar mass
M_r	absolute magnitude in r band
M_t	gas-richness threshold mass
μ_Δ	surface mass density contrast morphology metric
NFGS	Nearby Field Galaxy Survey
RESOLVE	REsolved Spectroscopy Of a Local VolumE survey
R_{vir}	group virial radius
$R_{x\%}$	galaxy radius at x% total light isophote (r band)
SDSS	Sloan Digital Sky Survey
SSP	simple stellar population
T07	Thilker et al. 2007
UV-B	UV-Bright disk
XUV	extended ultraviolet disk
z	redshift

CHAPTER 1: INTRODUCTION

The field of galaxy evolution is relatively young, dating only as far back as the mid-twentieth century when a variety of galaxy formation/evolution models were first proposed (e.g., Eggen et al. 1962; Larson 1969; Toomre 1977). A great deal of progress has been made in the intervening years, but some fundamental aspects of galaxy evolution remain uncertain. We still lack a complete understanding of the physical processes that shape the evolution of galaxies in the real universe, since many processes that are predicted in galaxy formation/evolution models are difficult (or impossible) to observe in action. In this work, our goal is examine observational signatures of the existence of one such predicted process, known as galaxy disk regrowth. Building on the prior observational evidence of Kannappan et al. (2009, hereafter KGB) for disk regrowth, we seek new constraints on the observed frequency, significance, and conditions of this process.

In the next section, we provide further background on aspects of galaxy evolution that are relevant to our consideration of disk regrowth. In §1.2 and 1.3, we provide an overview of the galaxy samples and approaches used in this research. In §1.4, we provide a brief summary of the major results of this thesis.

1.1 Background

In the prevailing hierarchical, cold dark matter model of galaxy formation (e.g., Lacey & Cole 1993), galaxies are thought to build up over time in a successive series of mergers and acquisitions. Each merger or significant acquisition of material has the potential to alter a galaxy's morphology. In general, spheroidal galaxy components result from mergers dominated by stellar dynamics in which pre-existing disk components are typically destroyed (e.g., Toomre & Toomre 1972; Steinmetz & Navarro 2002). In the case of mergers that involve either galaxies with significant gas or later external gas accretion onto the merger remnant, stellar disks may potentially be retained or regenerated at later times (e.g., Steinmetz & Navarro 2002; Barnes 2002; Governato et al. 2007; Hopkins et al. 2009).

Spiral galaxy morphology is characterized by both a central spheroidal bulge and an extended, structured disk. Elliptical (E) and S0 galaxy morphologies, characterized by purely spheroidal

or spheroid plus smooth outer disk configurations, are often thought to result from galaxy-galaxy mergers, although the E/S0 galaxy population is potentially a heterogeneous one with a variety of proposed formation channels that also include gas stripping and/or disturbance of spirals in a larger-scale potential (e.g., Gunn & Gott 1972; Moore et al. 1998). Through hierarchical merging processes, spiral galaxies are predicted to transform into spheroid-dominated E/S0s but also subsequently *regrow* new disks if sufficient gas to fuel this process is available (e.g., Baugh et al. 1996; Steinmetz & Navarro 2002; Governato et al. 2007).

A number of observational clues pointing to the occurrence of this process have recently emerged, primarily centered on the population of "blue-sequence" E/S0 galaxies, which inhabit the star-forming sequence in color vs. stellar mass space alongside spirals (KGB). The existence of such E/S0s contradicts the traditional idea that E/S0s are "red and dead" systems, devoid of recent star formation activity. KGB find that the blue-sequence E/S0 population becomes most common at low stellar masses, below the so-called "gas-richness threshold" mass $M_t \sim 5 \times 10^9\, M_\odot$. Further work has corroborated that such galaxies are associated with large gas reservoirs, which are typically sufficient to fuel significant stellar mass growth on several Gyr timescales (Wei et al. 2010). Stark et al. (2013) also find evidence for the growth of both gas and stellar disks in blue-sequence E/S0s.

The link between this blue-sequence E/S0 population and a particular mass scale associated with gas richness raises the intriguing possibility that the existence of blue-sequence E/S0s is tied to a gas acquisition channel that depends on mass, such as the theorized "cold mode" gas accretion process (e.g., Birnboim & Dekel 2003; Kereš et al. 2005). Recent simulation results have challenged the theory of cold mode gas accretion, inferring that most gas accreted onto galaxies actually arrives in a heated form (e.g., Nelson et al. 2013). However, such results have retained an important aspect of the cold-mode accretion theory: that gas accretion is most effective in group halos with low masses (e.g., Nelson et al. 2013; Birnboim & Dekel 2003; Kereš et al. 2005). Such halos also tend to host central galaxies with low stellar masses, similar to those typical of blue-sequence E/S0s.

In this thesis, we consider the blue-sequence E/S0 population to be a significant population of interest as we work towards observational determinations of the frequency, significance, and conditions of E/S0 disk regrowth. This work provides new constraints on the processes related to the morphological transformation of galaxies and, more generally, on the prevalence of galaxy growth by stellar disk (as opposed to spheroid) formation.

1.2 Galaxy Samples

We analyze three primary galaxy samples in this work, which are largely subsets of the Nearby Field Galaxy Survey (NFGS; Jansen et al. 2000a,b), the Environmental COntext (ECO; Moffett et al., in prep., Chapter 3) catalog, and the REsolved Spectroscopy Of a Local VolumE (RESOLVE; Kannappan et al., in prep.) survey.

In Chapter 2, we consider a broad E/S0 sample drawn largely from the NFGS. The NFGS is a sample of 196 galaxies subselected from the first CfA Redshift Survey sample (Huchra et al. 1983), which carries a B-band apparent magnitude selection. The NFGS sample was chosen to reflect both the morphology and luminosity distributions of its parent sample but was also selected with an effective apparent size limit to allow spectroscopic observations on an instrument with fixed slit length by including the brightest, physically largest objects only at the greatest distances sampled (Jansen et al. 2000b). The NFGS includes a variety of low and high density environments, although explicit environment selections were not made other than the omission of Virgo Cluster galaxies to guard against cluster dominance of the sample.

The analysis of Chapter 2 primarily employs ultraviolet and near-infrared imaging obtained for *GALEX* observing program GI3-0046 and *Spitzer* observing program GO-30406 (both PI S. Kannappan). NFGS E/S0 galaxies with stellar masses below $\sim 4 \times 10^{10}\, M_{\odot}$, where blue-sequence E/S0s are observed in the largest numbers (KGB), were targeted for these observing programs. In addition to the NFGS galaxies, we incorporate E/S0s from the "HyperLeda+" sample of KGB, a cross matched catalog data compilation that includes HyperLEDA, Sloan Digital Sky Survey (SDSS) data release 4, and Two Micron All Sky Survey sources (Paturel et al. 2003; Adelman-McCarthy et al. 2006; Jarrett et al. 2000). We use only E/S0s that are consistent with the NFGS selection criteria and have available archival *GALEX* and *Spitzer* images of similarly high quality to those from our program observations. Our combined sample then consists of 38 E/S0 galaxies, with 25 drawn from the NFGS and 13 drawn from the "HyperLeda+" compilation.

For the analysis of Chapter 3, we expand to much larger statistical samples, with a primary focus on the newly created ECO catalog (Moffett et al., in prep.). While large galaxy samples like those now available from the SDSS database represent a powerful tool for studying galaxy properties statistically, such samples can also mask important details through failures of automated data reduction methods and/or systematic incompleteness effects. The key advantages of ECO over other

large catalog samples are its high, well-calibrated level of completeness and its high-quality photometric measurements, which have incorporated human inspection/interaction to improve estimates of photometric properties when fully automated methods fail.

The ECO catalog incorporates galaxy identifications and redshifts from multiple existing galaxy catalogs, including the RESOLVE (Kannappan et al., in prep.), Updated Zwicky Catalog (Falco et al. 1999), SDSS data release 6, 7, and 8 (Adelman-McCarthy et al. 2008; Abazajian et al. 2009; Aihara et al. 2011), HyperLEDA (Paturel et al. 2003), GAMA (Driver et al. 2011), 2dF (Colless et al. 2001), and 6dF (Jones et al. 2009) databases. ECO encompasses a volume of over 500,000 Mpc^3, including the "A-semester" region of RESOLVE. Over 15,000 galaxies are considered for membership in the final ECO sample, which is defined based on membership in groups whose centers lie within the ECO volume and on estimates of galaxy baryonic mass (stars plus gas) that can be made only after our custom photometric measurements have been carried out. The final ECO catalog sample with an approximate baryonic mass limit of $10^{9.3} M_{\odot}$ consists of just under 7,000 galaxies and traces the wide natural variety of galaxy environments contained within the large contiguous volume selection.

Subsets of the RESOLVE survey catalog are also used in both Chapter 3 and 4. In Chapter 3, we primarily use the RESOLVE "B-semester" volume as a comparison sample that is even more complete than ECO, forming the basis of completeness correction factors applied to the ECO membership. RESOLVE was designed to be a baryonic-mass-limited sample with extraordinarily high completeness, enabled in large part by our ongoing redshift completion efforts (Kannappan et al., in prep.). RESOLVE sample galaxies have been morphologically classified by RESOLVE team members, an effort that I have led (see Appendix A). RESOLVE encompasses both "A-semester" and "B-semester" volumes, which add to a total volume of approximately 50,000 Mpc^3 and include diverse galaxy environments. A major goal of RESOLVE is to obtain galaxy kinematic measurements for all survey galaxies inside these regions.

For the analysis of Chapter 4, we target a subsample of RESOLVE S0 galaxies for special extra-deep spectroscopic observations, which were carried out with UNC SOAR guaranteed time and NOAO programs 2010A-0110 (PI M. Norris), 2010B-0594, and 2011A-0164 (both PI A. Moffett). Within the pool of RESOLVE S0s for which we can expect to reliably measure kinematics and resolve potential velocity substructure, we have targeted 59 galaxies that sample the RESOLVE ranges of environments, stellar masses, and colors. As a sample intended for the identification of secondary stellar disks in S0s, this sample is unique in its selection from a single diverse, volume-limited sample where galaxy environments are well quantified. Our sample selection enables a

less biased estimation of secondary disk frequencies in various parameter-space regimes than has been possible with previous studies using samples focused only on bright galaxies, with inconsistent literature selections, and/or with poorly quantified environment distributions (e.g., Kuijken et al. 1996; Bettoni et al. 2001; KGB). As this project is a work in progress, we analyze only those targets for which final data reduction has been completed in Chapter 4.

1.3 Research Approaches

In this thesis, we take multiple approaches to the problem of determining the frequency, significance, and conditions of E/S0 disk regrowth. In Chapter 2, we explore this problem by examining the frequency and characteristics of UV-detected disks representing recent star formation in E/S0 galaxies. Following the original work on by-eye identifications of extended UV (XUV) disks (Thilker et al. 2005; Gil de Paz et al. 2005; Thilker et al. 2007), we define purely quantitative classifications for XUV disks and a new class of UV-Bright (UV-B) disks, which are specifically defined to require a $\gtrsim$10% disk mass contribution by a young stellar population.

Building on this initial small sample study, we further constrain the conditions of disk regrowth through consideration of the much larger, newly created ECO catalog in Chapter 3. As tracers of disk regrowth, we focus on the populations of blue-sequence E/S0s, gas-dominated galaxies, and E/S0 UV-B disk hosts. To identify E/S0s in ECO we use a semi-quantitative morphology classification method that combines by-eye classifications (where available) with a quantitative morphology discriminant calibrated on available ECO and RESOLVE by-eye morphology classifications. Gas-dominated galaxies are identified primarily through the overlap of ECO with the public Arecibo Legacy Fast ALFA (ALFALFA) α.40 catalog of HI mass estimates (Haynes et al. 2011) but also using the "photometric gas fraction" technique (Kannappan 2004) to assign HI mass estimates based on the tight correlation between $u - J$ color and gas to stellar mass ratio found by Kannappan et al. (2013).

Finally in Chapter 4, we take an even more direct approach to identifying disk regrowth through examination of kinematic signatures of secondary stellar disks in S0 galaxies. Using deep SOAR telescope and Goodman Spectrograph longslit observations focused on stellar absorption line features, we extract the detailed stellar velocity profile structure of our targets using cross-correlation with stellar population templates. We also estimate stellar rotation velocities and velocity dispersions using a template fitting procedure. We then use the spatial variations of the velocity structure and measured dispersions to identify targets with strong stellar-stellar counterrotation, indicating the

presence of two cospatial stellar disks.

1.4 Results Summary

In Chapter 2, we find high, approximately 40% frequencies of both XUV and UV-B disks in a low-mass E/S0 galaxy sample, with an even higher combined UV disk frequency of approximately 60% since the populations do not always overlap. UV-B disk hosts are found to be a population of particular interest in connection with the disk regrowth phenomenon, as these galaxies display relatively significant ($\gtrsim$10% by mass) recent disk growth, preferentially blue optical outer-disk colors, and high atomic gas content compared to E/S0s not hosting UV-B disks. Nearly all of the blue-sequence E/S0s in the sample below the gas-richness threshold stellar mass host UV-B disks, which supports the association of low-mass, blue-sequence E/S0s with significant disk growth and reinforces the idea that mass-scale dependent processes may be important in enabling such growth.

In Chapter 3, we find further evidence that mass scales play an important role in disk growth, with the focus now on the masses of the group halos that galaxies inhabit. Below group halo mass $\sim 10^{11.5} M_{\odot}$, we find that blue E/S0s, gas-dominated galaxies, and UV-B disk host galaxies become significantly more common, supporting a link between disk regrowth and this low group halo mass regime. We likewise find that the increase in spiral galaxy frequency at low group halo mass and the typically similar environments of low baryonic mass ($\lesssim 10^{10} M_{\odot}$) E/S0 and spiral galaxies are both consistent with a model in which E/S0 galaxies can regrow spiral disks in low group halo mass environments.

In Chapter 4, we find direct, kinematic evidence for secondary stellar disks in 6 S0 galaxies, which corresponds to a frequency of approximately 25% in our current sample. Given the small number statistics, we find no statistically significant differences in the stellar masses, environments, or colors of the S0s that host secondary stellar disks compared to those that do not. However, we find that the majority of our targets with secondary stellar disks inhabit low group halo mass environments, suggesting that our full sample could yield more definitive results on the environment distribution of S0s with secondary stellar disks.

CHAPTER 2: EXTENDED UV DISKS AND UV-BRIGHT DISKS IN LOW-MASS E/S0 GALAXIES

We have identified 15 XUV (extended ultraviolet) disks in a largely field sample of 38 E/S0 galaxies that have stellar masses primarily below $\sim 4 \times 10^{10}\, M_\odot$ and comparable numbers on the red and blue sequences. We use a new purely quantitative XUV disk definition designed with reference to the "Type 1" XUV disk definition found in the literature, requiring UV extension relative to a UV-defined star formation threshold radius. The 39±9% XUV-disk frequency for these E/S0s is roughly twice the ∼20% reported for late-type galaxies (although differences in XUV-disk criteria complicate the comparison), possibly indicating that XUV disks are preferentially associated with galaxies experiencing weak or inefficient star formation. Consistent with this interpretation, we find that the XUV disks in our sample do not correlate with enhanced outer-disk star formation as traced by blue *optical* outer-disk colors. However, UV-Bright (UV-B) disk galaxies with blue UV colors outside their optical 50% light radii *do* display enhanced optical outer-disk star formation as well as enhanced atomic gas content. UV-B disks occur in our E/S0s with a 42^{+9}_{-8}% frequency and need not coincide with XUV disks, thus their combined frequency is 61±9%. For both XUV and UV-B disks, UV colors typically imply <1 Gyr ages, and most such disks extend beyond the optical R_{25} radius. XUV disks occur over the full sample mass range and on both the red and blue sequences, suggesting an association with galaxy interactions or another similarly general evolutionary process. In contrast, UV-B disks favor the blue sequence and may also prefer low masses, perhaps reflecting the onset of cold-mode gas accretion or another mass-dependent evolutionary process. Virtually all blue E/S0s in the gas-rich regime below stellar mass $M_t \sim 5 \times 10^9\, M_\odot$ (the "gas-richness threshold mass") display UV-B disks, supporting the previously suggested association of this population with active disk growth.

2.1 Introduction

In hierarchical models of galaxy formation, galaxies often experience mergers that result in early-type remnants. Disk structures are also predicted to regrow around some of these remnants (e.g., Steinmetz & Navarro 2002; Governato et al. 2007), allowing for transitions back from early- to

late-type morphologies. Observationally, a transition stage from late to early types, brought about by interactions, may be glimpsed in the population of E+A (post-starburst) galaxies (e.g., Yang et al. 2008). However, observational evidence for the opposite predicted transition, that from early- to late-type morphology, has remained more elusive.

The ultraviolet regime offers a natural choice for studying possible disk growth. Recently, *GALEX* has enabled the discovery of extended ultraviolet (XUV) disks (e.g., Thilker et al. 2005; Gil de Paz et al. 2005). These XUV disks show ongoing star formation beyond the optical radii and traditional star formation thresholds of late-type galaxies, providing an intriguing new look at galaxy disk growth in progress at $z\sim0$. In a nearby galaxy sample emphasizing late types, Thilker et al. (2007, hereafter T07) find a 20% incidence of "Type 1" XUV disks, characterized primarily by large radial extents and structured UV morphologies (versus "Type 2" XUV disks, which consist of less-extended UV-bright zones without morphological specifications).

GALEX has provided a useful platform for detection of star formation in early-type galaxies as well. Kauffmann et al. (2007) find that extended UV emission is common in high-mass bulge-dominated galaxies, likely associated with modest reservoirs of cold gas in the disk that help fuel bulge and black hole growth. Focusing specifically on galaxies with E/S0 morphology, extended UV emission has also been seen in ring structures around several S0 galaxies (Donovan et al. 2009; Cortese & Hughes 2009), and Thilker et al. (2010) recently identified an XUV disk around the nearby S0 NGC 404. Salim & Rich (2010) have also identified several $z<0.12$ early-type galaxies with extended UV structures in far-ultraviolet *HST* imaging.

The presence of XUV disks, however, can have a variety of interpretations. T07, for example, suggest an association of XUV disks with interactions or minor perturbations. The raw material for XUV disk formation could be acquired externally from such interactions or from fresh cosmic gas accretion, either of which may be consistent with the extended disks and rings of HI commonly observed around E/S0s (e.g., Sage & Welch 2006; Morganti et al. 2006; Oosterloo et al. 2007; Oosterloo et al. 2010). Another possibility for creating extended disks in early types is the fallback of tidal tails in late stage mergers (e.g., Hibbard & Mihos 1995; Barnes 2002; Naab et al. 2006).

The evolutionary significance of disk growth may be greater in some of these scenarios than others. Of particular interest is the scenario of cold mode gas accretion (e.g., Birnboim & Dekel 2003; Kereš et al. 2005; Dekel & Birnboim 2006; Kereš et al. 2009), which may be linked to disk building in "blue-sequence E/S0s," a recently identified morphologically defined population of E/S0 galaxies on the blue sequence in color versus stellar mass (Kannappan et al. 2009). Blue-sequence

E/S0s are primarily found in non-cluster environments (KGB), and as shown in KGB and Wei et al. (2010), many display global gas reservoirs and specific star formation rates that could allow the growth of significant new disks on relatively short timescales.

Cold mode accretion occurs primarily below a critical shock heating stability mass (e.g., Birnboim & Dekel 2003; Kereš et al. 2005); this mass may coincide with an observed "gas-richness threshold" stellar mass at $M_t \sim 5 \times 10^9\, M_\odot$, below which blue-sequence E/S0s become suddenly common, along with gas-dominated galaxies (Kannappan 2004; Kannappan & Wei 2008; see KGB regarding corrected mass scale). This low-mass regime may be where the most active E/S0 disk growth occurs (KGB). Blue-sequence E/S0s also occur in modest numbers up to stellar masses of $\sim 3 \times 10^{10}\, M_\odot$, the bimodality mass of Kauffmann et al. (2003), above which classical spheroids with older stellar populations begin to dominate.

To better understand the significance of recent disk star formation in E/S0s, we concentrate on the mass regime up to the bimodality mass and seek to quantify the incidence of extended-disk star formation in a representative, largely field sample of E/S0s. In §2.2, we introduce our chosen sample and basic data. In §2.3, we discuss various methods for identifying extended star formation, adopting the T07 Type 1 XUV-disk designation as a reference. We then propose modifications to this definition to create a purely quantitative classification that reflects recent extended disk star formation in early types. Since we are interested in the presence of disk star formation in a general sense, we also introduce an alternative UV-Bright (UV-B) disk definition, which can be used to identify significant disk star formation not necessarily extended relative to traditional star formation thresholds. In §2.4-2.5, we present demographics and properties of our classified XUV and UV-B disks, and in §2.6 we compare our results to various formation scenarios and results from the literature. Finally, we provide a brief summary in §2.7.

2.2 Sample and Data Reduction

Our "*GALEX* GI" sample of 30 E/S0s was defined for *GALEX* program GI3-0046 and primarily draws on the Nearby Field Galaxy Survey (NFGS, Jansen et al. 2000a,b). The sample was selected to encompass all of the NFGS blue-sequence E/S0s and the majority of NFGS red-sequence E/S0s in the stellar mass range below $\sim 4 \times 10^{10}\, M_\odot$ (Fig. 2.1), where many E/S0s have substantial gas and settled blue-sequence E/S0s with the potential for disk regrowth are observed (KGB). The NFGS provides a representative sample of galaxies in the $z \sim 0$ universe with a wide range of luminosities, morphologies, and environments, allowing us to explore the natural variety of stages in galaxy

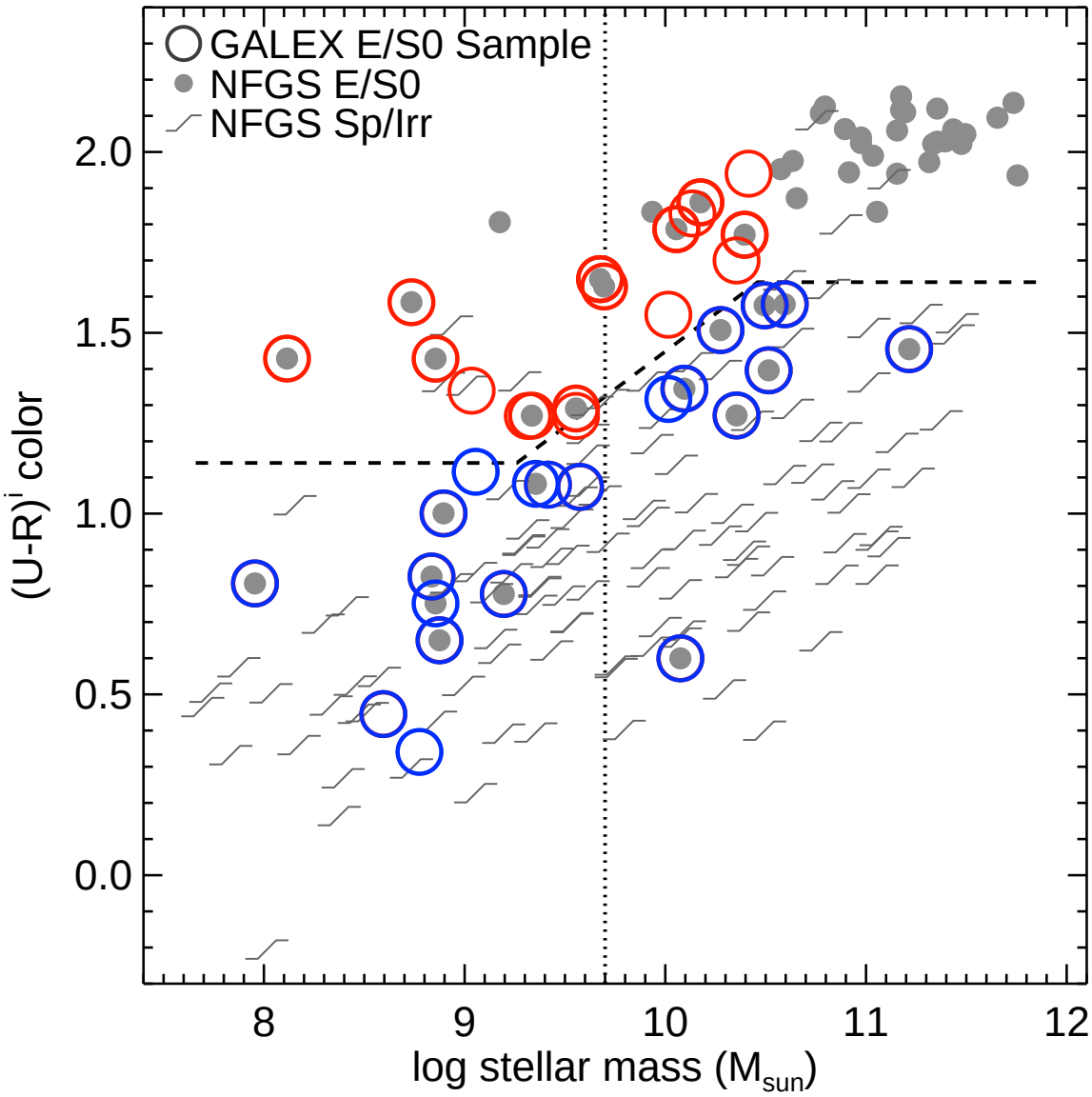

Figure 2.1 *GALEX* GI and archival E/S0 sample in color-stellar mass space. The small grey symbols indicate galaxies in the Nearby Field Galaxy Survey, the parent sample for the majority of our E/S0s (§2.2). The dashed line divides the red and blue sequences, and the vertical line marks the gas-richness threshold mass (KGB). The 38 E/S0s with *GALEX* data are denoted by open circles.

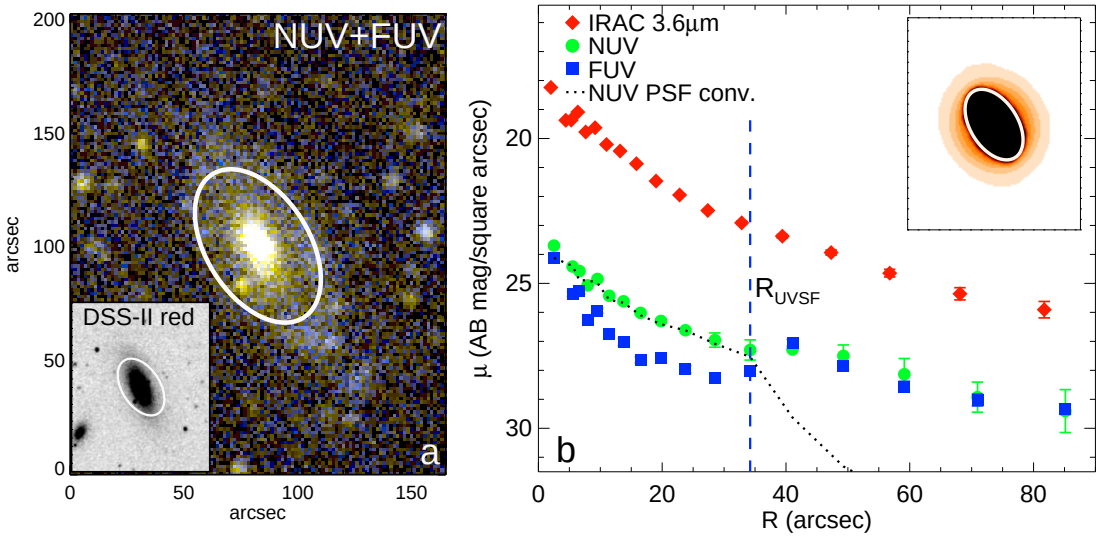

Figure 2.2 Images and surface brightness profiles of NGC 4117, one of several XUV-disk galaxies identified on the red sequence. (a) *GALEX* NUV+FUV color composite with overlay of the NUV-derived star formation threshold, $R_{\rm UVSF}$ (see §2.3). The inset shows the DSS-II red image with the same overlay for scale. (b) *GALEX* and *Spitzer* surface brightness profiles. A vertical line marks $R_{\rm UVSF}$. The black dotted line represents a profile extracted from the 2D (re)convolution of the NUV PSF with the NUV galaxy light within $R_{\rm UVSF}$ (see §2.3). The inset shows the (re)convolved image.

evolution. In addition to 25 NFGS E/S0s, the sample includes 5 blue-sequence E/S0s from the "HyperLeda+" sample of KGB with comparable archival data.

To augment this sample, we have cross-matched all $M_* \lesssim 4 \times 10^{10}\,M_\odot$ E/S0s in the "HyperLeda+" sample of KGB with the *GALEX* and *Spitzer* archives to find sources imaged with exposure times similar to those for our prior programs. Excluding Virgo Cluster members from this cross-matched sample (consistent with the NFGS selection criteria), we find eight additional E/S0s for our "archival" sample.

Our primary data are *GALEX* NUV and FUV images at least as deep as those of the Medium Imaging Survey (MIS). For comparison of UV and optical morphologies, we employ DSS-II red images (http://archive.stsci.edu/dss/). For profile analysis, we compare to *Spitzer* IRAC 3.6 μm imaging mostly obtained for program GO-30406 with typical exposure times of 480 s (although several archival sources have exposure times down to 120 s). The 3.6 μm imaging serves as a proxy for K-band data, assuming the Leroy et al. (2008) conversion $I_{3.6} = 0.55 I_K$ (MJy ster^{-1}). We use the notation K_{80} to denote the 80% light radius calculated using the 3.6 μm data, to indicate the direct analogy with the K_{80} radius of T07.

We use *GALEX* imaging in a pipeline-processed form with the zero point calibrations of Morrissey

Table 2.1. Summary of Relevant UV-disk Definitions

Definition	Extent Criterion	Recent Star Formation Criterion
T07 Type 1 XUV	UV visually identified beyond $R_{\rm UVSF}$	structured, bright UV with morphology different from optical
Purely Quantitative XUV	UV $>3\sigma$ above PSF shelf beyond $R_{\rm UVSF}$	NUV$-K$ consistent with young population
UV-B	blue UV color beyond optical R_{50}	NUV$-K$ consistent with $\gtrsim$10% young population

et al. (2007). We apply foreground extinction corrections based on Schlegel et al. (1998) and Cardelli et al. (1989), but correction factors for internal extinction are not applied (consistent with prior XUV-disk studies). *Spitzer* IRAC 3.6 μm imaging is also pipeline processed and calibrated according to procedures outlined in the IRAC Instrument Handbook[1]. In addition to the pipeline processing, we apply a median background subtraction procedure.

From these data, we extract radial surface brightness profiles and magnitudes by totaling fluxes in elliptical apertures. The parameters of these ellipses were determined from isophotal fits to optical images (as reported in Jansen et al. 2000a for NFGS galaxies) and newly derived using the IRAF ELLIPSE task and SDSS g-band imaging (Abazajian et al. 2009) for non-NFGS sample galaxies (parameters for non-NFGS galaxies in the *GALEX* GI sample from Stark et al., in prep). Detection and masking of non-galaxy sources in these images was accomplished using SExtractor (Bertin & Arnouts 1996). For calculation of comparative *GALEX* and *Spitzer* photometry, our UV and IR images were convolved with an appropriately sized Gaussian kernel to yield degraded images with the same PSF FWHM as the lowest-resolution NUV images (FWHM $\sim$4.9$''$).

2.3 Identifying Extended Star Formation

Here we discuss UV-based methods for identifying galaxies with recent star formation in disks and extended disks. Ideally, we seek to employ a purely quantitative method of classification. We also seek to answer two distinct questions about extended star formation in our sample, for which different specific identification methods are relevant. First, does it occur beyond traditional star formation thresholds? This question motivated the original "Type 1" XUV-disk definition of T07, which we take as a reference in designing a purely quantitative XUV disk definition (§2.3.2). Second, is it *significant* (in a mass-contribution sense) in the optical outer disks of galaxies? This question motivates our introduction of a new "Ultraviolet-Bright" (UV-B) disk definition (§2.3.3; see also Table 2.1 for a summary of definitions used in this paper).

We note that extension relative to UV-defined star formation thresholds does not necessarily

[1]see http://irsa.ipac.caltech.edu/data/SPITZER/docs/irac/iracinstrumenthandbook/

imply extension beyond the full optical extent of the galaxy. Thus, another natural question about extended star formation is: does it extend beyond the optical galaxy? We will treat the answer to this question as a matter of investigation rather than definition, given that the radial extent of star formation relative to the optical disk may behave fundamentally differently in E/S0s vs. late-type galaxies, for example, in the case of inside-out disk (re)growth.

2.3.1 Prior Definitions

A natural choice for answering our first guiding question, concerning star formation extended beyond traditional star formation thresholds, is the T07 "Type 1" XUV-disk definition. T07 define Type 1 XUV disks as displaying more than one structured UV-bright emission complex beyond a centralized surface-brightness contour corresponding to the expected star formation threshold (equated to an NUV surface brightness of 27.35 AB mag arcsec^{-2} by T07, roughly matching typical Hα and HI thresholds; we label the corresponding radius $R_{\rm UVSF}$). In addition to extension relative to this UV contour, the definition requires that the XUV emission take on a different morphology from any underlying optical emission. T07 also define a Type 2 XUV-disk classification, but this is not geared towards tracing star formation beyond $R_{\rm UVSF}$, and an issue[2] with the definition implies that we cannot apply it uniformly to early types. Thus, we do not consider Type 2 XUVs further here and henceforth are referring to Type 1 XUVs when we reference T07 XUV designations.

The T07 XUV definition is the basis for our new XUV definition (described in §2.3.2), but for completeness, we note that several other measures of bright and/or extended UV disks exist, most requiring high spatial resolution. For example, visual classification of UV structures such as rings is common in the literature (e.g., Cortese & Hughes 2009; Salim & Rich 2010; Marino et al. 2011). A quantitative variant on extended UV disk identification involves measuring individual UV knots in the outer regions of galaxies (e.g., Zaritsky & Christlein 2007). Another quantitative approach lacking the high resolution requirement is the blue integrated UV-color cut of Kauffmann et al. (2007). However, with an integrated color cut alone the correspondence between blue color and extended star formation is not necessarily one-to-one. We modify this approach by adopting an *outer-disk* UV color cut in our UV-B disk definition (see §2.3.3), addressing our second guiding question regarding significant star formation in the optical outer disks of galaxies.

[2]The Type 2 XUV-disk classification requires FUV(AB) $-$ K(AB) $\leq$ 4 in a large, optically low surface brightness zone within $R_{\rm UVSF}$ but outside K_{80}. Here "large" means an area at least seven times that enclosed within K_{80}. The Type 2 definition was developed for a late-type sample and has proved problematic to apply to E/S0s, in that $R_{\rm UVSF}$ often lies inside the K_{80} radius, or lies outside but not as far as the definition requires (see also Moffett et al. 2010 for further details).

2.3.2 A New Purely Quantitative XUV Disk Definition

To answer whether or not star formation occurs beyond $R_{\rm UVSF}$, we adopt the T07 XUV-disk definition as a useful reference definition and construct a purely quantitative alternative. Table 2.2 indicates the distribution and properties of the 16 XUVs we identify by the original T07 definition; see Figure 2.2 for an example. The primary criteria of the T07 XUV-disk classification are UV extension relative to $R_{\rm UVSF}$ and association of this emission with recent star formation. In the following sections, we discuss issues with these criteria that motivate elements of our modified definition, including consideration of possible UV upturn contributions and of the extended PSF shelf in the *GALEX* NUV.

Ensuring Young Ages

A possible concern in identifying XUV disks in E/S0s is the prevalence of the UV upturn, i.e., UV emission associated with old stellar populations (O'Connell 1999). To mitigate this issue, we identify XUV disks in the NUV (in contrast to T07's use of a combination of FUV and NUV data) since the UV upturn becomes stronger at FUV wavelengths. Nonetheless, 5 of the 16 XUVs we find using the original T07 XUV-disk definition have XUV-disk region FUV$-K$ colors red enough to be consistent with a >1 Gyr SSP (simple stellar population, as in T07 Figure 1).

In general, the T07 requirement that UV emission take on a different morphology from any underlying optical emission should preclude classifying an underlying old population as a separate XUV disk. However, the subjective requirement of structured emission can be difficult to apply consistently to samples like our own: our galaxies tend to have smaller angular sizes than those of T07, implying greater blurring at the low angular resolution of *GALEX*, so UV structure may be lost or be difficult to assess. An XUV-disk definition relaxing this requirement of structured emission has recently been applied by Lemonias et al. (2011) to a sample containing both early and late types, and they experiment with using an FUV$-r$ cut to ensure young populations.

Taking a similar approach but focusing on the NUV, we consider color cuts based on a suite of composite Bruzual & Charlot (2003) stellar population models using a Salpeter (1955) initial mass function, as described in KGB (see their §2.3). These composite models are built from two (young and old) components, with set age options, combined in a variety of ratios to create a large model grid. Similar to the grid of KGB, the young SSP age options are 5, 25, 100, 290, 640, and 1000 Myr, while the old SSP age options are 1.4, 2.5, 3.5, ..., 13.5 Gyr. The young SSP contributions can be 0%, 1%, 2%, 4%, 8%, 16%, 32%, 64%, or 100% of the population mass. SSP metallicities allowed

in the grid are Z = 0.008, 0.02, and 0.05. The young SSP can have 11 different extinction values, but here we consider only zero-extinction models for comparison to observed outer-disk colors. We make no explicit restriction on the metallicity combinations of the composite population models we consider, although we find that consideration of metallicity restrictions that could be reasonable in specific circumstances, such as $Z_{young} \leq Z_{old}$ or $Z \leq Z_{solar}$, do not substantially change the model color distributions we report (see Figures 2.3 and 2.4).

In one version of their XUV-disk classifications, Lemonias et al. (2011) used a color cut at FUV-$r = 5$, designed to separate galaxies with recent XUV-disk star formation from those containing evolved populations (divider based on empirical red/blue sequence division from Wyder et al. 2007). However, based on consideration of our stellar population model grid (Fig. 2.3), this color selection can potentially exclude up to ∼30% of the composite populations with recently star-forming components.

Thus, we search for a different color selection that better encompasses composite stellar populations with young components. As a result of the aforementioned difficulties with using the FUV for this purpose and the practical usefulness of making such a selection in bands where data coverage is more complete, we prefer the NUV over the FUV. We find that NUV-based colors indeed display a more cleanly defined region where populations are predominantly old (compare Figures 2.3 and 2.4). From the model color distributions, it is apparent that the fraction of purely old models increases significantly beyond NUV$-K = 5$, which is where young model fractions start to decline as well. Thus, we choose to exclude XUV disks with NUV$-K > 5$.

Ensuring Extended Emission

When applying the original T07 XUV-disk definition, classifiers must subjectively identify the presence of extended emission beyond $R_{\rm UVSF}$. However, when classifying XUVs from *GALEX* NUV imaging, especially when considering galaxies with small angular sizes, the ∼45″ shelf in the NUV PSF (http://www.galex.caltech.edu/researcher/techdoc-ch5.html) may affect this judgment. Thus, to design a quantitative test for extension relative to $R_{\rm UVSF}$, we require that the NUV flux detected *outside* $R_{\rm UVSF}$ is significantly greater than ($>3\sigma$ above) the flux redistributed into this region by an artificial second convolution of the NUV PSF with the flux *inside* this radius. This (re)convolution is in addition to the natural convolution inherent in the images; see Figure 2.2 for an illustration. We note that for the XUV disks we have identified based on the original, subjective T07 definition, we have confirmed that this requirement is always satisfied.

Final Definition

In summary, for our "purely quantitative XUV-disk" designation, we ensure UV emission beyond $R_{\rm UVSF}$ by requiring $>3\sigma$ emission above the NUV PSF shelf, and we ensure recent star formation by requiring NUV$-K < 5$ in the XUV-disk region beyond $R_{\rm UVSF}$. Properties and demographics of these XUV disks are presented in §2.4 (see also Table 2.2) and largely imply that this population is associated with recent but not necessarily significant outer-disk star formation.

With our new definition, we identify a similar fraction of XUV disks as when applying the traditional T07 Type 1 XUV-disk definition (see Table 2.2, Figure 2.5), but the overlap between these classifications is not perfect. Approximately 70% of the traditionally identified XUVs are among XUVs identified with our purely quantitative method. In cases where the classifications do not overlap, the reason is either (1) insufficiently blue NUV$-K$ color to satisfy the new definition's color cut or (2) UV disk morphology not distinct enough from the optical to satisfy the T07 Type 1 definition. Our color cut is more conservative in rejecting XUV disks that may contain evolved populations than the T07 requirement of morphological differences compared to the optical. On the other hand, the T07 morphology requirement may recover XUVs with even weaker or more incipient star formation than our definition allows, where this star formation has not built up a detectable optical counterpart.

2.3.3 UV-Bright (UV-B) Disk Definition

To answer whether or not significant UV-detected star formation occurs in the optical outer-disk region, irrespective of extent beyond $R_{\rm UVSF}$, we construct a second quantitative classification.

We designate a population with a $\gtrsim$10% young component by mass as one containing "significant" star formation (in practice for our model set >8%, §2.3.2). Considering the aforementioned stellar population model grid, a more conservative color cut than was used in the purely quantitative XUV case appears necessary to select galaxies containing significant recent star formation (Fig. 2.4). Requiring NUV$-K < 4.5$ presents a natural choice for this definition, given the falloff in the fraction of models with a $\gtrsim$10% young population component beyond this value.

To quantify our region of interest for this definition, i.e., the optical outer disk, we select the region beyond the optical 50% light radius. Thus, our UV-B disk classification requires only NUV$-K$ < 4.5 beyond the optical 50% light radius. The properties and demographics of the UV-B disks are presented in §2.5 (see also Table 2.2) from which we conclude that these galaxies correlate well with enhanced optical disk star formation.

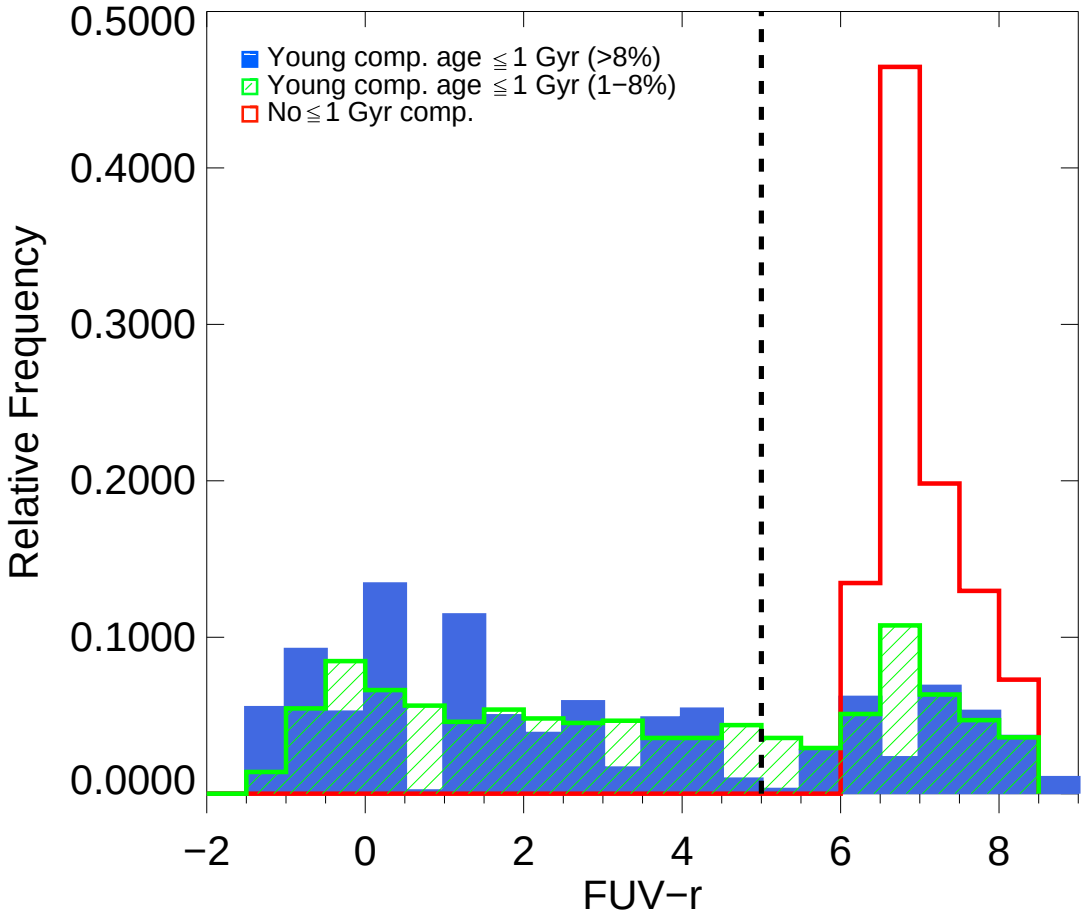

Figure 2.3 FUV$-r$ color for selected composite stellar population models (grid as described in §2.3.2), illustrating issues with using this color as a clean young/old population divider. Blue and green histograms represent numbers of models with >8% and 1-8% young population contributions by mass, normalized to the total numbers of such models. The red histogram represents numbers of models containing no young (age $\leq$ 1 Gyr) component, normalized to the total numbers of such models. The vertical dashed line indicates the color cut of Lemonias et al. (2011), which appears to miss a significant fraction ($\sim$30%) of the combined young model options that fall outside this cut with colors redder than FUV$-r = 5$.

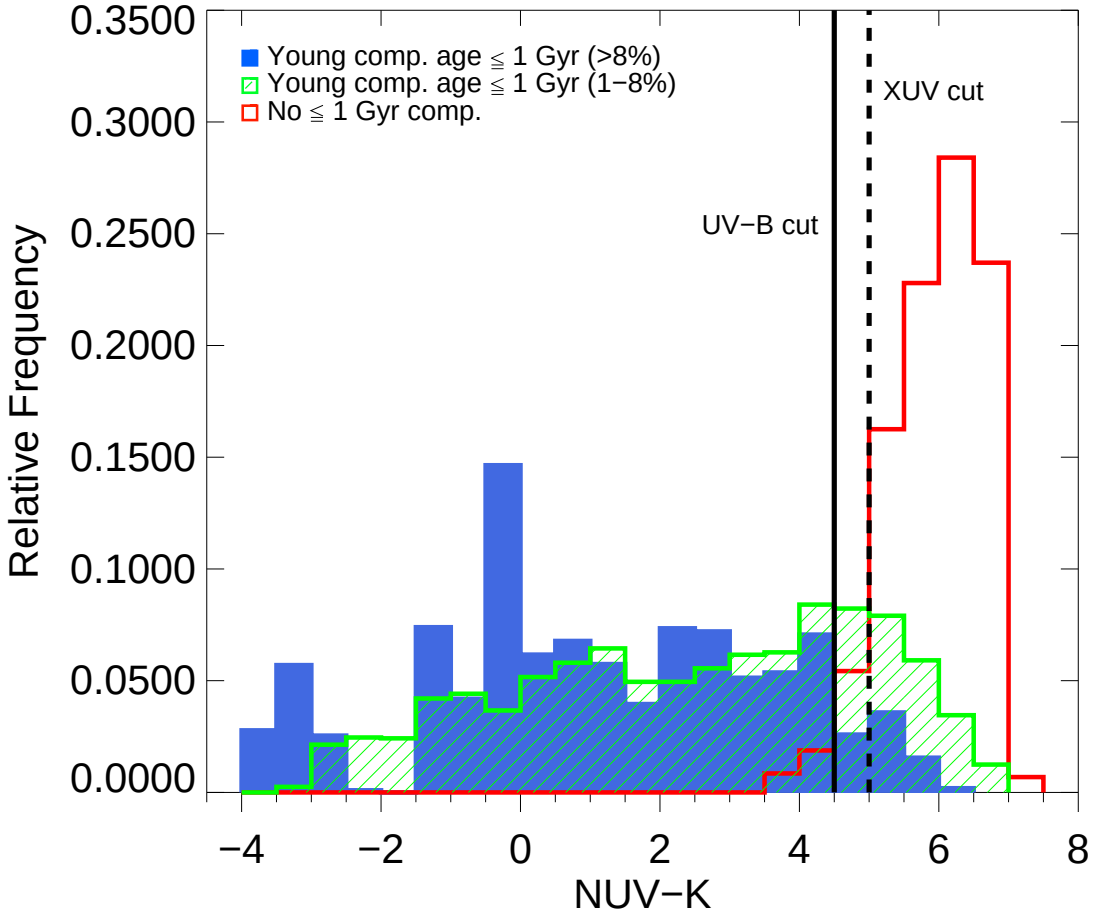

Figure 2.4 NUV$-K$ color for selected composite stellar population models (grid as described in §2.3.2), illustrating NUV$-K$ cuts chosen for our analysis. Blue and green histograms represent numbers of models with >8% and 1-8% young population contributions by mass, normalized to the total numbers of such models. The red histogram represents numbers of models containing no young (age $\leq$ 1 Gyr) component, normalized to the total numbers of such models. It is apparent that the fraction of purely old models increases significantly beyond NUV$-K = 5$, so we use this value to reject XUV disks likely to contain evolved populations as described in §2.3.2. A more conservative color cut at NUV$-K = 4.5$ appears necessary if we wish to select populations with a significant young population as in our UV-B disk classification (here >8%, corresponding to the $\gtrsim$10% requirement specified in §2.3.3).

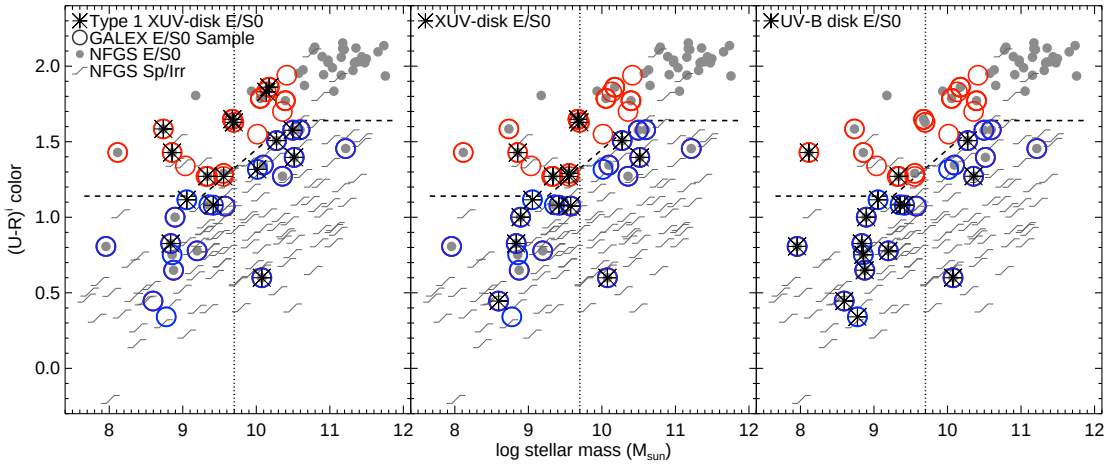

Figure 2.5 *GALEX* GI and archival E/S0 sample in color-stellar mass space (as in Figure 2.1), showing UV disks (asterisks) identified according to three different classifications: (left) the original T07 XUV-disk definition, (middle) our new, purely quantitative XUV definition, and (right) the UV-B disk definition.

2.4 XUV Disk Properties and Demographics

With our purely quantitative definition, we identify XUV disks in 15/38 or 39^{+9}_{-9}% of our E/S0 sample (see Table 2.2 for the identifications and Fig. 2.8 for images of classified XUVs). These XUV-disk classifications supersede the preliminary, purely visual classifications of Moffett et al. (2010), which were made without reference to $R_{\rm UVSF}$. In the following, we present the demographics and basic properties of the identified XUVs.

2.4.1 Extents and Ages

The XUV disks in our E/S0s can extend beyond R_{25}, as has been found in Type 1 XUV disks for late types (e.g., Thilker et al. 2005; Gil de Paz et al. 2005; T07; see also Zaritsky & Christlein 2007). We find radial extents (to the last measured NUV point) $\sim$0.7$-$2.3R_{25}, with mean $\sim$1.3R_{25} and $\sim$70% extending beyond R_{25}. Relative to the older populations traced by near-IR light, the average radial extent of the young XUV-disk component in our E/S0s is $\sim$2 times the K_{80} radius. Relative to the centralized younger populations traced by NUV light, the average radial extent of our XUV disks is $\sim$1.5 times $R_{\rm UVSF}$.

Compared to XUV disks in late-type galaxies, our E/S0 XUV disks tend to be redder. The reported outer-disk FUV$-$NUV colors of late-type XUV-disk galaxies in the literature range primarily between small negative values and $\sim$0.5 (Thilker et al. 2005; Gil de Paz et al. 2005, 2007). Our early-type XUV-disk galaxies have an average color of $\sim$1.4 in the XUV-disk regions (similar

to the early-type XUV-disk galaxy NGC 404, Thilker et al. 2010). However, the contour at $R_{\rm UVSF}$ for our early-type XUVs tends to occur closer to K_{80} than it does for late-type XUVs (enclosing on average ∼3 times the area of the K_{80} contour versus ∼15 for late types; see T07). Thus, redder XUV-disk colors in early types may simply indicate a greater contribution from the underlying old stellar population than is typical for late types.

The XUV-disk FUV−NUV colors we compute for our E/S0s are consistent with <1 Gyr ages from simple stellar population models. We choose to report SSP-equivalent ages for our XUVs in light of the inherent degeneracies involved in estimating separate old/young population ages from composite population models. We note that age estimates from stellar population models are affected by uncertainties in modeling the UV contribution from old stellar populations and will also vary depending on the assumed star formation history. Comparing with Bruzual & Charlot (2003) UV model colors for an instantaneous starburst with $Z = 0.02$ (as in T07 Figure 1), our average XUV-disk FUV−NUV color of ∼1.4 corresponds to an SSP with an approximate age of 500 Myr.

One of our XUV-disk galaxies does have XUV-disk region FUV$-K$ color red enough to be consistent with a >1 Gyr SSP (as in T07 Figure 1). However, all of our XUV-disk galaxies, including this red FUV$-K$ case, display independent indicators for recent or potential star formation, in the form of either Hα or HI detections in the NFGS or the literature.

2.4.2 Demographics

We find XUV disks in both red- and blue-sequence E/S0s and over a wide range in stellar mass (Fig. 2.5). On the red sequence, the XUV-disk frequencies are 0^{+23}% and 60^{+18}_{-20}% above and below the gas-richness threshold mass (at stellar mass $M_{\rm t} \sim 5 \times 10^9\, M_\odot$, KGB), respectively. On the blue sequence, the corresponding frequencies are 33^{+22}_{-18}% and 50±18%.

If we ignore mass dependence, we find no clear evidence for a preference in XUV-disk incidence between red- and blue-sequence E/S0s. Assuming a probability for an XUV-disk galaxy to be on the blue sequence equal to the overall sample blue-sequence fraction, binomial statistics yields a 46% probability of obtaining at least the number of XUV-disk galaxies observed on the blue sequence out of the total number of XUVs identified.

Likewise, if we ignore sequence dependence, we find that the XUV-disk galaxy stellar mass distribution is not significantly different from that of the parent E/S0 sample (61% probability of being drawn from the same distribution in a Kolmogorov-Smirnov test). Binning the data in mass yields a hint of a difference: the frequencies of XUV disks are 19^{+15}_{-10}% and 55^{+12}_{-13}%, respectively,

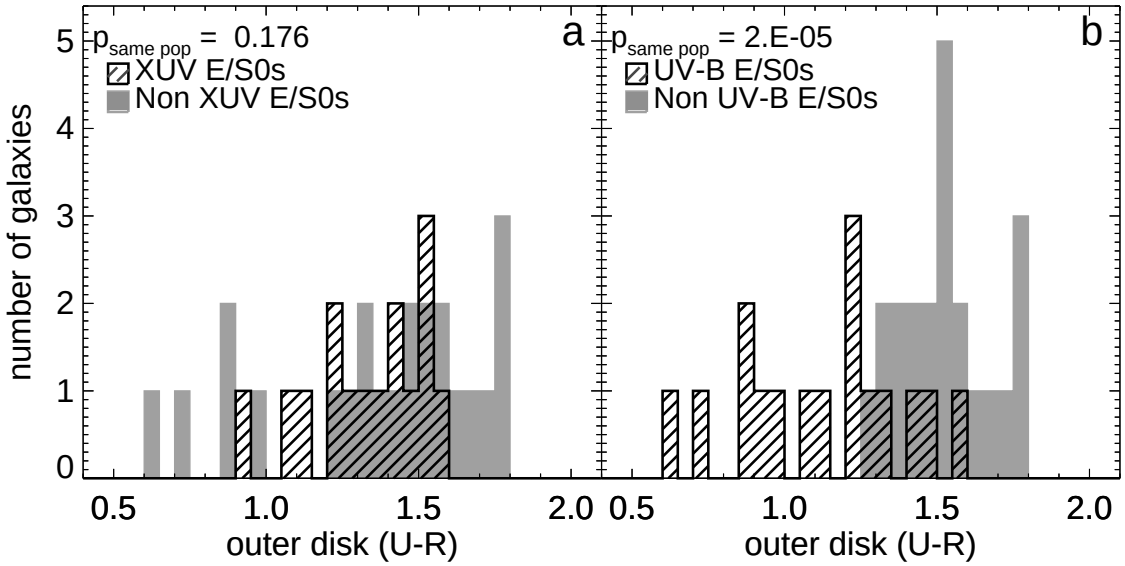

Figure 2.6 Optical outer-disk colors for sample E/S0s, calculated between the 50%–75% B-band light radii for NFGS E/S0s and between the 50%–75% g-band light radii for all others ($u-r$ color is used as a proxy for $U-R$ for non-NFGS galaxies, with a shift to $U-R$ color as applied in KGB). (a) Comparison of E/S0s with and without XUV disks, illustrating that XUV-disk E/S0s do not show bluer optical outer-disk colors than E/S0s without XUV disks, i.e., do not show enhanced outer-disk star formation. (b) Comparison of E/S0s with and without UV-B disks, illustrating that UV-B disk E/S0s *do* show bluer optical outer-disk colors than E/S0s without UV-B disks, i.e., *do* show clearly enhanced outer-disk star formation.

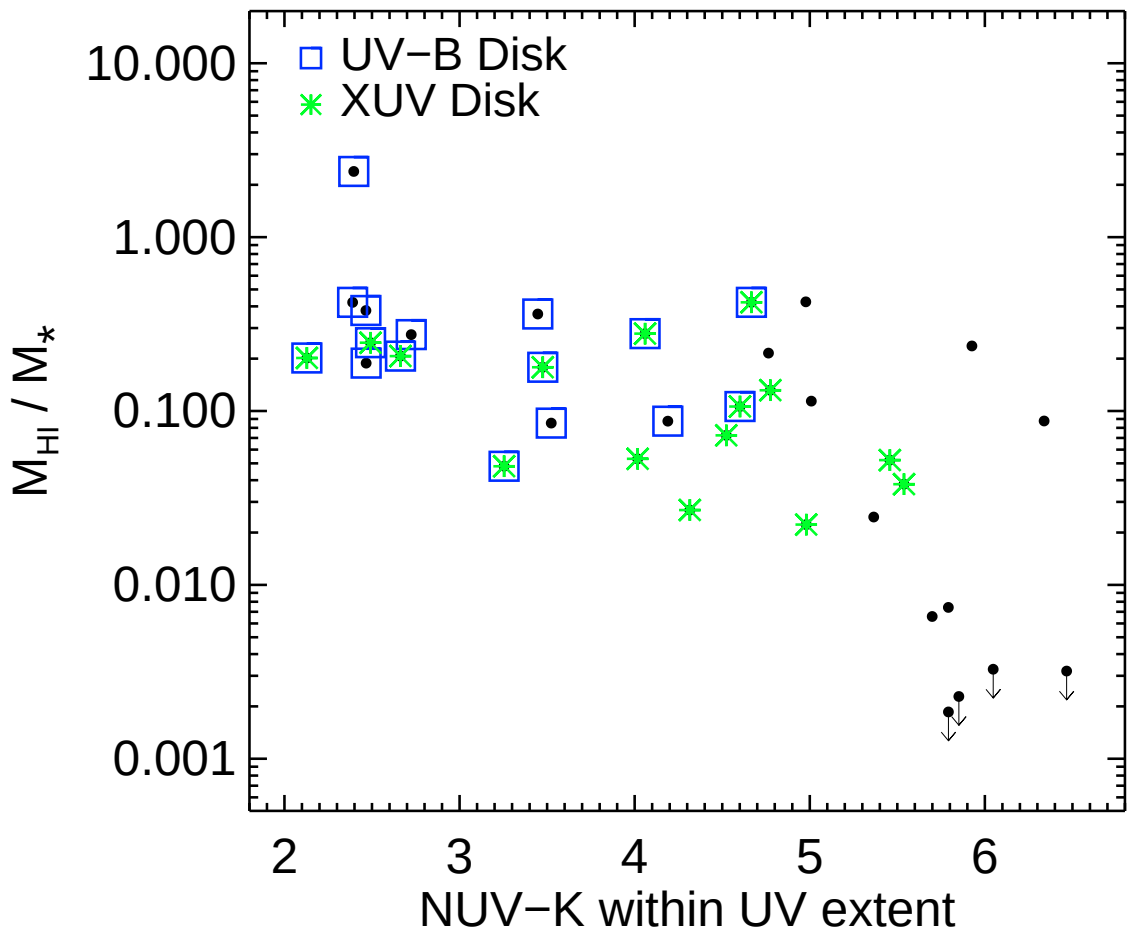

Figure 2.7 HI content versus NUV$-K$ color measured within the detected NUV extent, illustrating the trend towards enhanced HI content in UV-B disk galaxies (blue squares). Black points represent all sample galaxies with HI data ($M_{\rm H\,I}$ from references noted in Table 2.2), and green stars represent XUV disks. Note that the plotted NUV$-K$ colors are not those used for classification of either XUV or UV-B disks.

above and below $M_{\rm t}$, although the significance of this difference is not high ($\sim$1.8σ confidence).

We note that XUV disks identified according to the original T07 definition have an even more uniform color/mass distribution (Fig. 2.5). Considering the slope of the color-stellar mass sequences, this difference is consistent with what one might expect as a consequence of our purely quantitative XUV definition excluding XUV disks with the reddest colors.

2.4.3 Star Formation

Although our XUV disks reflect recent star formation, we find that they do not show substantial recent star formation as traced by blue *optical* outer-disk colors (Fig. 2.6). Likewise, the E/S0s with XUV disks do not show enhanced atomic gas content relative to the E/S0s without XUV disks, instead yielding a 36% Kolmogorov-Smirnov test probability of the same $M_{\rm H\,I}/M_*$ distribution (Fig. 2.7). These possibly counterintuitive results imply that XUV disks are not necessarily associated with strong star formation and may instead be associated with weak/incipient star formation due to a process affecting the galaxy population broadly, an idea that we return to in §2.6.

We note that the T07 requirement of different UV-optical morphology may pick out weak star formation to an even greater degree than our purely quantitative approach, since the UV-optical morphology difference could imply that the UV-detected star formation is not substantial or sustained enough to have built up an optical counterpart.

2.5 UV-B Disk Properties and Demographics

With the UV-B disk classification, we identify 16/38 or 42^{+9}_{-8}% of our sample as UV-B disks (see Table 2.2 for identifications; Figs. 2.8 and 2.9 for images of classified UV-Bs). Although we find similar frequencies of XUV and UV-B disks in our sample, and about half of the galaxies with UV-B disks also host XUV disks, the overall properties and demographics of these two classes display a number of differences, as we discuss in the following sections.

2.5.1 Extents and Ages

Similar to our quantitatively identified XUV disks, the UV-B disks we identify typically extend beyond R_{25}, with an average extent (to the last detected NUV point) of $\sim$1.4R_{25} and all extending beyond R_{25}. The average UV-B disk extent relative to the near IR is slightly larger than for XUV disks at $\sim$2.3K_{80} while the average extent relative to the UV is smaller than for XUV disks at $\sim$1.3$R_{\rm UVSF}$.

The UV-B disk FUV−NUV colors we observe are also consistent with <1 Gyr SSP ages. For UV-B disk galaxies, the average FUV−NUV color outside the optical 50% light radius is ∼0.6, which corresponds to a slightly younger ∼300 Myr SSP-equivalent age than is found for XUV disks. No UV-B disks display FUV−K colors red enough to imply SSP ages older than 1 Gyr.

2.5.2 Demographics

In contrast to the widespread distribution of XUV disks, UV-B disks are preferentially found on the blue sequence and may prefer the low-mass regime as well (see color-mass distribution in Fig. 2.5).

If we ignore mass dependence, we find clear evidence for a preference in UV-B disk incidence between red- and blue-sequence E/S0s. Assuming a probability for a UV-B disk galaxy to be on the blue sequence equal to the overall sample blue-sequence fraction, binomial statistics yields a low 0.7% probability of obtaining at least the number of UV-B disks observed on the blue sequence out of the total number of UV-Bs identified.

If we ignore sequence dependence, we find that the UV-B disk galaxy and full sample stellar mass distributions have an 8% Kolmogorov-Smirnov test probability of being drawn from the same distribution, which implies they are not conclusively distinct. Similarly, the UV-B disk frequencies we calculate are 19^{+15}_{-10}% and 59^{+12}_{-13}%, above and below $M_{\rm t}$ respectively, which are more different than in the XUV-disk case, but still only distinct at approximately 2σ confidence.

2.5.3 Star Formation

In contrast to XUV disks, the UV-B disks in our sample *do* correlate with elevated star formation as traced by blue optical outer-disk color (Fig. 2.6). E/S0s with UV-B disks also show enhanced HI content relative to E/S0s without UV-B disks (Fig. 2.7), with 0.1% Kolmogorov-Smirnov test probability of the same $M_{\rm H\,I}/M_*$ distribution. Thus, it appears that UV-B disks are closely linked to significant star formation potential and pronounced optical outer-disk star formation.

2.6 Discussion

In this section, we compare our identified XUV- and UV-B disk galaxy properties and demographics to XUV-disk and early-type galaxy formation scenarios and related literature results. We note, however, that uniform knowledge of the local and global environments of our sample galaxies would be necessary to constrain these formation scenarios and that uniform environmental data are

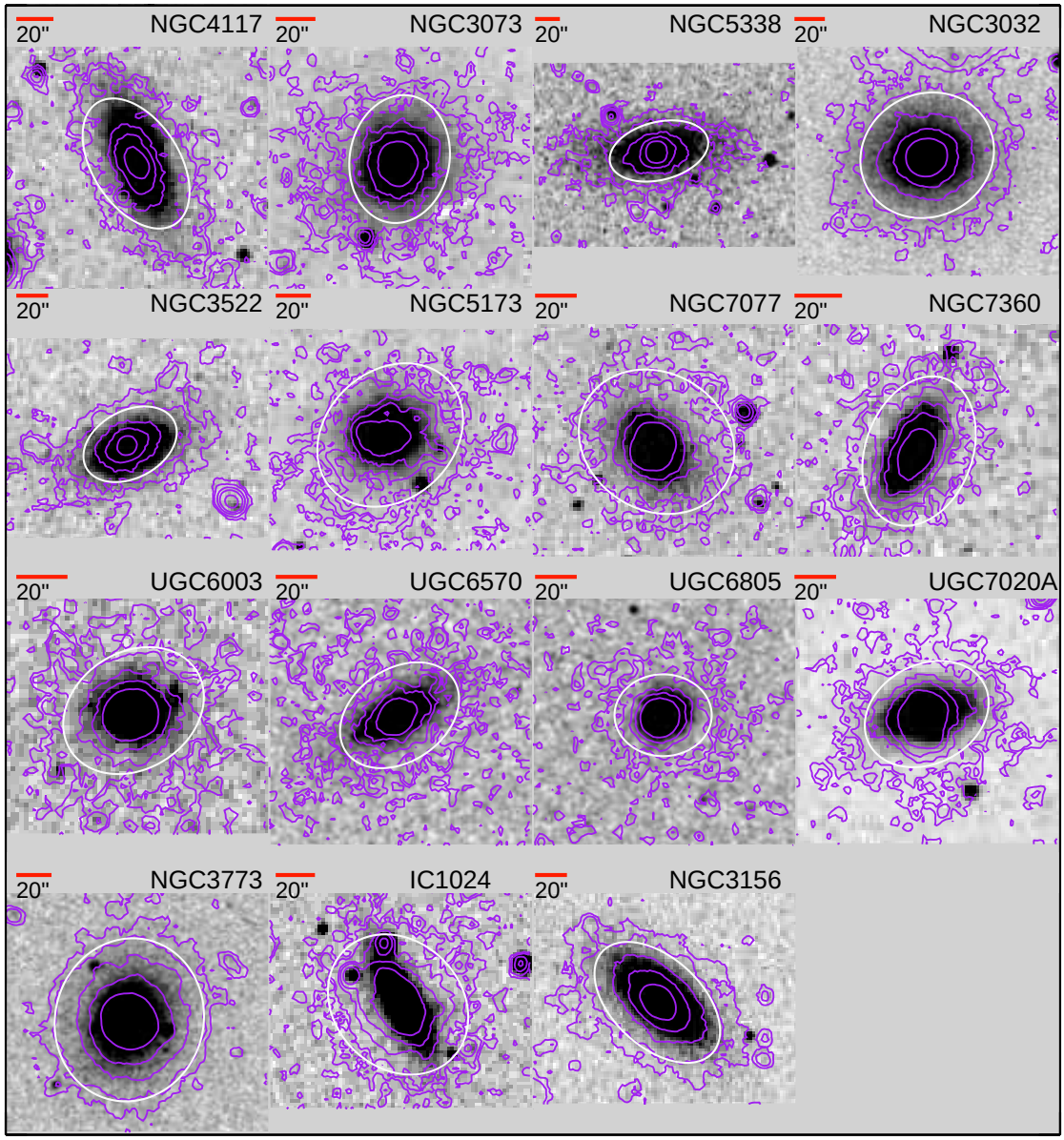

Figure 2.8 Smoothed NUV contours (purple) overlaid on DSS-II red images of XUV-disk E/S0s. $R_{\rm UVSF}$ is indicated in white, and contours start at ∼28.6 AB mag arcsec^{-2} and go up by 2×, 5×, 10×, and 25× in intensity. Eleven of these are Type 1 XUVs by the T07 definition: NGC4117, NGC3073, NGC5338, NGC3522, NGC5173, NGC7077, NGC7360, UGC6003, UGC7020A, IC1024, and NGC3156. Eight of these are also UV-Bs: NGC3073, NGC5173, NGC7077, UGC6003, UGC6805, UGC7020A, NGC3773, and IC1024.

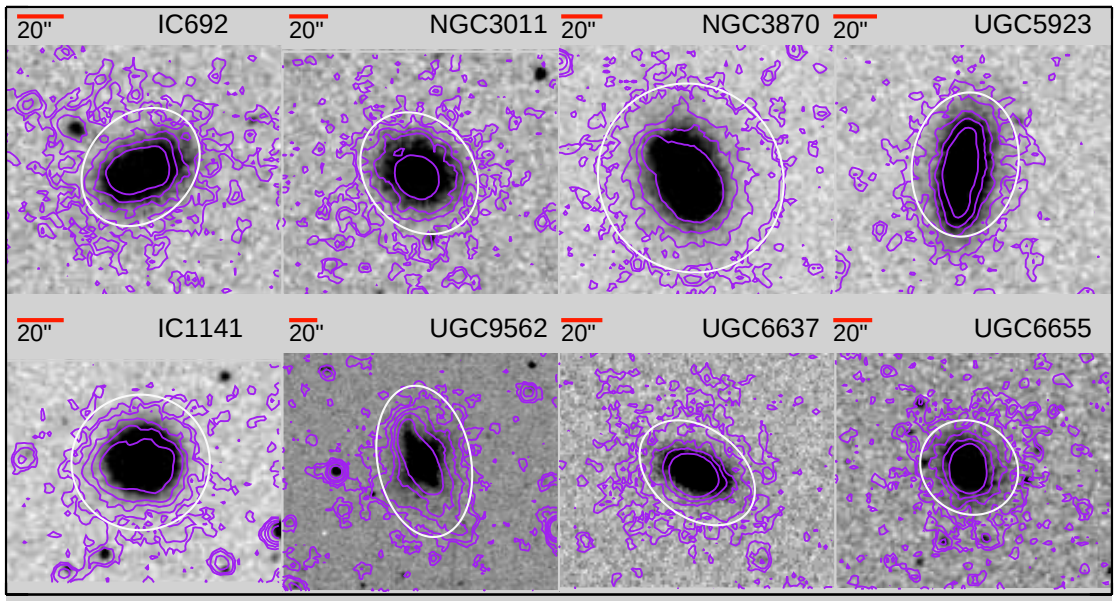

Figure 2.9 Smoothed NUV contours (purple) overlaid on DSS-II red images of UV-B disk E/S0s that are not also XUV-disk E/S0s. $R_{\rm UVSF}$ is indicated in white, and contours start at ∼28.6 AB mag arcsec^{-2} and go up by 2×, 5×, 10×, and 25× in intensity. None of these are Type 1 XUVs by the T07 definition. Some galaxies where the contours show extent beyond $R_{\rm UVSF}$ do not pass the test that this emission is $>3\sigma$ above the PSF shelf (see §2.3.2).

not available for our sample. Thus, study of the environmental properties of such galaxies is deferred to future work.

2.6.1 High Frequencies of XUV and UV-B Disks

XUV and UV-B disks occur in our sample with individually high, approximately 40% frequencies, and a combined frequency of 61±9%. Compared to classical "red and dead" expectations for early-type galaxies, the high incidence of apparent extended star formation we observe in XUV disks, with ∼70% extending beyond the optical R_{25}, is in itself a surprising result and may provide evidence against E/S0 formation through quenching processes in the low-mass, largely field regime we sample. Moreover, that we observe a similarly high incidence of UV-B disks, which seem to relate more closely to *significant* star formation, and that *all* extend past R_{25} is even more remarkable. In addition, although differences in samples and definitions complicate comparisons of absolute XUV-disk frequencies, it is intriguing that we find a frequency approximately twice the ∼20% reported in late types by T07 (see also Lemonias et al. 2011).

One possible explanation for the high incidence of XUV disks we observe in E/S0s could be a formation channel that involves mergers. Fallback of tidal tails in the late stages of a merger

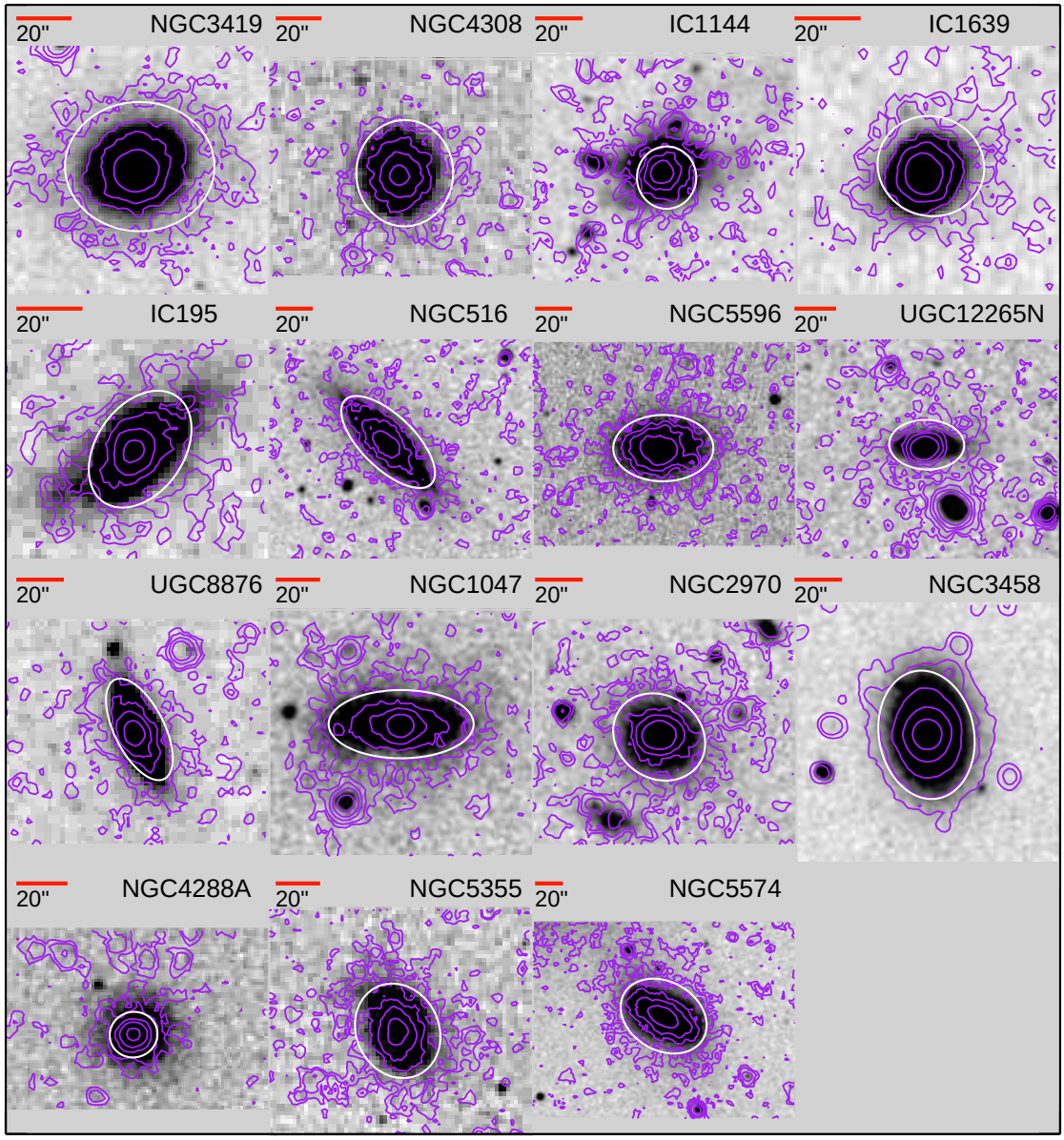

Figure 2.10 Smoothed NUV contours (purple) overlaid on DSS-II red images of E/S0s in our sample without XUV or UV-B disks. $R_{\rm UVSF}$ is indicated in white, and contours start at $\sim$28.6 AB mag arcsec^{-2} and go up by 2$\times$, 5$\times$, 10$\times$, and 25$\times$ in intensity. Five of these are Type 1 XUVs by the T07 definition: NGC3419, NGC4308, IC195, UGC8876, and NGC5355. Some galaxies where the contours show extent beyond $R_{\rm UVSF}$ do not pass the test that this emission is $>3\sigma$ above the PSF shelf (see §2.3.2).

that is major enough to produce a spheroid is a likely scenario for creating new extended disks (e.g., Barnes 2002; Naab et al. 2006). Early type galaxies at low luminosities/masses are largely "fast rotators" (as per the Emsellem et al. 2007 terminology), displaying disk-like dynamics reflecting the importance of gas in mergers related to their formation (e.g., Davies et al. 1983; Emsellem et al. 2007; KGB). Thus, if such mergers often form XUV disks, the high frequency we observe in our mass regime could be a natural consequence.

Another possible explanation for the high XUV-disk incidence in early types compared to late types, related to the inferred weak nature of XUV-disk star formation (§2.6.3), could be a bias due to the relative ease of detecting small star formation events in E/S0s. Such events may have a more detectable impact on the appearances/properties of early types than late types, where they may be obscured by generally higher levels of star formation.

2.6.2 Ubiquity of XUVs Compared to UV-Bs

The widespread distribution of the XUV disks in color and stellar mass seems to suggest an association with evolutionary processes affecting the galaxy population broadly. A potential scenario for creating extended, star-forming disks around early types is external acquisition of extended gas, whether delivered by companion interactions or fresh cosmic gas accretion, and subsequent conversion of this gas to stars. In early-type galaxies, such extended disks or rings of HI are frequently observed and often believed to be associated with external accretion (e.g., Sage & Welch 2006; Morganti et al. 2006; Oosterloo et al. 2007; Oosterloo et al. 2010).

T07 find that ∼75% of their Type 1 XUV disks show evidence for interactions or minor perturbations. An interaction scenario could explain the widespread demographics of XUVs in our E/S0s, especially since the XUVs we identify using the original T07 definition, which favors discovery of the weakest XUVs, are the most broadly distributed (Fig. 2.5). To confirm such an association, more complete knowledge of the companion statistics of our sample would be needed.

For UV-B disks, which appear to have a somewhat mass-dependent distribution, the higher UV-B disk frequency at low masses (below $M_{\rm t}$) could hint at a gas delivery mechanism with a preferred mass scale, as in the cold-accretion scenario (e.g., Birnboim & Dekel 2003; Kereš et al. 2005; Dekel & Birnboim 2006; Kereš et al. 2009). However, an in-depth examination of the environments and group properties of a larger, statistical sample of such galaxies will be necessary to distinguish between various scenarios for producing extended star formation in early types.

2.6.3 Relationship to Star Formation and HI Content

An important question to ask about the apparently young UV disks we observe around E/S0s is: are they actually associated with substantial disk growth?

The higher ($\sim$40%) frequency of XUVs in both red- and blue-sequence E/S0s vs. in late types seems to link XUV disks to a galaxy population associated with weak or inefficient star formation. Moreover, our E/S0 XUV disks do not show an association with blue optical outer-disk colors, nor with enhanced HI content (see §2.4.3). The association of XUV disks with weak or inefficient star formation is consistent with the observation of a high ($\sim$70%) rate of XUV disks in massive optically low surface brightness galaxies, which are known for inefficient star formation as well (Boissier et al. 2008). It is also consistent with T07's result associating *lower* SFR/$M_{\rm H\,I}$ with Type 1 XUV disks. In addition, simulations of XUV disks in spiral galaxies show that star formation in these objects can proceed for as long as 4 Gyr without producing enough stars to create a high surface brightness optical component (Bush et al. 2008).

In contrast, although XUV and UV-B classifications overlap, our UV-B disk galaxies as a class are characterized by bluer optical outer-disk colors and larger reservoirs of HI gas than E/S0s without UV-B disks (see §2.5.3). Thus, UV-B disks are more closely associated with significant disk star formation than are XUV disks. In addition, if we consider the blue sequence below $M_{\rm t}$, where the numbers and properties of E/S0s suggest disk building is most active (KGB), we find all sample galaxies save one are classified as UV-B disks (Fig. 2.5). This strong link between UV-B disks and the sub-$M_{\rm t}$ blue sequence seems to support the scenario of significant growth in the optical outer disks of E/S0s in this regime.

2.7 Conclusions

We have used UV, optical, and IR imaging to study extended-disk star formation in a sample of 38 red- and blue-sequence E/S0s in the stellar mass regime below $\sim 4\times10^{10}\,M_\odot$ and in primarily field environments. We introduce two new classifications: a *purely quantitative version of the Extended Ultraviolet (XUV) disk classification*, akin to the Type 1 XUV definition of Thilker et al. (2007; T07); and an *Ultraviolet-Bright (UV-B) disk classification*, with NUV$-K$ color indicating $\gtrsim$10% young population in the outer optical disk beyond the 50% light radius. We summarize key results from the application of these classifications below.

- We identify a high 61±9% combined frequency of XUV and UV-B disks. Since the classifications partially overlap, this frequency reduces to separate 39±9% and 42^{+9}_{-8}% frequencies for XUV disks and UV-B disks, respectively. In the XUV-disk case, the observed frequency is approximately twice the ∼20% reported by T07 for primarily late-type galaxies, although differences in XUV-disk criteria and possible detection biases could affect this comparison.

- UV colors of both XUV and UV-B disks typically imply <1 Gyr ages, and most of the identified UV disks extend beyond the optical R_{25} radius.

- XUV-disk host galaxies occupy a widespread distribution in color and stellar mass, while UV-B disks more strongly prefer the blue sequence and may also prefer the low-mass regime.

- XUV disks appear to be associated with *low-level* star formation, whereas UV-B disks appear to be more clearly associated with *significant* star formation. UV-B disk galaxies are also closely linked to the population of blue-sequence E/S0s in the stellar mass regime below the "gas-richness threshold mass" at $M_t \sim 5 \times 10^9\, M_\odot$ (Kannappan et al. 2009; KGB), supporting the idea that such galaxies represent an actively disk-building population (KGB).

Our results suggest that XUV-disk formation could be related to a process that affects the galaxy population broadly, such as interactions, while UV-B disk formation could be related to a process with a mass-scale preference, such as cold-mode gas accretion. Existing data do not yet allow us to disentangle such effects in the E/S0 population, but the purely quantitative classifications we have developed in this work are well suited to application in larger statistical samples, which will allow us to construct a more complete picture of the local and global environments of star-forming E/S0s. In subsequent work, we plan to combine quantitative metrics of both disk building and environment in a large volume-limited survey in order to constrain the origin and future evolution of star-forming E/S0s and further probe the intriguing possibility of early-to-late-type transformation.

We thank S. Jogee for her role in acquiring the *Spitzer* data, M. Haynes for the early release of *GALEX* imaging of NGC 3773, and the anonymous referee for suggestions that motivated substantial improvements to this work. We also thank D. Stark for helpful conversations on the topic of refining data analysis codes. We thank C. Clemens, K. Eckert, A. Leroy, M. Norris, and L. Wei for useful discussions as well. AJM acknowledges support from the NASA Harriett G. Jenkins Pre-doctoral Fellowship Program. This work uses observations made with the NASA Galaxy Evolution Explorer. *GALEX* is operated for NASA by Caltech under NASA contract NAS5-98034. We acknowledge

support from the *GALEX* Guest Investigator program under NASA grant NNX07AT33G. This work uses observations made with the *Spitzer* Space Telescope, operated by the Jet Propulsion Laboratory, Caltech under a contract with NASA. Support for this work was also provided by NASA through an award issued by JPL/Caltech. This work uses observations from the SDSS; funding for the SDSS and SDSS-II has been provided by the Alfred P. Sloan Foundation, the Participating Institutions, the National Science Foundation, the U.S. Department of Energy, the National Aeronautics and Space Administration, the Japanese Monbukagakusho, the Max Planck Society, and the Higher Education Funding Council for England. The SDSS Web Site is http://www.sdss.org/.

Table 2.2. Summary of *GALEX* GI and Archival E/S0 Sample Properties

Galaxy	$\log(M_*/M_\odot)$	Seq	Morph.	Dist.	$\log(M_{\rm H\,I}/{\rm M}_\odot)$	FUV−NUV	NUV−K	FUV−NUV	NUV−K	T07 XUV?	XUV?	UV-B?	Sample
NGC3419	10.0	B	S0-S0/a	43.4	9.1[b]	2.9	5.0	2.5	5.1	Y	N	N	GI
NGC4117	9.7	R	S0	19.0	8.3	0.5	4.7	0.7	5.1	Y	Y	N	GI
NGC3073	9.1	B	S0/a	21.1	8.5	1.6	4.5	1.5	4.4	Y	Y	Y	GI
NGC4308	8.7	R	S0	8.4	<6.0	3.1	5.4	2.3	5.6	Y	N	N	GI
IC692	8.9	B	E	21.4	8.4	0.9	2.9	0.5	2.7	N	N	Y	GI
NGC3011	9.4	B	S0/a	25.7	8.3	0.8	3.3	0.4	3.4	N	N	Y	GI
NGC3870	8.8	B	Pec	14.5	8.4	0.4	2.7	0.3	2.7	N	N	Y	GI
UGC5923	8.1	R	S0/a	8.0	7.7	1.1	3.8	0.7	3.6	N	N	Y	GI
NGC5338	8.9	R	S0	10.3	7.3	2.0	4.5	1.9	4.7	Y	Y	N	GI
IC1141	10.4	B	S0/a	68.0	9.3	0.7	3.5	0.6	4.0	N	N	Y	GI
IC1144	11.2	B	S0/a	175.4	<8.7	2.3	5.8	2.3	6.0	N	N	N	GI
IC1639	10.6	B	cE	76.0	8.4	3.1	5.3	2.0	5.7	N	N	N	GI
IC195	10.5	B	S0/a	52.1	9.4	1.9	6.2	1.9	6.2	Y	N	N	GI
UGC9562	8.9	B	S0	25.2	9.3	0.4	2.5	0.4	2.2	N	N	Y	GI
NGC3032	9.6	B	Pec	25.2	8.3	2.0	4.7	1.8	4.8	N	Y	N	GI
NGC3522	9.7	R	S0	22.9	8.4	2.1	4.9	2.0	5.1	Y	Y	N	GI
NGC516	10.1	R	S0	34.9	<7.4	2.8	5.6	2.2	5.8	N	N	N	GI
NGC5173	10.3	B	E	41.2	9.3	0.8	3.9	0.7	4.2	Y	Y	Y	GI
NGC5596	10.4	R	S0	50.8	8.8	1.2	5.5	0.6	5.2	N	N	N	GI
NGC7077	8.8	B	S0/a	18.9	8.2	2.1	3.1	0.7	3.0	Y	Y	Y	GI
NGC7360	10.5	B	E	67.9	9.6	0.6	4.4	0.6	4.5	Y	Y	N	GI
UGC12265N	10.1	B	S0	82.8	9.4	1.1	4.7	1.0	4.8	N	N	N	GI
UGC6003	10.1	B	S0/a	84.2	9.4	1.5	1.9	0.8	2.7	Y	Y	Y	GI
UGC6570	9.6	R	S0/a	28.6	8.4	1.4	4.5	1.0	4.6	N	Y	N	GI
UGC6637	9.2	B	S0	31.5	8.6	0.8	3.7	0.3	2.9	N	N	Y	GI
UGC6655	8.0	B	S0	8.8	7.2	0.8	3.4	0.3	2.8	N	N	Y	GI

Table 2.2 (cont'd)

Galaxy	$\log(M_*/M_\odot)$	Seq	Morph.	Dist.	$\log(M_{\rm H\,I}/{\rm M}_\odot)$	FUV−NUV	NUV−K	FUV−NUV	NUV−K	T07 XUV?	XUV?	UV-B?	Sample
UGC6805	8.9	B	S0	20.3	7.6	1.3	3.9	0.6	3.5	N	Y	Y	GI
UGC7020A	9.3	R	S0	26.7	8.6	0.7	3.5	0.6	3.5	Y	Y	Y	GI
UGC8876	10.2	R	S0/a	36.7	<7.7	1.6	6.3	1.5	6.4	Y	N	N	GI
NGC3773	8.6	B	Pec	10.5	7.9	··· [c]	3.4	··· [c]	3.2	N	Y	Y	GI
IC1024	9.4	B	S0Pec	20.4	9.0[b]	0.8	4.0	0.7	4.3	Y	Y	Y	archival
NGC1047	9.0	R	S0/a	19.1	8.7[b]	2.3	5.3	2.5	5.2	N	N	N	archival
NGC2970	9.3	R	S0/a	22.7	··· [a]	2.4	5.2	2.0	5.2	N	N	N	archival
NGC3156	9.6	R	S0	15.3	7.9[b]	2.6	4.9	2.4	5.1	Y	Y	N	archival
NGC3458	10.4	R	S0	27.6	··· [a]	1.9	6.2	1.7	6.5	N	N	N	archival
NGC4288A	10.4	R	S0	100.8	··· [a]	1.4	6.1	1.1	5.9	N	N	N	archival
NGC5355	10.1	R	S0/a-S0Pec	34.4	9.5[b]	··· [c]	5.7	··· [c]	5.8	Y	N	N	archival
NGC5574	10.0	R	S0/a	23.2	7.9[b]	2.0	5.7	2.3	5.7	N	N	N	archival

Note. — Derived FUV−NUV and NUV−K colors outside $R_{\rm UVSF}$ and beyond the optical 50% light radius (the XUV-disk and UV-B disk classification regions, respectively) plus ancillary data and classifications using the original T07 XUV-disk definition, our purely quantitative XUV-disk definition, and the UV-B disk definition. Ancillary data are from Jansen et al. (2000a,b), KGB, and Wei et al. (2010) except as noted. Distances assume H_0=70 km s^{-1} Mpc^{-1}. [a] HI data unavailable. [b] HI data from HyperLeda (Paturel et al. 2003). [c] No FUV imaging available.

CHAPTER 3: ECO AND RESOLVE: GALAXY DISK GROWTH IN ENVIRONMENTAL CONTEXT

We study the relationships between galaxy properties related to disk (re)growth and galaxy environments by considering two highly complete samples that are approximately baryonic mass limited into the high-mass dwarf galaxy regime, the Environmental COntext (ECO) catalog (data release herein) and the B-semester region of the REsolved Spectroscopy Of a Local VolumE (RESOLVE) survey. We quantify galaxy environments using both group identification and smoothed galaxy density field methods. We use by-eye and quantitative morphological classifications plus atomic gas content measurements and estimates. We find that blue early-type (E/S0) galaxies, gas-dominated galaxies, and UV-bright disk host galaxies all become distinctly more common below group halo mass $\sim 10^{11.5} M_{\odot}$, implying that this low group halo mass regime may be a preferred regime for significant disk growth activity. We also find that blue early-type and blue late-type galaxies inhabit environments of similar group halo mass at constant baryonic mass, consistent with a scenario in which blue early types can regrow late-type disks. Furthermore, for all early and late type central galaxies with baryonic mass $\lesssim 10^{10} M_{\odot}$, we find no relationship between group halo mass and morphology. The observed morphology-environment relation, with environment quantified by group halo mass and with late-type fractions rising at low group halo mass, is likewise consistent with expectations from a scenario in which disk regrowth occurs preferentially at low group halo mass. This relation does not, however, require such a scenario; a similar trend is expected if disk destruction/quenching occurs preferentially at high halo mass (and of necessity predominantly affects satellites).

3.1 Introduction

For decades, astronomers have observed that the properties of galaxies in the local universe, including appearance, star formation rate, and gas content, depend on the surrounding environment (e.g., as reviewed by Bower & Balogh 2004; Boselli & Gavazzi 2006). Galaxies of different morphological types, in particular, have long been seen to preferentially congregate in different environments (e.g., Hubble & Humason 1931; Davis & Geller 1976). Dressler (1980) reported the

so-called "morphology-density relation," whereby E/S0 fractions increase with increasing environmental density within rich clusters while spiral fractions decrease. Postman & Geller (1984) showed that a similar relationship between galaxy morphology and local density also holds in the lower-density group environment. However, several authors found the conflicting result that significant variation in morphology with environment exists only in the richest clusters (e.g., Maia & da Costa 1990; Whitmore 1995). Notwithstanding these early disagreements, the original Postman & Geller (1984) observation of a morphology-density relation extending into less-rich environments has since been corroborated by a variety of other authors (e.g., Tran et al. 2001; Helsdon & Ponman 2003; Goto et al. 2003; Calvi et al. 2012).

Recently, it has also been noted that the mass ranges of galaxies considered can have a significant impact on the observed form of the morphology-density relation (e.g., Bamford et al. 2009; Calvi et al. 2012; Wilman & Erwin 2012). While Drinkwater et al. (2001) observe a traditional morphology-density relation in the dwarf galaxy population within a single cluster, other studies find that the morphology-density relation takes on different forms for low-to-intermediate mass galaxies. Kannappan et al. (2009, hereafter KGB) find suggestive evidence that low-to-intermediate stellar mass E/S0s occupy low density environments similar to those of spirals at the same masses, while Calvi et al. (2012) find that morphologies for intermediate mass galaxies are not closely related to environment, except in clusters. Interestingly, Hogg et al. (2003) find that the mean environmental overdensity for red, typically assumed to be early-type (E/S0), galaxies reaches a minimum at intermediate masses/luminosities (around L_*). The conflation of morphology and color, of course, complicates interpretation of the Hogg et al. result, since both optically red, "passive" spiral galaxies (e.g., van den Bergh 1976; Couch et al. 1998; Dressler et al. 1999; Poggianti et al. 1999) and optically blue E/S0 galaxies (e.g., KGB; Schawinski et al. 2009) are known components of the galaxy population.

It is likely that the existence of such non-traditional color-morphology pairings in the galaxy population is an important factor driving the observation that trends in galaxy color (or more direct star formation property measures) versus environment can differ from observed morphology-density trends. Beginning with the analysis of Kennicutt (1983), it has often been observed that cluster galaxies show typically lower levels of star formation than galaxies in less rich environments. Several authors have subsequently found that such star formation or color trends with environment cannot be completely explained by the presence of morphology-density trends (e.g., Koopmann & Kenney 1998; Lewis et al. 2002; Christlein & Zabludoff 2005; Welikala et al. 2009). Others have taken this

conclusion further, inferring that trends in star formation/color are actually more closely linked to environmental conditions than are trends in structural/morphological parameters (e.g., Blanton et al. 2003; Kauffmann et al. 2004; Blanton et al. 2005; Quintero et al. 2006; Bamford et al. 2009; Skibba et al. 2009).

Galaxy gas content is another property that has been observed to share a close link to both star formation and the ambient environmental conditions around galaxies. First observed by Davies & Lewis (1973) for galaxies in the Virgo Cluster, the result is now well established that cluster galaxy populations typically display lower levels of atomic gas than do similar populations in less dense environments (e.g., Giovanelli & Haynes 1983; Haynes et al. 1984; Giovanelli & Haynes 1985; Gavazzi 1987; Bravo-Alfaro et al. 2000; Solanes et al. 2001; see also review by van Gorkom 2004). Likewise, cluster galaxies are typically observed to have HI gas disks that are less extended than those in lower density environments (e.g., Giovanelli & Haynes 1983; Warmels 1988; Cayatte et al. 1994; Bravo-Alfaro et al. 2000). Galaxy gas properties can apparently be affected by the conditions present in lower density environments as well, e.g., as shown in the simulations of Kawata & Mulchaey (2008) where "strangulation" or stripping of a hot galaxy halo gas component, which could otherwise cool to provide a cold gas reservoir, in a larger potential is effective in a group environment with halo mass $\sim 10^{12.9}\,M_{\odot}$. Still further down the environmental density scale, gas-rich galaxies have been observed to be one of the most weakly clustered galaxy populations, that is, typically found in the lowest density environments (Basilakos et al. 2007; Meyer et al. 2007; Martin et al. 2012; Li et al. 2012). This observation could be related to the finding from multiple theoretical studies that gas accretion into galaxies, whether in a "cold" or "hot" mode, is most effective where group halo masses are low (e.g., Birnboim & Dekel 2003; Kereš et al. 2005; Dekel & Birnboim 2006; Kereš et al. 2009; Nelson et al. 2013).

In the prevailing hierarchical model of galaxy evolution, galaxies are thought to experience morphological transformations not just from late to early type, for example through merging/quenching processes, but also potentially from early to late type, through a disk *regrowth* process that may be enabled by gas accretion (e.g., Barnes 2002; Steinmetz & Navarro 2002; Governato et al. 2007). Observationally, the operation of such a disk regrowth process is difficult to confirm.

However, several hints have recently emerged that such a scenario is plausible. One such hint lies in the existence of the blue or "blue-sequence" E/S0 population, consisting of morphologically early type galaxies that lie on the blue sequence in color-stellar mass space. Blue-sequence E/S0s are typically found in non-cluster environments and exist primarily at stellar masses less than $\sim 10^{10.5}\,M_{\odot}$

(the bimodality mass of Kauffmann et al. 2007, hereafter M_b) but are most common below the "gas-richness threshold" stellar mass of $\sim 10^{9.7} M_\odot$ (KGB). Kannappan et al. (2013, hereafter K13) argue that the bimodality and gas-richness threshold mass scales mark two distinct transition points between galaxy refueling regimes, with galaxies below the threshold scale typically experiencing high levels of external gas accretion and stellar mass growth. Consistent with this picture, low-mass blue E/S0s contain sufficient gas reservoirs and specific star formation rates to allow the growth of evolutionarily significant disk structures on relatively short timescales (KGB; Wei et al. 2010). Another hint of disk regrowth in E/S0s is the observation of extended UV emission, associated with recent star formation, around a number of nearby galaxies with early-type morphology (e.g., Donovan et al. 2009; Cortese & Hughes 2009; Thilker et al. 2010; Moffett et al. 2012). Moffett et al. (2012) observe that such extended UV structures are common in low-to-intermediate mass early-type galaxies and that a particular class of "UV-Bright" or UV-B disk galaxies is marked by a high potential for ongoing star formation. Linking these two populations together, UV-B disks are also strongly associated with the low-mass, blue-sequence E/S0 population, supporting the idea that these galaxies may be engaged in disk regrowth. Stark et al. (2013) report evidence for gas as well as stellar disk regrowth in such low-mass E/S0 galaxies.

In this contribution, we employ two unusually complete volume-limited galaxy samples, both of which extend into the "high-mass" dwarf galaxy regime (reaching baryonic masses $\sim 10^{9.3} M_\odot$), to probe disk (re)growth in a variety of environments. We seek to answer three major questions. (1) Does environment play a role in enabling gas or stellar disk growth? (2) Does the morphology-density, or more generally morphology-environment, relation behave as might be expected if disk regrowth is effective in transforming galaxy morphology? In particular, are the typical environments for blue early- and late-type galaxies similar in the galaxy mass regimes in which disk regrowth occurs? (3) Are there specific group halo mass scales implicated in evidence for disk regrowth?

We address these questions in part by examining the detailed form of the morphology-environment relation, including possible variations with galaxy mass scale and central/satellite designations. In addition, we consider an alternative way of formulating a morphology-environment relation. If the traditional formulation of the morphology-environment relation can be considered to quantify the probability of a galaxy exhibiting a particular morphology given some environment, P(M|E), then an alternative way to frame this relation is to quantify the probability of a galaxy inhabiting a particular environment given its morphology, P(E|M). This alternative formulation provides a useful framework for understanding the typical environments of galaxies with different morphologies.

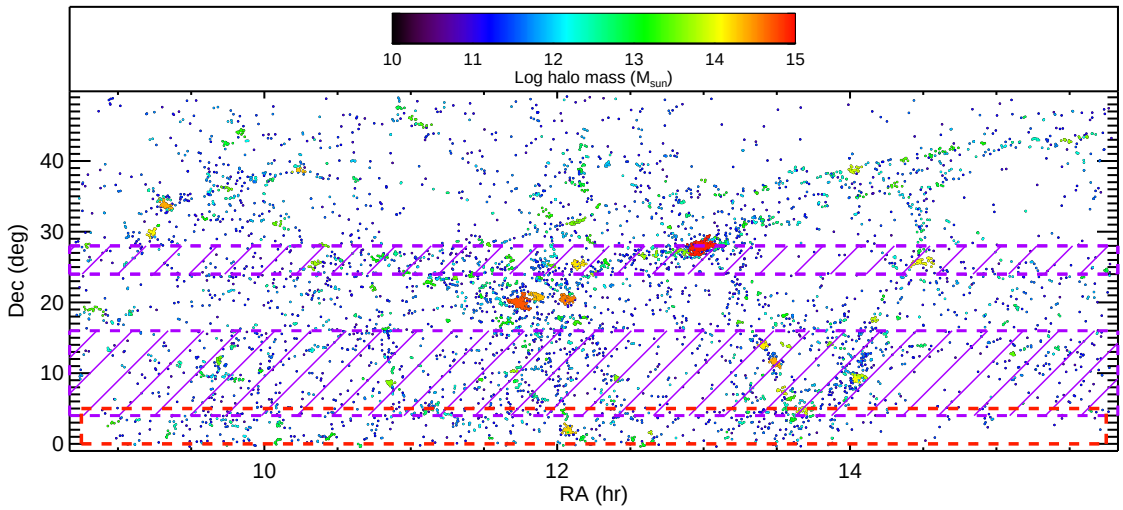

Figure 3.1 The ECO catalog region in sky coordinates, with color coding according to group halo masses estimated as described in §3.3.6. The RESOLVE-A region is outlined in red, and the region of overlap with the ALFALFA α.40 catalog (Haynes et al. 2011) is indicated by the purple crosshatched strips.

We further examine the typical environments of different classes of galaxies linked to disk growth, including blue-sequence early types, galaxies with substantial atomic gas reservoirs, and early-type galaxies that display recent UV-detected disk star formation.

We begin by introducing the galaxy samples under consideration in §3.2. In §3.3, we describe our main data analysis methods. In §3.4, we report a variety of results from this analysis, including the observed forms of both the traditional and alternative morphology-environment relations, in particular finding that the morphology-environment relation disappears for low baryonic mass central galaxies. We also find that blue-sequence early type, gas-dominated, and disk-growing populations rise in prominence in environments with $M_{halo} \lesssim 10^{11.5} M_{\odot}$. In §3.5, we show that the forms of both the traditional and alternative morphology-environment relations we observe are consistent with expectations of the disk regrowth model and discuss the idea that the low group halo mass regime below $\sim 10^{11.5} M_{\odot}$ appears to be a preferred regime for disk growth. Finally, we provide a brief summary of our major results in §3.6.

3.2 Samples

3.2.1 ECO catalog

The ECO, or Environmental COntext, catalog is the largest sample we consider and includes the greatest diversity of galaxy environments (see Table 3.1 for detailed ECO galaxy properties). The

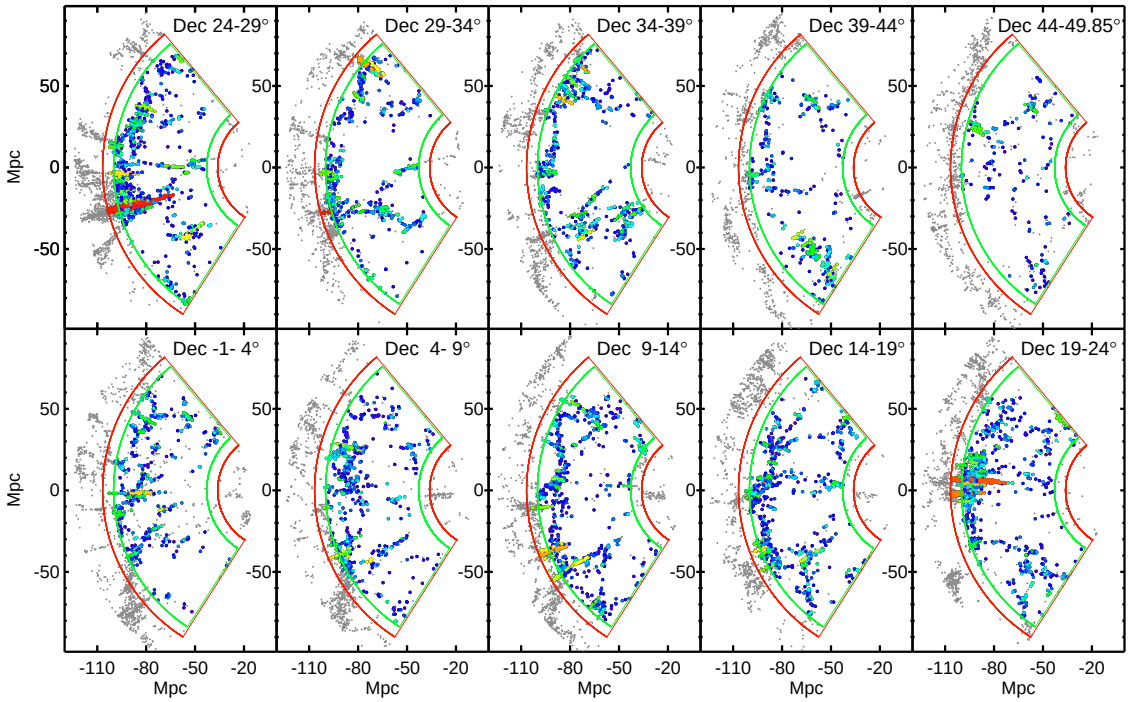

Figure 3.2 The ECO catalog region in RA vs. line-of-sight distance coordinates, in slices of ∼5 degrees in Dec, increasing from the bottom left panel. Galaxies included in the final ECO sample analyzed here are indicated by dots color-coded according to their group halo masses as in Fig. 3.1, while galaxies outside this sample but present in our merged parent redshift catalog are indicated by grey dots. The outer limits of the ECO catalog "buffer" region are outlined in red, and the region of ECO we consider interior to this buffer is indicated in green.

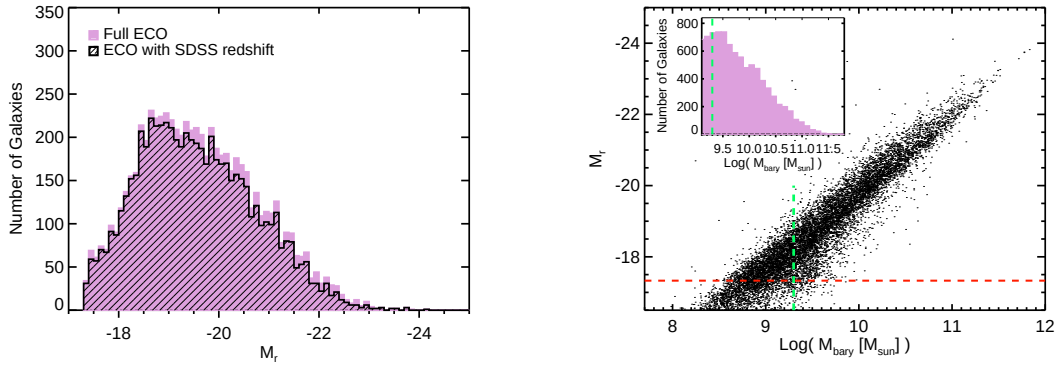

Figure 3.3 Illustration of the completeness and selection of the ECO catalog. Panel *a* shows the additional completeness of the ECO catalog over the SDSS redshift catalog. The M_r distribution of the full ECO sample in our reprocessed magnitude system (see §3.3.1 for details) is indicated by the purple solid histogram, and the distribution of ECO galaxies that have SDSS redshifts is indicated by the black hashed histogram. Panel *b* shows the M_r and M_{bary} distributions of the initial ECO catalog (dots and purple inset M_{bary} histogram), where the horizontal red line indicates the $M_r < -17.33$ redshift completeness limit and the vertical green lines indicate the final mass cut we adopt to create an approximately baryonic mass limited sample to $M_{bary} > 10^{9.3} M_{\odot}$.

ECO catalog region was chosen as the largest contiguous region on-sky where the highly complete Updated Zwicky Catalog (UZC; Falco et al. 1999) and Sloan Digital Sky Survey (SDSS; York et al. 2000) redshift databases overlap, allowing objects not present in either one to be recovered through inclusion of the other, with SDSS typically providing redshifts for fainter objects than the UZC. Though defined by the overlap of these two catalogs, the ECO catalog also incorporates redshifts from the REsolved Spectroscopy Of a Local VolumE (RESOLVE; Kannappan et al., in prep.), HyperLEDA (Paturel et al. 2003), GAMA (Driver et al. 2011), 2dF (Colless et al. 2001), and 6dF (Jones et al. 2009) surveys. The ECO region was also selected to enclose the RESOLVE A-semester survey volume plus a minimum 1 Mpc "buffer" in all directions (see sky coverage in Fig. 3.1). This buffer region, chosen with a size comparable to typical halo virial radii at the present epoch, exists to mitigate potential edge effects in calculating galaxy environment metrics, such that only galaxies in the buffer region should have environmental measures strongly affected by the loss of nearby galaxies outside the catalog boundaries. The far side limit of 7470 km/s was selected to encompass both the aforementioned 1 Mpc (equivalent to 70 km/s for $H_0 = 70\ km\ s^{-1}\ Mpc^{-1}$) buffer beyond the RESOLVE cz limit of 7000 km/s and an additional allowance to compensate for group peculiar velocities up to 400 km/s. The near side buffer zone cz limit of 2530 km/s was similarly chosen to expand the ECO volume as much as possible beyond the near-side RESOLVE cz limit of 4500 km/s while avoiding the effects of Virgo Cluster region velocity-space distortions (see Fig. 3.2). We

consider the velocity limits of the non-buffer ECO volume to be 470 km/s away from the buffer edges, or 3000 km/s $< cz <$ 7000 km/s.

The ECO catalog represents a cross match between sources with measured redshifts found in the UZC, SDSS (including data releases 6, 7, and 8; Adelman-McCarthy et al. 2008; Abazajian et al. 2009; Aihara et al. 2011), HyperLEDA, RESOLVE, GAMA, 2dF, and 6dF catalogs with a 15" matching radius on sky. New sources are added to ECO from each of the constituent catalogs whenever they do not match to a previously included ECO source. The resulting catalog has also been inspected by eye for duplicate entries caused either by "shredding" of SDSS photometric objects into multiple galaxy pieces (as described in Abazajian et al. 2004) or by centering/coordinate errors occasionally larger than the cross-matching radius. Such duplicate entries, making up $\sim$5% of the galaxies originally considered for inclusion, have been removed from our catalog. As illustrated in Fig. 3.3a, the majority of ECO galaxies are present in the SDSS redshift survey, but the number of galaxies added from other sources is significant, at approximately 7% of the final catalog.

Initially, sources with measured positions and redshifts inside the ECO volume are considered for potential membership regardless of any previously measured catalog magnitudes they may or may not have. We then use custom photometric measurements performed on SDSS imaging frames for all such potential ECO members (see §3.3.1 and Eckert et al., in prep.) to determine a defining magnitude limit for the ECO catalog. The completeness limit of the SDSS redshift survey at 7000 km/s is $M_r = -17.23$ (in DR7 catalog Petrosian magnitudes corrected for foreground extinction), and our reprocessed magnitudes are typically brighter than the SDSS catalog values by approximately 0.1 mag (see §3.3.1 for details). Thus, a potential completeness limit for the ECO catalog motivated by the SDSS completeness would be $M_r < -17.33$, which we use to produce an initial group catalog as described in §3.3.6. However, we seek to create a baryonic mass limited final sample for our analysis, where baryonic mass (M_{bary}) is defined here as stellar plus atomic gas mass and estimated as described in §3.3.2 and 3.3.7. As illustrated in Fig. 3.3b, within the confines of the $M_r = -17.33$ magnitude completeness limit, we can construct an approximately baryonic mass limited sample with $M_{bary} > 10^{9.3} M_\odot$ while leaving aside only a relatively small number of high mass-to-light ratio objects.

The final ECO sample we analyze meets both the above limit and the additional criterion that the center of the *group* to which each galaxy belongs (see §3.3.6 for details of group membership determination) must lie within the limits of the non-buffer region of ECO, that is, the group center must have 3000 km/s $< cz <$ 7000 km/s and RA/Dec $>$ 1Mpc from the buffer edges on sky at its

redshift (see Fig. 3.2)[1]. This final sample contains 6908 galaxies.

Two partially overlapping subregions of the ECO catalog are given special attention in this paper. The "ECO+A" region is defined by the overlap of the ECO catalog and public Arecibo Legacy Fast ALFA (ALFALFA) α.40 catalog (Haynes et al. 2011) and represents the portion of the ECO sample for which direct HI mass determinations are available and used in our analysis (see Fig. 3.1). The "ECO+G" subsample is defined by the availability of archival *GALEX* imaging (Morrissey et al. 2007; *GALEX* MAST GR6/7 archive at `http://galex.stsci.edu/GR6/`) with exposure times >1000s in the NUV band, sufficient to detect extended UV disk structures (e.g., Thilker et al. 2007). Since *GALEX* imaging coverage over the ECO sky region is patchy, we select multiple fully covered subregions of ECO as our final ECO+G subsample, largely coincident with RESOLVE-A but extending to larger Dec and including several slices through rich clusters. Together these regions closely reflect the full ECO environment distribution (see Fig. 3.4).

3.2.2 RESOLVE-B

The B-semester region of the RESOLVE survey, which covers most of the SDSS "Stripe 82" region, is used as a comparison sample in this analysis. The RESOLVE-B region environment distribution is illustrated in Fig. 3.4, where primary differences compared to ECO are the lack of $M_{halo} \gtrsim 10^{13.5} M_{\odot}$ groups while $M_{halo} \sim 10^{13} M_{\odot}$ groups are overrepresented in RESOLVE-B. The RESOLVE-B subsample has the advantage of greater completeness than the ECO catalog, due to deeper SDSS imaging and redshift coverage, plus the further redshift completion efforts of the RESOLVE survey. By comparison with this extra-complete sample, we assess the effects of incompleteness and derive completeness corrections that can be applied to ECO (median correction ∼2%; see §3.3.8). For all galaxies in RESOLVE-B, morphological classification has been performed by a team of classifiers, providing both the basis for calibration of, and a comparison to, the quantitative morphological classifications used for ECO (see §3.3.4; RESOLVE classification details in Appendix A).

3.3 Methods

In this section, we describe our methods of custom photometric processing, galaxy color and stellar mass estimation, galaxy morphology and UV disk classification, environment metric calculation,

[1]Note that we do not recalculate galaxy M_r values by considering galaxies to lie at their group center redshifts. We find this recalculation would make a negligible difference in our overall sample membership.

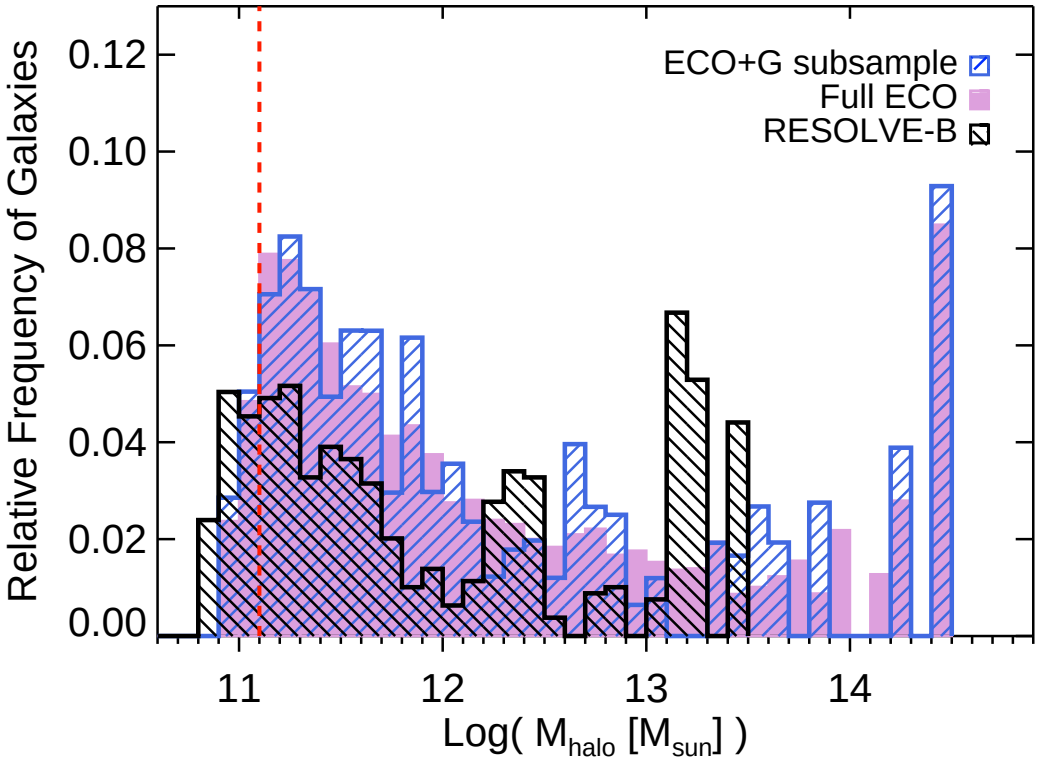

Figure 3.4 The distribution of galaxies by halo mass in the ECO, ECO+G, and RESOLVE-B samples, with completeness correction factors applied. The red dashed vertical line indicates the halo mass completeness limit for ECO. We have selected the ECO+G sample to have a similar environment distribution to the full ECO sample.

atomic gas mass estimation, and correction for the incompleteness of the ECO sample. Throughout our analysis, we calculate distances according to $D = cz/H_0$ and take $H_0 = 70\ km\ s^{-1}\ Mpc^{-1}$ unless otherwise noted. We estimate binomial confidence intervals on population proportions according to the Bayesian approach of Cameron (2011).

3.3.1 Imaging/Photometry

As a result of the problematic nature of obtaining accurate estimates of galaxy properties with bulk SDSS pipeline-processed data and our desire to study spatially resolved parameters not necessarily computed in catalog data products, we have undertaken a custom reprocessing of SDSS, 2MASS, and *GALEX* imaging for all ECO sample galaxies considered here. The ECO photometric reprocessing mimics the methods developed for the RESOLVE survey (see Eckert et al., in prep. for full details).

To summarize this reprocessing: we retrieve imaging frames in $ugriz$, JHK, and NUV bands via automated queries to the SDSS DR8 (Aihara et al. 2011), 2MASS (Skrutskie et al. 2006), and *GALEX* (Morrissey et al. 2007) archives respectively. Greater than 99% of our galaxies are covered by 2MASS and ∼30% by *GALEX*. Photometric processing proceeds first on the SDSS imaging, where SExtractor (Bertin & Arnouts 1996) is called to identify sources from an r-band image and create a corresponding mask image wherein sources other than the target are masked. SExtractor parameters for the target galaxy are then used as an initial input to the IRAF *ellipse* task, which fits the galaxy isophotes in a co-added gri image while allowing the PA and ellipticity to vary. From this free ellipse fit, an optimal ellipticity and PA corresponding to the outer disk is determined. A fixed ellipse fit is then performed, using these outer-disk parameters, on the images in all bands individually. Total magnitudes are determined from the resulting profiles by several methods: large aperture summation, exponential disk fitting, curve-of-growth extrapolation, and outer-disk color correction (see Eckert et al., in prep.). Comparing the results of these methods yields an estimate of the systematic errors, which are combined with the purely photometric errors to obtain the final magnitude error estimates.

The automated SExtractor masking procedure has been tuned to give reasonable results for the majority of galaxies, but it is possible for the automatically generated masks to either mask parts of the galaxy under consideration or fail to mask nearby sources not associated with the target galaxy. To identify potentially problematic masks, we flag objects for which the magnitude estimation procedure has failed, the extracted r-band profile signal does not rise above eight times

the sky noise, or the r-band profile does not extend beyond the calculated r-band 90% light radius. These mask images flagged as potentially problematic are inspected by eye and edited by hand where necessary to better reflect distinctions between the target galaxy and other nearby sources.

3.3.2 Color and Stellar Mass Estimation

Using the full complement of total magnitudes, including NUV where available, galaxy stellar masses are estimated from a spectral energy distribution (SED) fitting procedure. We use a recently updated version of the likelihood-based stellar mass estimation code of Kannappan & Gawiser (2007), which is described fully by K13. This procedure uses a suite of composite stellar population models constructed from old and young Bruzual & Charlot (2003) stellar populations. These model stellar populations are combined in various fractions by mass, with 13 allowable young population fractions of 0.001, 0.002, 0.005, 0.011, 0.025, 0.053, 0.112, 0.220, 0.387, 0.585, 0.760, 0.876, and 0.941. Four possible metallicities (Z = 0.004, 0.008, 0.02, and 0.05) and 11 possible extinction values ($\tau_V = 0$, 0.12, 0.24...1.2) are also used. The young population model grid is constructed to simulate both continuous and bursty star formation histories by including models with constant star formation from 1015 Myr in the past to various end points 0-195 Myr in the past and simple stellar populations (SSPs) with ages 360, 509, 641, 806, and 1015 Myr. The old population model grid includes SSPs with ages 2, 4, 6, 8, 10, and 12 Gyr. A Chabrier initial mass function (Chabrier 2003) is used in these calculations, which yield a stellar mass zero point consistent with that of Kauffmann et al. (2003). The code also outputs internal extinction corrected model fit colors, which more cleanly separate the red- and blue-sequence galaxies than raw measured colors, and we designate these colors with a superscript "e". We also use model fit colors without any internal extinction correction, denoted with superscript "model".

3.3.3 The Red and Blue Sequences

To separate red- and blue-sequence galaxies, we choose a dividing line between the red and blue color stellar mass loci defined by our extinction-corrected colors and stellar mass estimates (see Fig. 3.5). We determine this division based on double Gaussian fits to the red- and blue-sequence color distributions in two high and low stellar mass regimes where the sequences are well defined ($\log M_* < 9.5$ and $\log M_* > 9.5$). Our divider is then defined by the color halfway between the fit peaks and the median stellar mass in each mass regime. The slanted divider in the intermediate mass regime is defined by the line connecting these two Gaussian-fit-determined points. The equation of

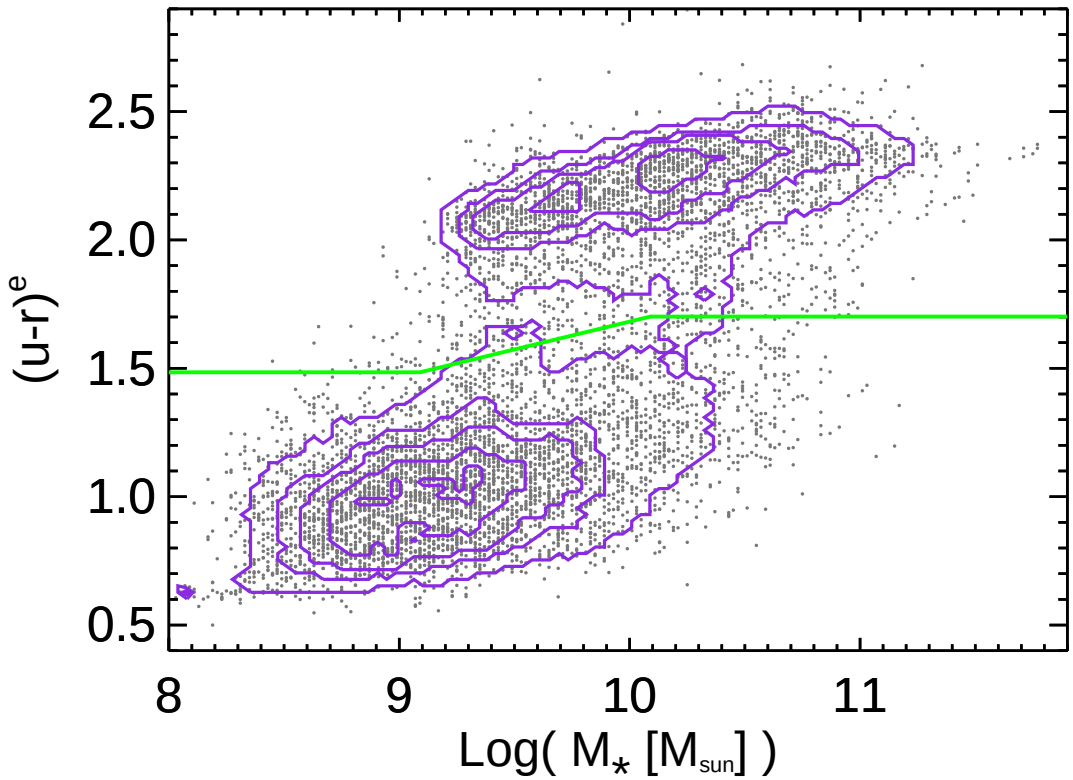

Figure 3.5 Color vs. stellar mass for the ECO catalog sample, where $(u-r)^e$ represents an internal extinction corrected color derived from the SED fitting code (see §3.3.2). Dark grey points indicate individual galaxies and density contours of this distribution are shown in purple. The green line indicates our chosen red/blue sequence divider (§3.3.3).

the divider is:

$$(u-r)^e = \begin{cases} 1.484 & \log M_* \leq 9 \\ 0.22 \times \log M_* - 0.5 & 9 < \log M_* < 10.1 \\ 1.7 & \log M_* \geq 10.1. \end{cases} \tag{3.3.1}$$

3.3.4 Morphology Classification

To calibrate a quantitative morphology cut for application to the ECO galaxies, we use by-eye morphological classifications from the RESOLVE survey, the A-semester sample of which is largely a subset of the ECO catalog (see Appendix A and Kannappan et al., in prep. for full details). RESOLVE galaxies that were given uncertain classifications by the classifiers are omitted from consideration. Since this comparison sample has just over 1000 galaxies, considerably fewer than the full ECO sample, and possesses few very bright galaxies, we also add to our morphology

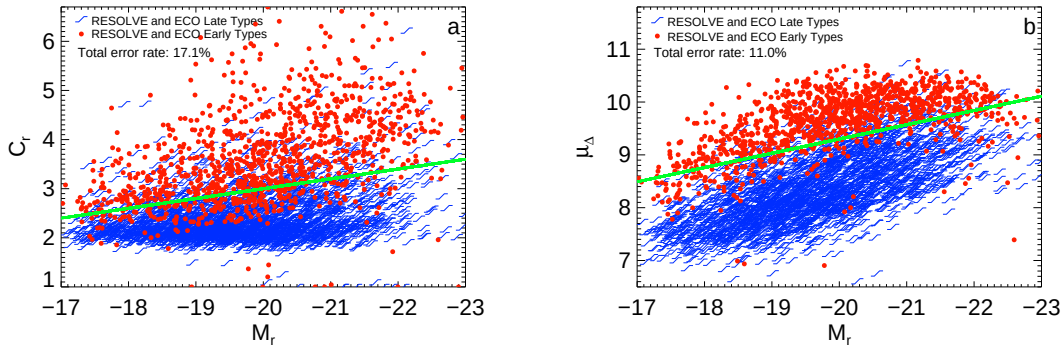

Figure 3.6 Quantitative morphology metrics applied to by-eye classified galaxies in the RESOLVE and ECO samples (see §3.3.4 for details). Panel *a* shows a cut in C_r vs. M_r applied to ECO and RESOLVE galaxies classified by eye as early and late types. The solid green line shows an optimized morphology discriminant in this parameter space ($C_r = -0.2 \times M_r - 1$), which performs poorly in duplicating the by-eye morphological classes. Panel *b* shows the distribution of these same galaxies in the μ_Δ vs. M_r parameter space. The solid green line shows our optimized morphology discriminant in this parameter space ($\mu_\Delta = -0.27 \times M_r + 3.9$), which gives improved classification error rates over the concentration index approach.

calibration sample those galaxies in ECO that have been previously classified by eye in the catalog of Nair & Abraham (2010) or by the Galaxy Zoo Project (Lintott et al. 2011). We use only the "clean and debiased" Galaxy Zoo classifications referenced by Lintott et al. (2011), which require 80% of classifiers to agree on the chosen morphological type and debiasing with respect to the effects of luminosity, size, and distance on the classifications (see §3.1 of Lintott et al. 2011).

Based on comparisons to this by-eye classified sample, an optimal quantitative morphology cut was derived for application to ECO. Traditional quantitative morphology discriminants, such as the concentration index $C_r = R_{90\%}/R_{50\%}$ defined using SDSS catalog photometry (e.g., Strateva et al. 2001; Shimasaku et al. 2001), yield unfortunately high error rates in the ECO sample (see Fig. 3.6a)[2]. We instead employ the μ_Δ metric recently developed by K13, which combines the surface mass density within $R_{90\%}$ and a multiple of 1.7 times the difference between the surface mass densities within $R_{50\%}$ and within the $R_{50\%} - R_{90\%}$ annulus. We optimize this metric for use as an early/late type discriminant in ECO by considering it as a function of M_r and choosing a linear cut in this parameter space that yields the minimum misclassification rate (see Fig. 3.6b).

To reduce the misclassification rate resulting from implementing a quantitative morphology cut, we make further use of the Galaxy Zoo clean and debiased morphology classifications. Where such classifications exist for ECO galaxies, we use the Galaxy Zoo early/late type classification rather than

[2]Note that we explicitly avoid the inclusion of color as a parameter used for morphology discrimination due to the bias it would introduce against blue early and red late types.

that inferred from the optimized quantitative morphology cut described above. This substitution results in a naive apparent misclassification rate of ∼3.6% for late types and ∼13.9% for early types in the morphology calibration sample.

We can better estimate the misclassification errors that would result from applying this quantitative calibration to an independent sample with a bootstrap resampling approach applied to the calibration sample, using the ".632" error rate estimator as described by Efron (1983). The bootstrap sampling procedure is repeated for 1000 iterations. For each iteration, we randomly sample N objects from the morphology calibration sample with replacement, where N is equal to the total number of objects in the calibration sample (the ".632" nomenclature refers to the fact that ∼63.2% of the objects will end up in each bootstrap sample on average because objects can be selected twice). We then use the bootstrap sample to determine an optimum classification rule and evaluate the misclassification rate using this rule when applied to those members of the morphology calibration sample that were outside the bootstrap sample. As for the ECO sample, we include replacement of quantitatively inferred classifications with those from Galaxy Zoo to fairly assess the error rate during each iteration. We calculate our final error estimates as:

$$E_{final} = 0.632E_{bavg} + .368E_{app}, \tag{3.3.2}$$

where E_{bavg} represents the average of the estimated error rates over the 1000 resampling iterations and E_{app} represents the naive apparent error rate estimate in the calibration sample. The final error estimates are similar to the aforementioned naive apparent error rates, with estimated ∼3.7% error rate for late types or ∼13.8% for early types. We also calculate these error estimates in multiple individual bins of group halo mass and galaxy stellar mass as the error rate is not necessarily constant for different subclasses of galaxies in the sample. Our early-type misclassification rates tend to decrease with increasing galaxy stellar mass, from ∼17% at our lowest stellar masses to ∼11% at our highest stellar masses, and to increase with increasing group halo mass, from ∼10% at our lowest halo masses to ∼16% at our highest halo masses.

3.3.5 Identification of UV Disks

For the ECO galaxies covered by *GALEX* NUV imaging, we apply an automated procedure for quantitatively identifying Ultraviolet-Bright (UV-B) disks according to the definition of Moffett et al. (2012). For each galaxy, we apply the center position, position angle, and ellipticity of the

SDSS optical ellipse fit to a set of fixed parameter IRAF ellipse fits on the NUV imaging, which are allowed to proceed outwards radially until no significant UV flux is detected. We apply additional SExtractor-derived masking of the UV images beyond that determined for the original SDSS optical photometry procedure, necessary due to the low resolution of the *GALEX* data and the occasional appearance of new contaminating sources not present in the optical data. As described by Moffett et al. (2012), the quantitative UV-B disk classification we employ requires satisfaction of an NUV$-K$ color condition, which is included to ensure young stellar population ages and select stellar populations with a minimum $\sim$10% young component by mass. We calculate NUV$-K$ colors between the optical g-band 50% light radius and the end of the NUV profile and require NUV$-K$ < 4.5 for classification as a UV-B disk[3].

Validating this fully automated identification approach against the methods of Moffett et al. (2012), which employed a more detailed, galaxy-by-galaxy elliptical isophote fitting procedure, our new algorithm identifies up to $\sim$25% more UV-B disks in an E/S0 sample. Reasons for the difference between the more and less automated approaches include occasional position angle misalignments between the galaxy regions where optical and UV emission dominate and imperfect automated masking of UV sources, which is in some cases less aggressive than the masking employed by Moffett et al. (2012).

3.3.6 Environment Metrics

For the catalog samples under consideration, we compute two different metrics of galaxy environment. We primarily focus on environmental trends using group halo mass, but we also compare to results obtained with a smoothed galaxy density field in §3.4.

Group Finding

We identify groups of galaxies using the friends-of-friends algorithm of Berlind et al. (2006). We infer halo masses based on the observed total r-band luminosity of galaxies in each group following an abundance matching procedure, as described in Blanton & Berlind (2007). Specifically, we assume a monotonic relation between the observed group luminosity and its halo mass, which we determine by matching the abundance of observed groups of a given luminosity to that of dark matter halos of a given mass, as derived from a standard concordance cosmology halo mass function. From

[3]Note that in some cases galaxy outer disks are not well detected in our 2MASS images. In such cases, we calculate upper limit K-band magnitudes in the outer-disk regions and use these magnitudes for determining the NUV$-K$ color.

consideration of the mock galaxy catalogs described below, we find that typical group halo mass errors are of order 0.15 dex, although much larger errors can sometimes occur when groups are improperly fragmented or improperly linked together.

The group-finding algorithm we employ automatically determines an appropriate "linking length" for grouping individual objects together, equal to 0.14 times, in the on-sky direction, and 0.75 times, in the line-of-sight direction, the mean separation between galaxies in the input sample (with $D = cz/H_0$ distances and $H_0 = 100h\ km\ s^{-1}\ Mpc^{-1}$ used for this calculation). For a sample region as small as RESOLVE-B, this mean spacing determination is far more sensitive to cosmic variance than for a large region as in the ECO sample. To compensate, when we apply the group-finding algorithm to RESOLVE-B we fix the linking lengths to those determined from a version of the ECO catalog limited to $M_r < -17$, the magnitude limit of RESOLVE-B. We also use the luminosity to halo mass conversion determined from this version of the ECO group catalog, since this conversion is similarly sensitive to cosmic variance. Through testing with an "ECO-analog" version of RESOLVE-B (matched to ECO's shallower depth and lower completeness; see §3.3.8), we find that the difference in completeness between RESOLVE-B and ECO does not significantly bias the group halo masses we estimate, with scatter between the group halo masses inferred from the two versions of RESOLVE-B only reaching ∼0.2 dex at $M_{halo} \gtrsim 10^{13} M_{\odot}$. The primary effect of extra completeness on group identifications is that additional $N = 1$ halos, typically containing faint galaxies near the magnitude limit, are found. Fig. 3.4 reveals that ECO is not complete for group halos with masses less than $M_{halo} \sim 10^{11.1} M_{\odot}$, so we refrain from including halos below this mass limit in our analysis.

Smoothed Galaxy Density Field

We calculate a smoothed galaxy density field with an IDL procedure based on the approach of Grogin & Geller (1999). This procedure takes in individual galaxy redshift-space positions, assuming line of sight $D = cz/H_0$ for consistency with other methods applied here, and creates a continuous number density field from this spatial point distribution by smoothing each galaxy with a unit-normalized Gaussian kernel and summing the resulting galaxy space and velocity distributions. Since the samples considered in this work are volume- and not flux-limited, no luminosity function weighting factors have been applied in the density field calculation (cf. Grogin & Geller 1999).

In using this smoothed galaxy density field procedure, we use a smoothing kernel width of ∼1.43 Mpc (1 Mpc/h with $h = 0.7$), a scale that is similar to a typical halo virial radius at z ∼0. In

all subsequent density analysis, we limit ourselves to consideration of galaxies that lie >2 smoothing lengths from catalog edges and report density values normalized by the median density of the smoothed field.

In order for densities smoothed on this small scale to be physically meaningful, we also implement a procedure to statistically collapse "fingers of God" in ECO, as these cause measured line-of-sight velocities in large groups/clusters to imperfectly reflect physical distances. Similar methods for statistically correcting redshift-space distortions have been applied by other authors (e.g., Tegmark et al. 2004). The algorithm we apply was developed and calibrated on mock galaxy catalogs derived from an N-body simulation of a ΛCDM cosmological model, with Ω_m =0.25, Ω_Λ =0.75, Ω_b =0.04, h=0.7, n_s=1.0, and σ_8 =0.8. Initial conditions were set using second order Lagrangian Perturbation Theory (Scoccimarro 1998) at a starting redshift of z =99 and the particle distribution was evolved using the code GADGET-2 (Springel 2005). The simulation contains 1050^3 dark matter particles in a box of size 180 Mpc/h, sufficient to encompass multiple ECO catalog volumes. The resulting particle mass is 3.5×10^8 $M_\odot$/h and the gravitational force softening is 7 kpc/h. At this resolution, the lowest mass halos in the ECO catalog sample typically contain 160 particles. We identify halos in the dark matter particle distribution using a friends-of-friends algorithm with a linking length equal to 0.2 times the mean interparticle separation. We then populate these halos with galaxies using a halo occupation distribution (Berlind & Weinberg 2002) designed to produce a galaxy population with similar space density and clustering properties as ECO galaxies. Central galaxies are given positions and velocities of halo centers of mass, and satellite galaxies are given positions and velocities of randomly selected dark matter halo particles. This procedure produces a "real-space" mock galaxy catalog. The real-space catalog is subsequently distorted into a "redshift-space" mock galaxy catalog by assuming the line of sight direction to extend radially outward from the center of the box and incorporating galaxy peculiar velocity components along the radial direction into galaxy redshifts.

Comparisons between real-space and redshift-space versions of the mock galaxy catalogs allow us to determine the distribution of 3D, real space radius offsets from the group center positions as a function of the group virial radii. The overall real-space group-centric R/R_{vir} density profile determined from the mock catalogs is approximated with a gamma probability density function fit and used as an input when we apply the collapse algorithm on observed catalogs. The fit relation has the following form:

$$f(x,a,b) = \frac{x^{a-1} \times e^{-bx} \times b^a}{\Gamma(a)}, \tag{3.3.3}$$

where a=1.6 and b=5.

We begin the finger-of-God collapse process on the observed galaxy catalogs with group identifications determined as described in §3.3.6. For each galaxy in an $N > 1$ group, we first assign a random real-space displacement from the center of the group according to our fit distribution of mock-catalog-determined R/R_{vir} values, taking into account the group's estimated R_{vir}. Each assigned 3D radius is then checked for consistency with the galaxy's observed projected distance from the group center, that is, a galaxy's assigned 3D distance from the group center is required to be greater than its observed projected distance from the center. If this is not the case on first assignment, a different random 3D radius value is chosen until the condition is met. This procedure does not significantly bias the assigned R/R_{vir} distribution. Next, the appropriate redshift direction displacement from the group center is determined for each galaxy, using the observed spatial coordinates and the assigned 3D radius. The sign of the redshift displacement for each galaxy relative to the group center is determined randomly.

Validation of the final collapse procedure on the mock catalogs yields reasonable agreement between the corrected and original simulated, real-space group velocity dispersions (see Fig. 3.7), although we tend not to reach corrected group velocity dispersions as small as the original dispersions seen in real-space mock catalog groups). This bias appears to be due largely to imperfect recovery of halo R_{vir} by our group finding method; overestimation of R_{vir} has the effect that our collapse algorithm places galaxies at larger 3D group-centric radii (and larger velocities) than observed in the real-space groups. The effect of the collapse process on the distribution of galaxies in the ECO catalog is shown in Fig. 3.8. The application of this collapse process yields greater confidence in our density field results, which generally agree with group-finding results that are less sensitive to such finger-of-God effects.

3.3.7 Atomic Gas Mass Estimates

For galaxies in the ECO+A subsample, we cross-match to published ALFALFA $\alpha.40$ (Haynes et al. 2011) HI sources within 1.5 times the beam radius ($3'$) and use the reported line flux densities to convert to M_{HI} via the standard formula ($M_{HI} = 2.36 \times 10^5 \times D^2 \times F_{HI}\ M_\odot$; Haynes & Giovanelli 1984). We then multiply our masses by 1.4 to correct for the presence of He. In the absence of HI detections, we estimate upper limits according to the procedure described by K13, which uses the typical $\alpha.40$ rms noise as a function of declination integrated over a velocity interval estimated for each source according to the average relation between internal velocity and r-band

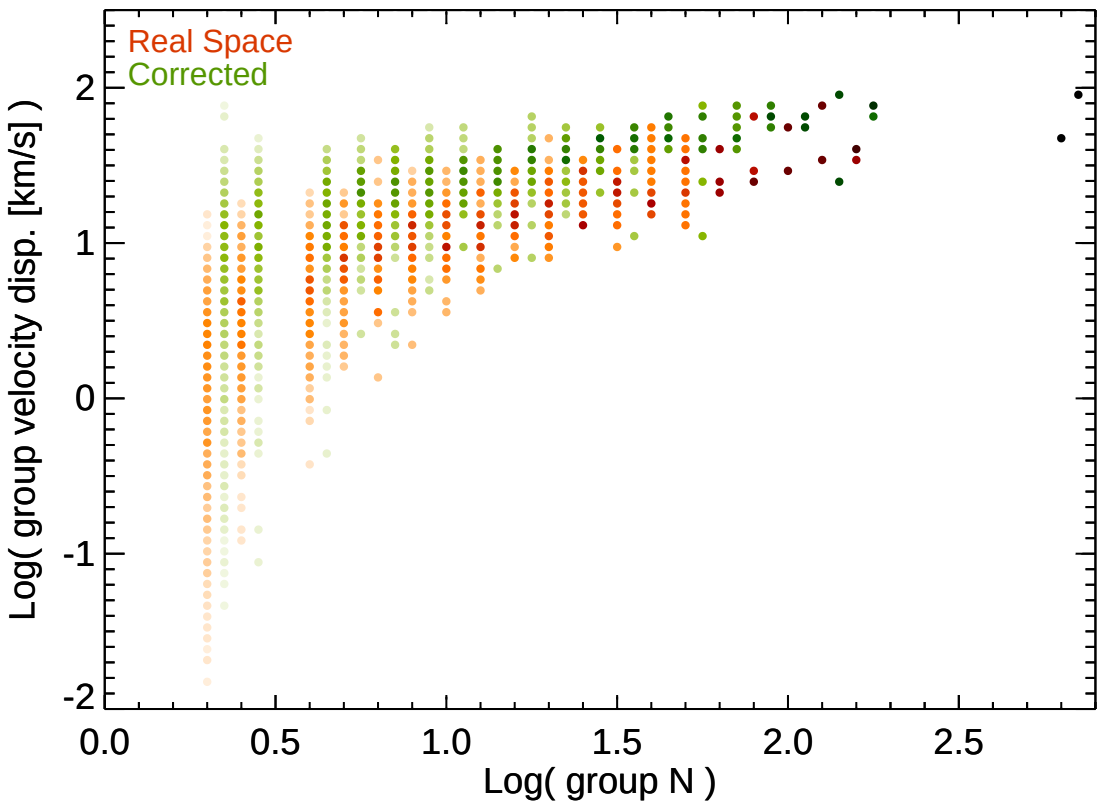

Figure 3.7 Illustration of the recovery of real-space mock galaxy catalog group velocity dispersions after running group finding on a redshift-distorted version of the catalog and applying our finger-of-God collapse procedure on the resulting group catalog. Plotted are the distributions of real-space group velocity dispersion (red/orange scale) and corrected group velocity dispersion (green scale) versus real group N, where color coding of points represents the histogram density normalized to sum to one within each bin of group N (darkest colors imply the highest density). Red and green points are plotted offset by half the group N bin size for clarity. Note that we typically do not collapse groups to velocity dispersion levels as small as those seen in real-space groups.

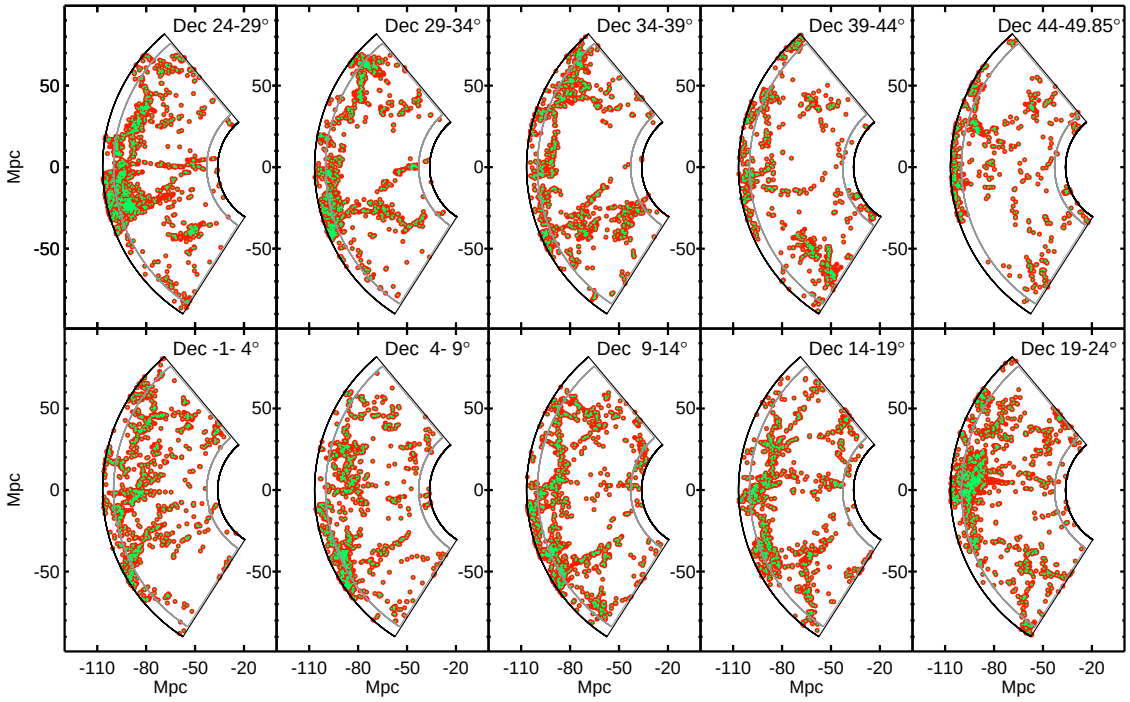

Figure 3.8 Illustration of the finger-of-God collapse procedure applied to the ECO catalog. Red points show the original inferred spatial distribution of galaxies, and smaller green points show the distribution after the finger-of-God collapse procedure has been applied.

magnitude ($\log V = -0.29 - 0.123\ M_r$, calibrated by K13). We check for possible confusion using a large combined redshift catalog containing ECO (see §3.2.1) and flag a source as confused if another galaxy is found within a $3'$ radius and if the HI profiles would overlap in velocity space assuming minimum 50 km/s redshift uncertainties and typical line widths of ∼100 km/s (the weighted average of the ALFALFA-derived velocity width function; Papastergis et al. 2011).

Where ECO galaxies lack ALFALFA $\alpha.40$ detections or have confused HI measurements, we use the "photometric gas fraction" technique (Kannappan 2004) to assign HI mass estimates based on the observed tight correspondence between HI gas to stellar mass ratio and $u - J$ color. We employ the photometric gas fraction calibration and procedure described by K13, in which gas masses are assigned to galaxies with $(u - J)^{model} < 3.7$ according to the relation:

$$\log\left(M_{HI}/M_*\right) = 2.7 - 0.98\ (u - J)^{model} \tag{3.3.4}$$

with random 0.34 dex scatter motivated by the observed relation. If the gas mass estimated with this relation for a given galaxy would exceed its calculated upper limit, the upper limit is adopted instead. For galaxies with colors redder than $(u - J)^{model} = 3.7$, that is, where the linear color-gas-to-stellar mass ratio relation breaks down for quenched galaxies, the procedure assigns random values in the logarithmic range $M_{HI}/M_* = 0.001 - 0.5$, again constrained to lie below the estimated upper limit for each galaxy.

We make one significant modification to the K13 photometric gas fraction procedure, which is motivated by the tendency for the bluest and most gas-rich galaxies to lie above the aforementioned gas-to-stellar mass ratio versus color relation (see K13 Fig. 8a). To better reflect the typical gas-to-stellar mass ratios observed for galaxies with $(u - J)^{model} < 3$, we multiply the gas mass estimates that would result from the K13 estimator by an additional factor of 1.5 in this regime, with resulting estimates still constrained to lie below upper limits where available. While our gas mass estimates are improved by the inclusion of this factor, we note that its inclusion does not qualitatively affect the results we report, which remain similar even if the extra multiplicative factor is omitted from estimated gas masses. In particular, we largely focus our analysis of gas content on the incidence of gas-dominated ($M_{HI}/M_* > 1$) galaxies in ECO, and so for much of our analysis, the exact gas mass estimated for a given galaxy is less important than whether or not it falls into a broad gas-to-stellar mass ratio category.

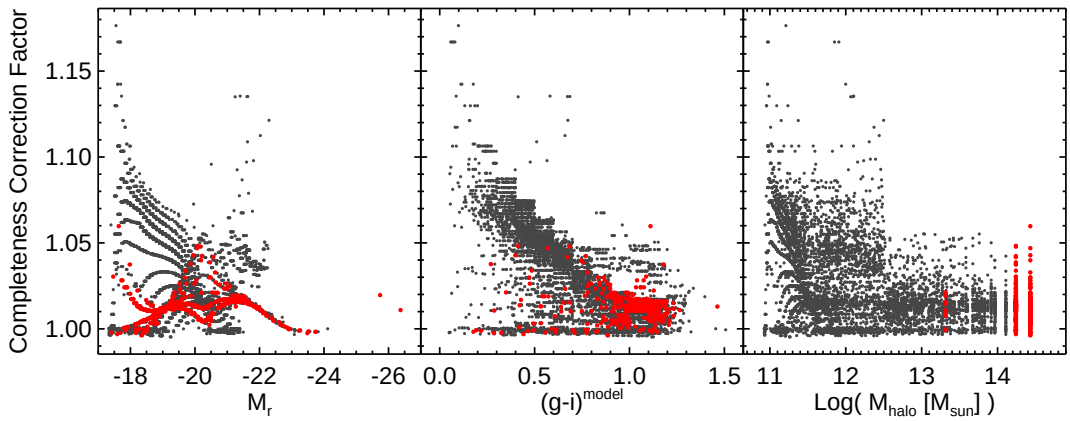

Figure 3.9 Multiplicative completeness correction factors derived for each individual ECO galaxy (points) as a function of r-band absolute magnitude, model $g-i$ color, and group halo mass. Galaxies indicated by red points require further multiplicative membership correction factors on top of the factors shown, due to the loss of galaxies with extreme line-of-sight velocities outside the ECO definition. The majority of galaxies indicated by red points lie in the Coma Cluster, where the additional multiplicative correction factor reaches its maximum value of ~ 1.77.

3.3.8 Completeness Corrections

Since the RESOLVE-B sample has much higher completeness than the ECO sample (see §3.2.2), we use the former to calibrate and correct for the effects of redshift incompleteness in the latter. To do so, we first construct a version of the RESOLVE-B sample analogous to the ECO catalog, that is, including only galaxies that would be found in the catalogs that make up ECO and excluding the extra SDSS Stripe 82 redshift coverage beyond the original redshift survey. For this "ECO-analog" version of RESOLVE-B, we also make photometric measurements using the same methods as for ECO proper, using only single-depth SDSS images analogous to those available for ECO and not the deeper co-added imaging available in the Stripe 82 region. We then compare number counts for the complete RESOLVE-B sample with those for the ECO-analog version in the parameter space of $(g-i)^{model}$ color vs. M_r, thereby determining the factors necessary to correct the ECO-analog numbers to match the complete RESOLVE-B numbers as a function of M_r and $(g-i)^{model}$. We prefer to use $(g-i)^{model}$ color because it is measured with higher S/N than any color constructed with SDSS u-band magnitudes, however we find that the derived completeness correction results are similar for other choices of galaxy color.

We divide both samples into cells in a $(g-i)^{model}$ vs. M_r grid, determined with a simple adaptive approach, which begins with subdividing each axis into four large cells. If more than five galaxies are present in a given cell, the cell is subdivided in half iteratively until no further subdivisions are

allowed by the five galaxies per bin condition. We interpolate each irregularly gridded dataset into a smoothly varying number density field, and divide the ECO-analog and RESOLVE-B sample fields to derive a final completeness correction field.

Our completeness correction method results in multiplicative correction factors that vary as a function of absolute magnitude, color, and environment as illustrated in Fig. 3.9. The median correction factor applied to a galaxy in our sample is ∼2%, but correction factors can reach up to nearly ∼18%. As this approach reveals residual differences in the derived completeness corrections as a function of galaxy environment, we elect to compute corrections separately for two different group halo mass regimes: above and below $M_{halo} = 10^{12.5} M_{\odot}$. The median correction factor is ∼3.5% for galaxies in low-mass halos and ∼1% for galaxies in high-mass halos.

In addition to the aforementioned environment-dependent incompleteness, we note that the presence of cluster fingers of God in the ECO sample can cause further incompleteness through the loss of members with extreme line-of-sight velocities, putting them outside our sample limits even though we include a large buffer region in our analysis to mitigate such losses. The presence of the Coma Cluster, in particular, leads to incompleteness for the highest group halo mass in the ECO sample (see upper leftmost panel in Fig. 3.2), which cannot be appropriately corrected through consideration of the RESOLVE-B comparison sample as this incompleteness is caused by ECO boundaries and not incomplete redshift data. To quantify correction factors for this boundary effect, we construct a comparison catalog including the same data sources as ECO but extending beyond the ECO redshift limits in both directions (1500 km/s to 12000 km/s), encompassing all apparent fingers of God extending outside of the ECO region. As reprocessed photometry is not available for this entire comparison catalog, we rely on SDSS catalog magnitudes and perform group finding on both ECO and the comparison catalog with catalog r-band magnitudes as input. We then match the ECO catalog groups to groups in the comparison catalog, where a given comparison catalog group center must lie within the ECO group R_{vir} on sky and within three times the ECO group velocity dispersion in the redshift direction. For any galaxy in a group that has been affected by proximity to the ECO volume edges, we calculate and apply an additional completeness correction factor based on the ratio of the number of galaxies in comparison catalog groups to the number of galaxies in ECO catalog groups, derived considering only galaxies with catalog magnitudes $M_r < -18.4$ (corresponding to the nominal SDSS r-band completeness limit at $cz = 12000$ km/s). The calculated boundary completeness correction factors range up to a maximum of ~ 1.77 for Coma galaxies in particular. We multiply the completeness correction factors illustrated in Fig. 3.9 by the boundary

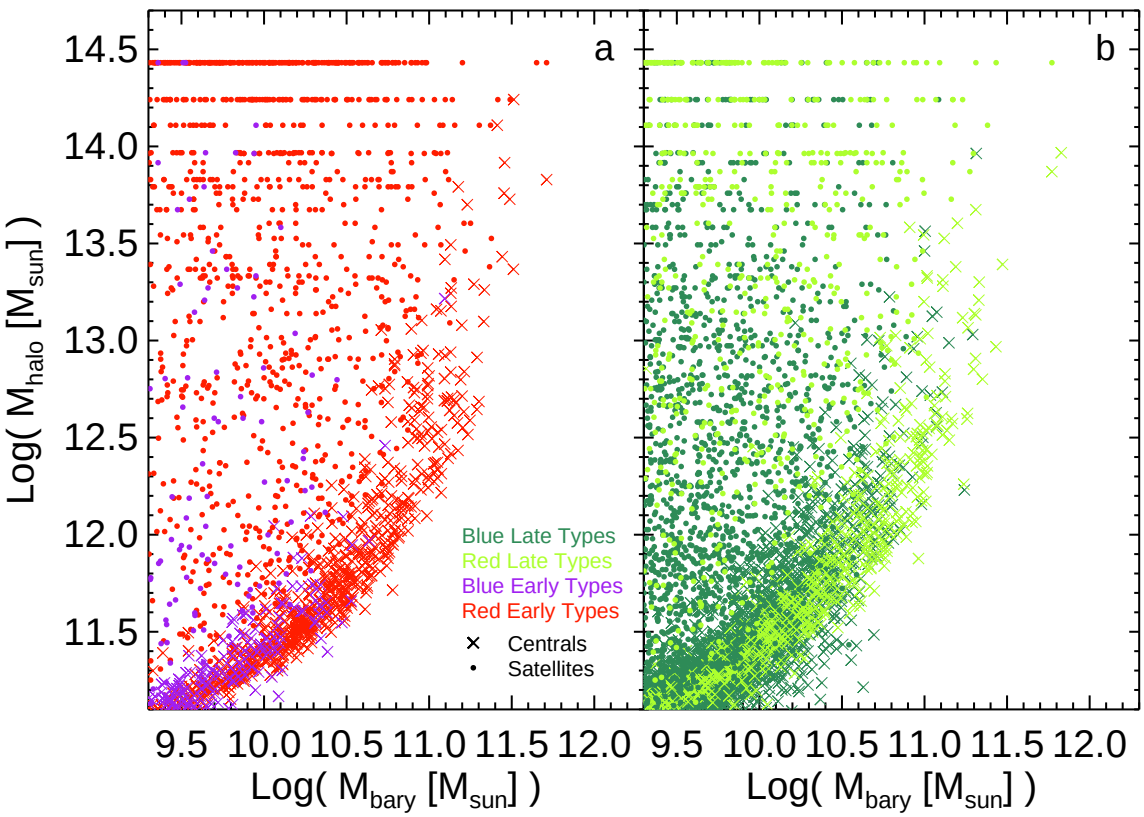

Figure 3.10 Illustration of ECO catalog galaxy distributions in the group halo mass and galaxy baryonic mass space, where early types of red/blue and central/satellite classes are shown on panel *a*, and late types of red/blue and central/satellite classes are shown on panel *b*. No catalog membership completeness corrections have been applied in this figure.

completeness correction factors to obtain the final ECO sample membership corrections.

As the loss of galaxies beyond ECO boundaries affects sample membership, this loss can also affect our derived group halo mass estimates. To correct for this effect, we use the same logic described above and apply a correction factor to each affected group halo mass based on the ratio of the total group luminosity derived in the comparison catalog to the total group luminosity derived in the ECO catalog. Applied group halo mass corrections range up to a maximum 0.06 dex increase for the Coma Cluster.

3.4 Results

In this section, we explore trends in galaxy properties related to galaxy mass and environment, using group halo mass as our primary indicator of environmental richness. The distribution of various classes of ECO catalog galaxies in group halo mass versus galaxy baryonic, stellar plus atomic gas,

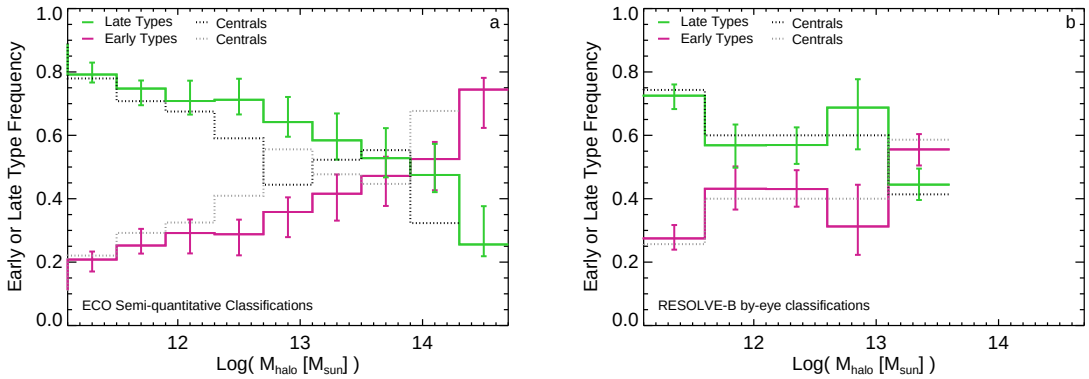

Figure 3.11 Illustration of the traditional morphology-environment relation in the ECO and RESOLVE-B samples. Early and late type frequencies as a function of group halo mass in (a) ECO and (b) RESOLVE-B, with early and late type frequencies crossing over at $M_{halo} \sim 10^{13.5} M_{\odot}$ in the ECO sample. Greyscale dotted lines indicate the frequencies for central galaxies alone, which become poorly determined at high halo masses due to the small number of high halo mass groups (and thus centrals) present in the sample. In panel a, all frequencies are plotted at their "expected" value given the calibrated uncertainties in our semi-quantitative morphology classification method, described in §3.3.4. The error bars in this panel are plotted as a combination of the calculated misclassification errors in each halo mass regime and the (binomial) counting statistics in each bin, while those in panel b reflect only the relevant counting statistics (assuming zero misclassification). Note that the early/late type frequencies for the two samples do not strictly agree in all bins, particularly near $M_{halo} \sim 10^{12} M_{\odot}$. Applying the quantitative classification approach to RESOLVE-B results in frequencies that more closely agree with the frequencies in ECO, although slight residual differences remain, perhaps resulting from group-to-group variations in typical properties.

mass parameter space can be seen in Fig. 3.10. Results derived from the density field are qualitatively similar to results derived from group halo masses, except as discussed in this section.

3.4.1 Traditional Morphology-Environment Relation - P(M|E)

As seen in Fig. 3.11a for the traditional formulation of the morphology-environment relation (frequency of a particular morphology as a function of environmental richness), the ECO sample displays the expected increase in early-type and decrease in late-type frequencies as a function of increasing environmental richness, here represented by increasing group halo mass. Near group halo mass $\sim 10^{13.5} M_{\odot}$, we observe a crossover point where early and late type frequencies become approximately equal. The frequencies in the more complete RESOLVE-B sample, where morphological classifications are entirely based on by-eye judgments, do not strictly agree with the frequencies in ECO, particularly around $M_{halo} \sim 10^{12} M_{\odot}$ (see Fig. 3.11b). If we apply quantitative classification methods to RESOLVE-B, we find frequencies that more closely but not completely agree with the frequencies in ECO. Variations in morphological mixtures between groups at fixed halo mass could

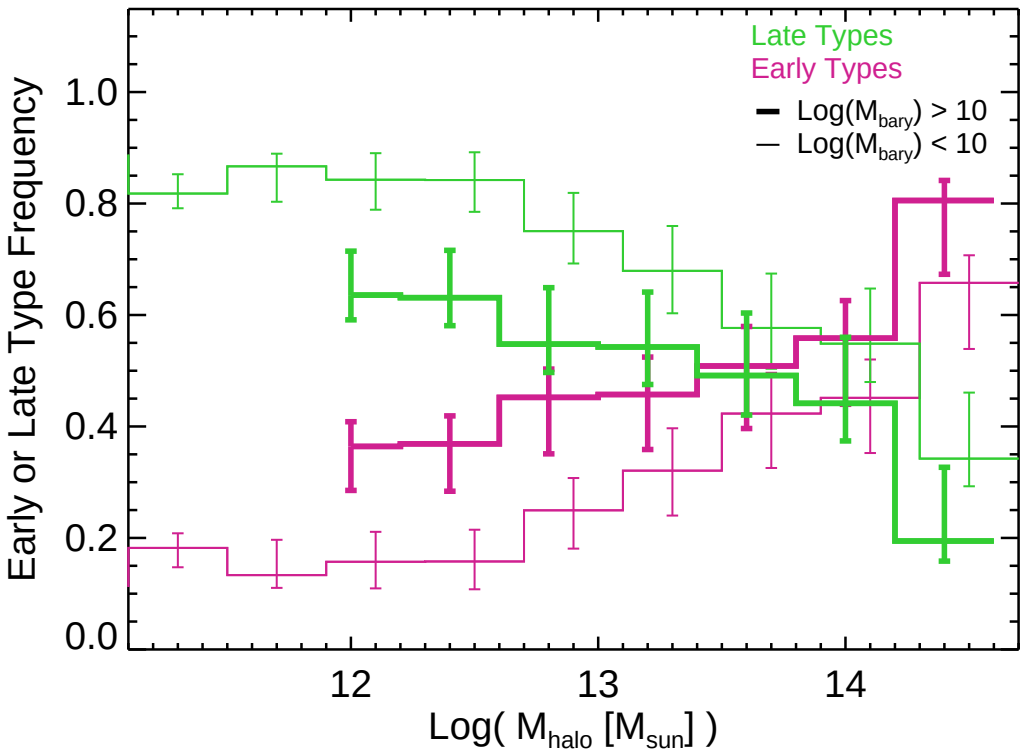

Figure 3.12 Illustration of morphology-environment relations in the ECO sample for separate high-mass ($M_{bary} > 10^{10} M_{\odot}$) and low-mass ($M_{bary} < 10^{10} M_{\odot}$) galaxy subsamples, indicated by thick and thin lines, respectively. Since few high mass galaxies inhabit halos below $\sim 10^{12} M_{\odot}$, we do not plot the frequencies for high mass galaxies below this point. While the trends are qualitatively similar over most of the group halo mass range, the relations have different amplitudes for the low and high galaxy mass samples.

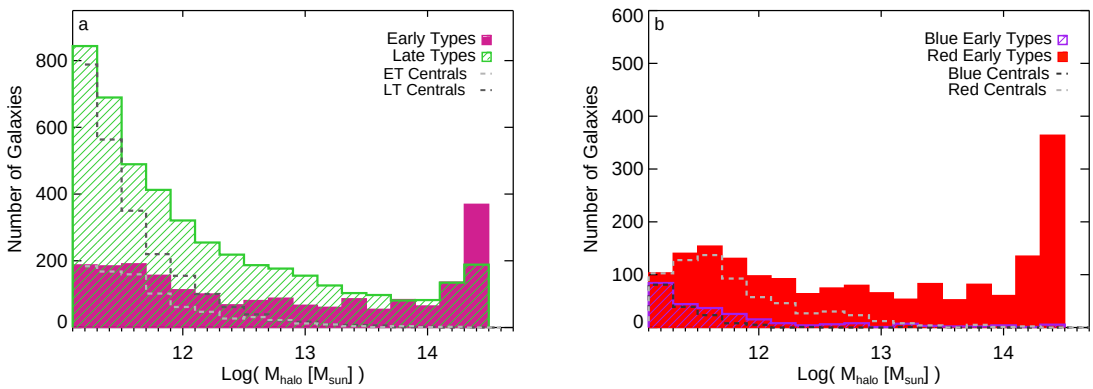

Figure 3.13 Halo mass distribution for early and late type galaxies in the ECO sample, with corresponding grey dashed lines indicating the distribution for group central galaxies of each type. Panel *a* shows all early and all late types together, and panel *b* breaks down the early types further by red and blue sequence membership. Approximately 40% of ECO early type galaxies occupy $M_{halo} < 10^{12} M_{\odot}$ environments, approximately 25% of which are blue early types.

also plausibly contribute to differing morphological mixes in these two samples. If we divide central and satellite galaxies, we find that central and satellite morphology-environment trends are similar to each other in both samples, where the satellite galaxy trend (not shown) closely follows the combined trend in Fig. 3.11a/b. If we examine the traditional morphology-environment relation for low and high baryonic mass (divided at $M_{bary} = 10^{10} M_{\odot}$) galaxies separately, we qualitatively recover the expected early-/late-type frequency trends as a function of halo mass, with the low and high baryonic mass relations offset overall and relatively flat except at the highest halo masses we sample (see Fig. 3.12).

3.4.2 Alternative Morphology-Environment Relation - P(E|M)

Considering an alternative formulation of the morphology-environment relation, the probability for a galaxy with a given morphology to inhabit a particular environment, we observe changes in early type population demographics at two low halo mass scales of potential interest. In ECO, we find that the majority of late-type galaxies occupy $M_{halo} < 10^{12} M_{\odot}$ environments (see Fig. 3.13a), which is not a surprising result given the form of the traditional morphology-environment relation. However, it is also apparent from this figure that ∼40% of early-type galaxies occupy $M_{halo} < 10^{12} M_{\odot}$ environments as well.

As seen in Fig. 3.13b, many early types in the lowest density environments are *blue-sequence* early types. These blue early types start to become more common below $M_{halo} \sim 10^{12} M_{\odot}$ and become comparable in numbers to red early types only below $M_{halo} \sim 10^{11.3} M_{\odot}$. Blue early types

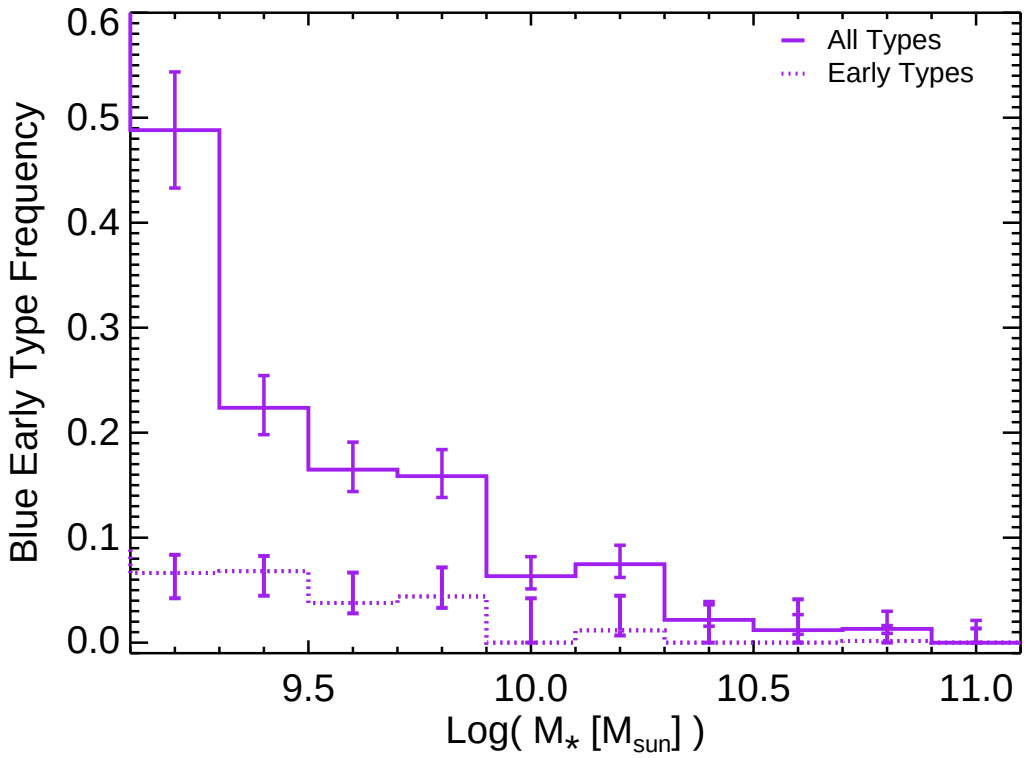

Figure 3.14 Variation in blue early type galaxy frequency as a function of stellar mass in the ECO sample. The solid line indicates the frequency of blue early types as a fraction of early types only, while the dotted line indicates their frequency as a fraction of all galaxy types. Frequencies are plotted at their expected values given the calibrated uncertainties in our semi-quantitative morphology classification method, described in §3.3.4. Error bars shown are a combination of the estimated misclassification errors and the (binomial) counting statistics in each bin.

with baryonic masses large enough to meet our mass limit are primarily central galaxies in this low group halo mass regime and primarily satellite galaxies in richer environments (see Fig. 3.10). However, since satellite blue early types with masses below our survey limit could also populate the low mass halos, we cannot yet quantify the balance between blue early type centrals and satellites in these environments. Fig. 3.10 shows that blue early-type galaxies appear to have similar environment distributions to blue late-type galaxies overall, but blue early types display a much more pronounced preference for the lowest group halo mass environments. As calculated with the Kolmogorov-Smirnov (K-S) test, the group halo mass distributions of blue early and blue late types in Fig. 3.10 are incompatible with having the same parent distribution ($P_{same} \sim 10^{-4}$).

We find that blue-sequence early-type galaxies are not only most common in low halo mass environments but at low stellar masses as well, both of which are regimes where extreme gas richness

is typical. As was previously found by KGB, we observe that the blue early-type galaxies in ECO become more common with *decreasing* stellar mass (see Fig. 3.14). These galaxies only emerge in ECO with measurable frequency around the galaxy bimodality mass ($M_b \sim 10^{10.5} M_\odot$) and increase in frequency significantly below $M_* \sim 10^{10} M_\odot$. This behavior is similar to that observed in KGB, where the blue early-type population increases sharply below $M_* \sim 10^{9.7} M_\odot$, the "gas-richness threshold" mass. Our observed frequency transition is somewhat less sharp than that observed by KGB, but it is plausible that any sharp transitions could be washed out by the error rates inherent in our semi-quantitative classification method. Our absolute frequencies are similar to those reported by KGB, although not in strict agreement within our error bars. If similarly large error bars on the KGB frequencies are assumed, then the two trends would agree overall. Thomas et al. (2010) have also observed an increasing frequency of "rejuvenated" early-type galaxies with decreasing galaxy mass (and environmental density), reaching a maximum of ∼45% of the early-types, which is similar to our observed maximum frequency. This observed low-mass preference implies that mass-dependent mechanisms are closely tied to the rise of the blue-sequence early-type population. We note that the typically low stellar mass nature of blue early-type galaxies appears linked to the typically low group halo mass environments they inhabit. At $M_* \sim 10^{10} M_\odot$, the typical baryonic mass for a galaxy is $\sim 10^{10.1} M_\odot$, which from Fig. 3.10 corresponds to a typical halo mass of $\sim 10^{11.5} M_\odot$ for centrals.

The P(E|M) formulation of the morphology-environment relation clearly reveals different preferred environment regimes for galaxies broken down by mass as well as morphological type and color. Comparing the halo mass dependences in Fig. 3.15a reveals a possible "inverse morphology-environment relation" (as suggested by KGB), wherein blue early type galaxies below $M_* \sim 10^{10} M_\odot$ inhabit environments of similar or lower richness than the environments occupied by blue late type galaxies at the same stellar mass. Fig. 3.15a seems to show that the typical environment richness of blue early type centrals below $M_* \sim 10^{10} M_\odot$ is lower than that of blue late type centrals at fixed stellar mass. However, the typical environments of blue early type and blue late type satellites are not clearly distinct given the large error bars on the typical values for blue early type satellites. Moreover, if we correct for the contribution of atomic gas mass, which can be a significant mass component in many low stellar mass galaxies, and instead compare these populations at constant baryonic mass, we find that $M_{bary} \lesssim 10^{10} M_\odot$ blue early and blue late types occupy typically similar environments, for both centrals and satellites (Fig. 3.16). The lack of a morphology-environment relationship among central galaxies also holds if we consider all early types and all late types together. Showing a similar lack of morphology-environment trend, the traditional morphology-environment

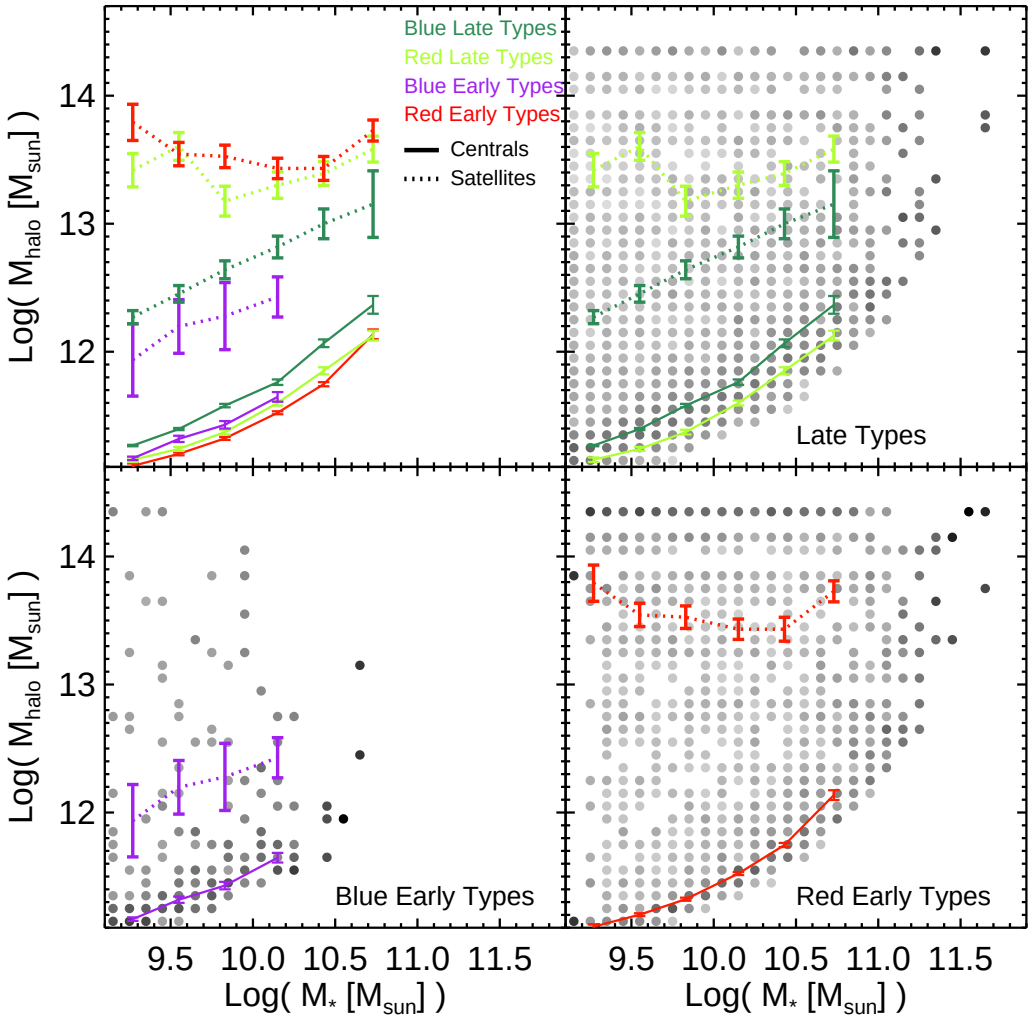

Figure 3.15 Characteristic distribution of halo mass as a function of stellar mass for different galaxy types. Solid lines indicate the running median group halo masses for centrals of each galaxy type, while dashed lines indicate the medians for satellites of each galaxy type. Error bars for each median point are estimated from the dispersion in properties in each bin. The background greyscale levels indicate the probability of inhabiting a particular halo mass at a given stellar mass, as the histogram densities used to set the greyscale have been normalized to one in each stellar mass bin (darkest points imply the highest probabilities).

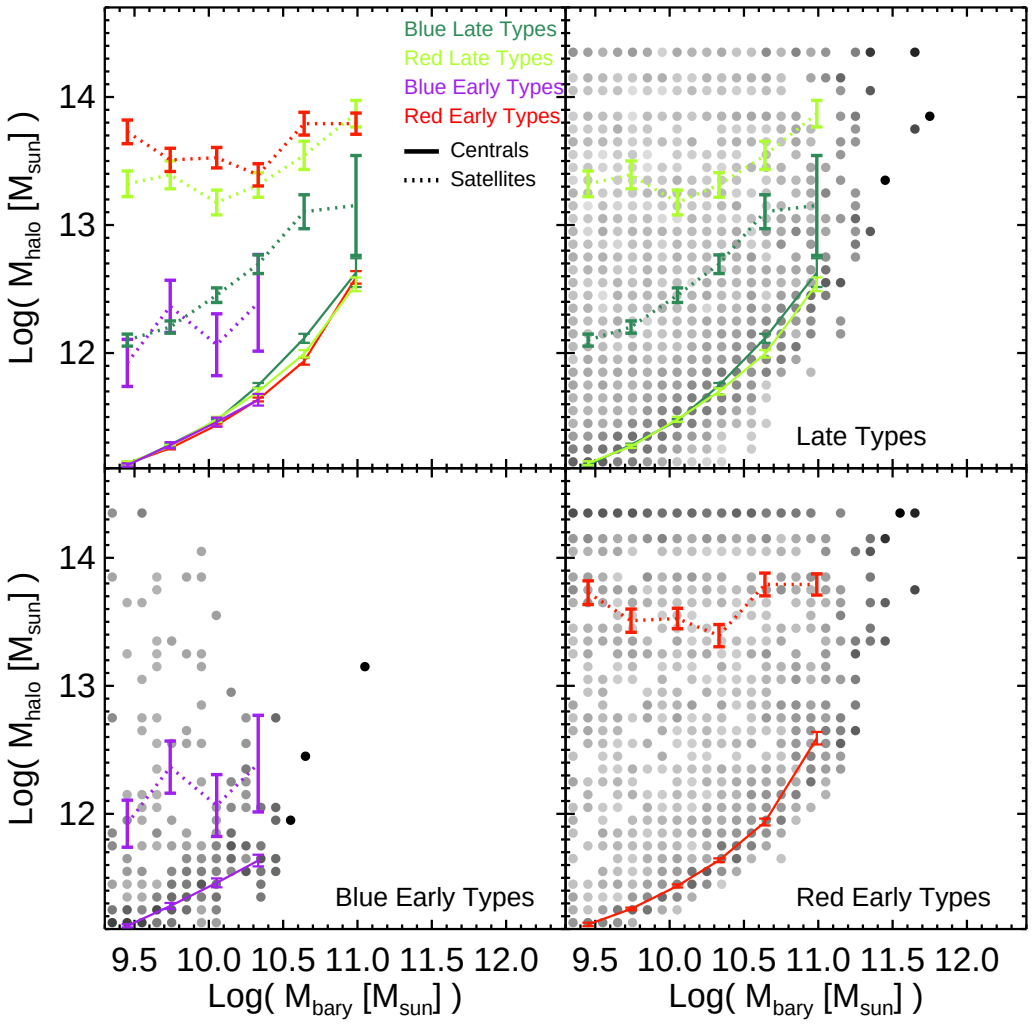

Figure 3.16 Characteristic distribution of halo mass as a function of baryonic mass for different galaxy types, with symbols and lines analogous to Fig. 3.15.

relation for low baryonic mass ($M_{bary} < 10^{10} M_{\odot}$) galaxies alone is approximately flat until group halo masses above $\sim 10^{13} M_{\odot}$ (see Fig. 3.12), where low baryonic mass galaxies are typically satellites. Accordingly, in the P(E|M) formulation, we find that a morphology-environment relation re-emerges for low baryonic mass satellites: early-type satellites typically occupy higher group halo mass environments than late-type satellites at constant baryonic mass.

Even though low mass blue early and blue late types occupy environments that are typically similar, their full environment probability distributions at a given mass may not necessarily be the same. In this case, we find K-S test $P_{same} \sim 0.01$ for the group halo mass distributions of $M_{bary} \lesssim 10^{10} M_{\odot}$ blue early and blue late types, where the blue late type environment distribution appears to be broader, indicating greater environmental diversity at fixed mass. Considering environmental density values (smoothed on $\sim$1.43 Mpc scales), we find that the typical densities around $M_{bary} \lesssim 10^{10} M_{\odot}$ blue early-type centrals are lower than those of late types until $M_{bary} \sim 10^{9.5} M_{\odot}$ where they again become similar (see Fig. 3.17a). If number density is more sensitive to major mergers than group halo mass, then this tendency towards somewhat lower environmental densities could be consistent with blue early-type centrals existing as post-merger objects with their number of neighbors reduced by merging. As with group halo masses, blue early-type and blue late-type satellites have similar typical densities in the $M_{bary} \lesssim 10^{10} M_{\odot}$ regime, and the overall blue early and blue late type density distributions in this mass regime have a $P_{same} \sim 0.07$ as quantified with the K-S test.

3.4.3 Extreme Gas Richness and Environment

Considering ECO+A galaxies of all types together, Fig. 3.18 shows that the fraction of gas-dominated galaxies (i.e., those with $M_{HI}/M_* > 1$) is a strong function of environment in general. The shape of the trend differs as a function of group halo mass compared to smoothed density field values: the halo mass relation displays a relatively smooth rise in gas-dominated galaxy frequency with a steep rise below $\sim 10^{11.4} M_{\odot}$, whereas the density relation shows an overall smooth rise in gas-dominated galaxies toward lower densities (compare Figs. 3.18a and 3.18b). The sharp increase in the frequency of extreme gas richness in our sample below $M_{halo} \sim 10^{11.4} M_{\odot}$ marks this as a regime where fractionally large gas reservoirs become a common feature of galaxies. Furthermore, we see that central galaxies are primarily responsible for the sharp increase in gas-dominated galaxy frequency with halo mass, within the baryonic mass limits of our sample (see Fig. 3.19).

If we consider the typical M_{HI}/M_* values as a function of environment for individual galaxy

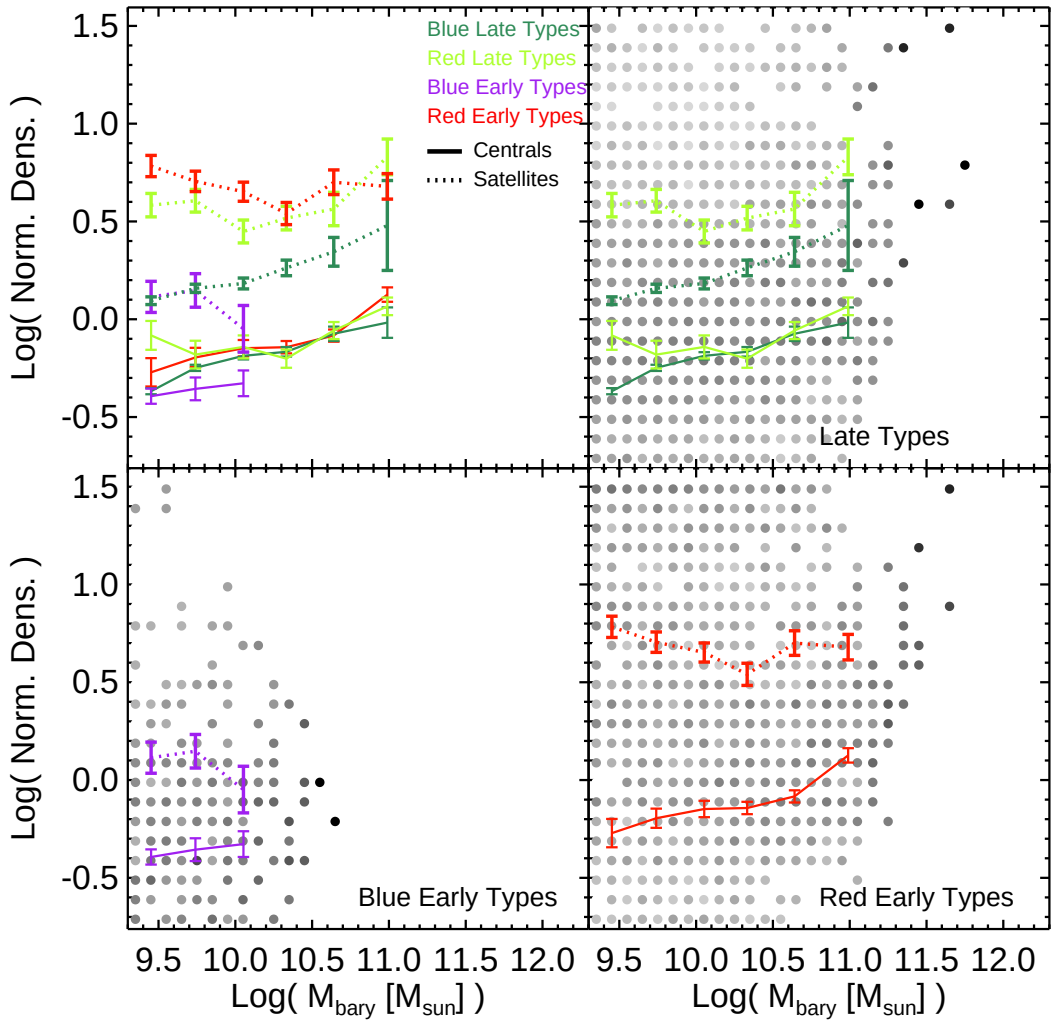

Figure 3.17 Characteristic distribution of environmental density (∼1.43 Mpc smoothing kernel) as a function of baryonic mass for different galaxy types, with symbols and lines analogous to Fig. 3.15.

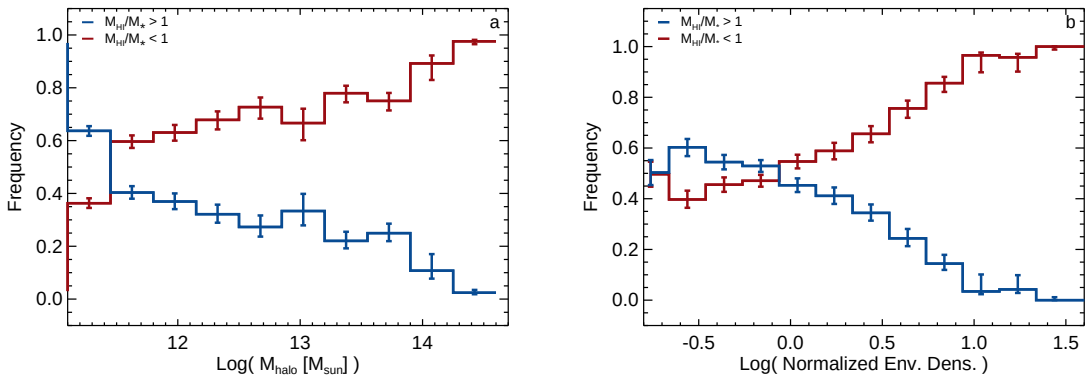

Figure 3.18 The environment-dependent frequency of HI gas-to-stellar mass ratios greater and less than one for ECO+A galaxies. The vast majority of ALFALFA α.40 derived HI limit values for ECO galaxies are sufficiently strong to place these galaxies in either the $M_{HI}/M_* > 1$ or $M_{HI}/M_* < 1$ category, but for any limit values found in the $M_{HI}/M_* > 1$ category, we replace these values with photometric gas fraction estimates as described in §3.3.7. If we leave the limit values in place and use no photometric gas fraction estimates, we still find trend lines that are within the error bars of the trends shown here. Confused sources in the ECO+A sample have been omitted. Panel *a* illustrates the sharp uptick of the gas-dominated galaxy frequency at low group halo mass, and panel *b* illustrates the smoother increase in gas-dominated galaxy frequency as a function of environmental density.

types in the full ECO sample, we find that in low halo mass environments blue early types display M_{HI}/M_* values that are comparable or somewhat lower than those of blue late types (see Fig. 3.20). We also observe that gas-dominated blue early types, with HI gas-to-stellar mass ratios > 1, are found almost entirely in low halo mass environments (see Fig. 3.21), becoming most common below a group halo mass of $\sim 10^{11.5} M_\odot$, where they are primarily group centrals (although again, any satellites would likely fall below our mass limit).

From Fig. 3.20, we find that satellite galaxies display typically higher gas-to-stellar mass ratios than centrals at fixed morphology, color type, and halo mass. The exceptions are blue late and red early types in the richest environments. It is somewhat surprising that higher satellite gas content appears to persist for red late types in rich environments where satellites are typically expected to be quenched, but we stress that in this gas-poor regime, many of our HI gas masses are estimated using optical colors. This photometric gas fraction technique is likely unreliable in dense environments (Cortese et al. 2011). Considering smoothed density field values results in trends that are similar to but weaker than the group halo mass trends illustrated in Fig. 3.20.

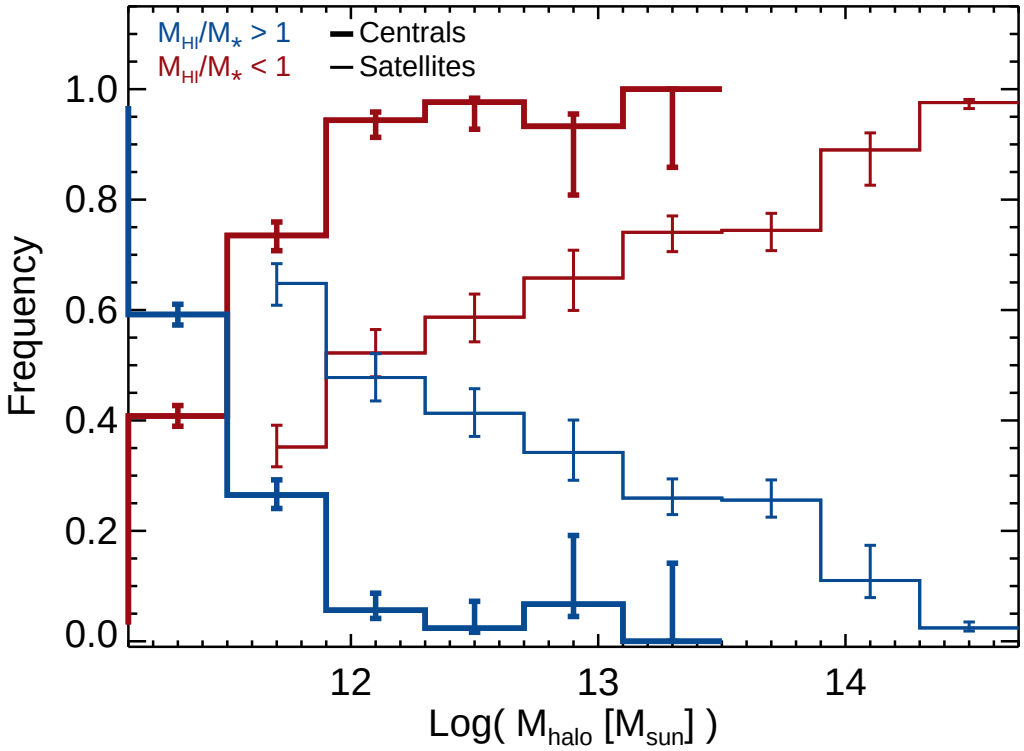

Figure 3.19 The frequency of HI gas-to-stellar mass ratios greater and less than one for ECO+A galaxies alone, plotted as a function of group halo mass for central (thick lines) and satellite (thin lines) galaxies separately. Confused sources in the ECO+A sample have been omitted. Since ECO contains relatively few satellite galaxies in $M_{halo} \lesssim 10^{11.5} M_{\odot}$ environments, we refrain from plotting satellite frequencies in this regime. Since ECO contains relatively few centrals above $M_{halo} \gtrsim 10^{13.5} M_{\odot}$, we likewise refrain from plotting central frequencies in this regime. Gas-dominated galaxy fraction increases significantly for low group halo mass central galaxies, particularly at $M_{halo} \lesssim 10^{11.5} M_{\odot}$.

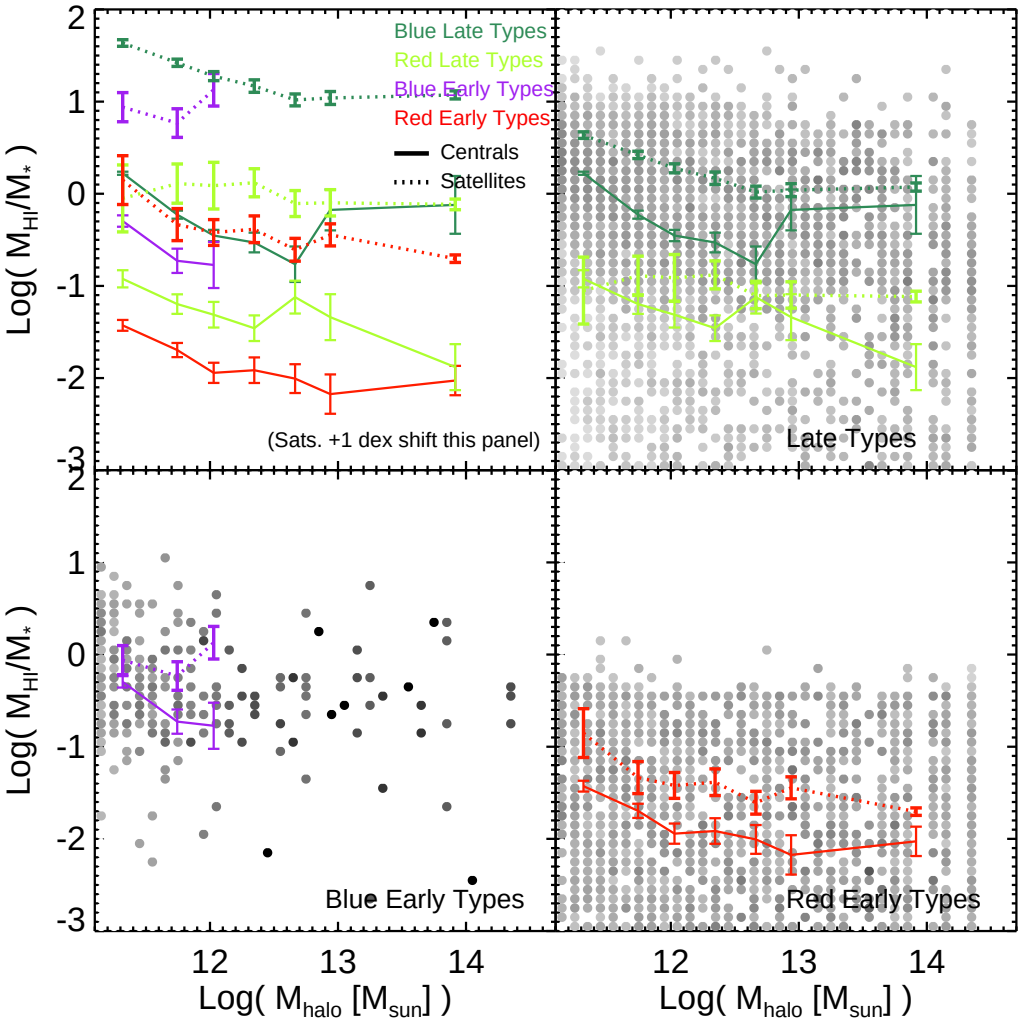

Figure 3.20 Characteristic distribution of HI gas-to-stellar mass ratio as a function of group halo mass for different galaxy types. HI gas masses are derived as described in §3.3.7. Symbols and lines are analogous to Fig. 3.15 except that in the upper left panel, all satellite median lines have been shifted upwards by the same amount for clarity.

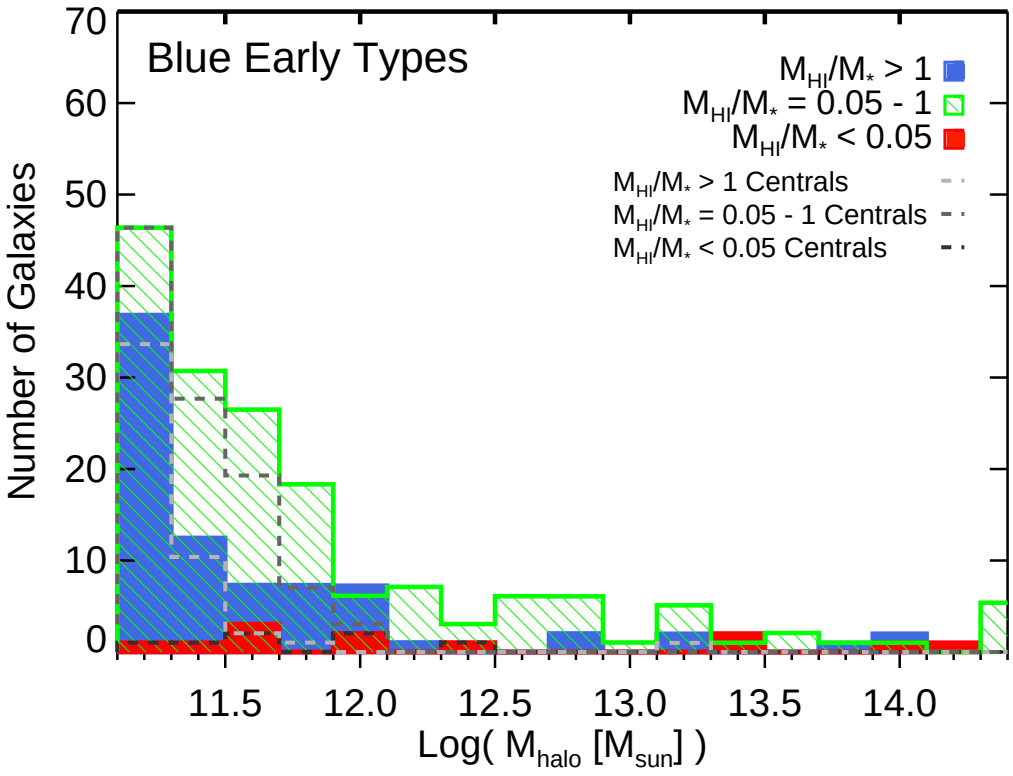

Figure 3.21 Halo mass distribution for blue early type galaxies in the ECO sample with different levels of HI gas. Corresponding greyscale dashed lines indicate the distribution for group central galaxies of each type. HI masses are derived as described in §3.3.7. Gas-dominated blue early types and blue early types with moderate gas-to-stellar mass ratios primarily inhabit environments with group halo masses below $\sim 10^{12} M_{\odot}$, with ∼65% of gas-dominated blue early types in $M_{halo} \lesssim 10^{11.5} M_{\odot}$ environments.

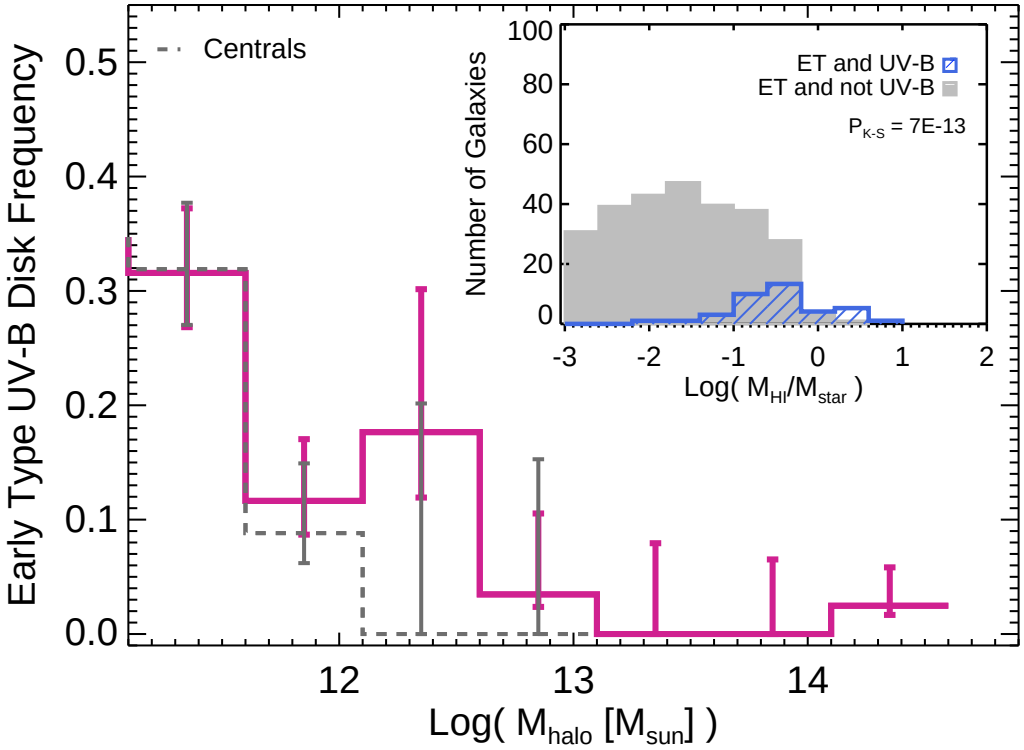

Figure 3.22 Frequency and gas content of early-type UV-B disk hosts in the ECO+G sample. The magenta line indicates the frequency of UV-B disks in early types as a function of group halo mass, and the grey dashed line indicates UV-B disk frequency among early-type centrals alone. The inset shows the distribution of HI gas-to-stellar mass ratios for UV-B and non-UV-B early types. HI gas masses are derived as described in §3.3.7. A strong preference towards higher gas-to-stellar mass ratios is observed for early-type UV-B disk hosts.

3.4.4 UV Disk Growth and Environment

In the ECO+G subsample, we find that UV-B disks are relatively common (Fig. 3.22), occurring with $34^{+1.5}_{-1.4}$% overall frequency. Fig. 3.22 shows that UV-B disks in early types rise from a few percent to ∼30-40% with decreasing group halo mass. The frequency of UV-B disks among early types in the low group halo mass regime is consistent with the reported UV-B disk frequencies of Moffett et al. (2012) for early-type galaxies in a low-to-intermediate stellar mass sample. UV-B disk frequency among early type galaxies rises sharply below $M_{halo} \sim 10^{11.5} M_{\odot}$, approximately the same halo mass scale below which blue-sequence early types and gas-dominated galaxies emerge. Within our sample mass range, UV-B disk early types below $M_{halo} \sim 10^{12} M_{\odot}$ are typically central galaxies, but additional satellite UV-B hosts with lower masses could also exist in these environments. Early type galaxies hosting UV-B disks show a strong tendency to host larger HI gas reservoirs than galaxies without UV-B disks (K-S test $P_{same} \sim 10^{-13}$; see Fig. 3.22), in agreement with results from Moffett et al. (2012) for low-to-intermediate mass early type galaxies. Overlapping in their typically gas-rich, low group and galaxy mass nature, blue-sequence early-type galaxies are often UV-B disk hosts, with 69^{+6}_{-7}% of blue-sequence E/S0s in the full ECO+G subsample hosting UV-B disks, or 80^{+5}_{-9}% in the low baryonic mass regime below $\sim 10^{10} M_{\odot}$.

3.5 Discussion

In this section, we compare our results on relationships between galaxy properties and environments to previous results in the literature and to galaxy evolution scenarios.

3.5.1 Morphology-Environment Relations

Comparisons to Previous Results

In general, we find that in the traditional P(M|E) morphology-environment relation formulation, our measured early and late type frequencies behave in a manner similar to that observed in previous studies of this relation, for example, with late-type galaxy frequencies decreasing from ∼80% in the least rich environments to much smaller frequencies in the most rich environments (e.g., Dressler 1980; Postman & Geller 1984; Whitmore et al. 1993). Examining early-/late-type frequencies as a function of group halo mass specifically, both Bamford et al. (2009) and Hoyle et al. (2012) find approximately constant frequencies in the high group halo mass regime ($\gtrsim 10^{13} M_{\odot}$), which we do not observe in the ECO sample. In addition to their default estimates for group mass based on

virial radius measures, Bamford et al. (2009) specifically test the use of summed luminosities as a proxy for group mass, using a definition close to that we employ, and find a very slightly more pronounced trend in the early-type fraction with this proxy, although still weaker than our trend. Similarly, Poggianti et al. (2009) find no significant frequency trend with cluster velocity dispersion but do find a trend with another proxy for group halo mass, X-ray luminosity. We note that the typical galaxy masses considered by these authors are higher than those considered in ECO, and when restricting to $M_{bary} > 10^{10} M_{\odot}$ galaxies alone, our early-/late-type frequency trends at the highest halo masses are relatively weak given the large error bars, except in the highest mass bin (see Fig. 3.12). Calvi et al. (2012) also find variations with galaxy mass, with their intermediate stellar mass galaxies showing similar morphological mixes in all environments except in the most massive clusters, which is compatible with the behavior of our $M_{bary} > 10^{10} M_{\odot}$ subsample. Bamford et al. (2009) likewise report that the form of the morphology-environment relation is strongly dependent on the stellar masses of the galaxies considered, with shifts in the overall frequency levels between subsamples. We find trends similar to the Bamford et al. results, where morphology-environment relations are similar in shape but offset between low and high mass subsamples in the sense that late-type frequencies are typically higher among low-mass galaxies (see Fig. 3.12). This offset may imply that for $M_{bary} < 10^{10} M_{\odot}$ galaxies, disks are either destroyed less frequently or regenerated more frequently than for higher mass galaxies.

Morphology-Environment Relations and Disk Regrowth

We next consider the specific question of whether or not morphology-environment relations operate in a manner consistent with the presence of disk regrowth. If morphological transformation operates primarily towards the destruction of disks in certain regimes but towards both the destruction and regrowth of disks in others, we would expect the balance of galaxy morphological types to differ in these regimes. In a scenario where large-scale gas accretion, whether arriving cold or hot, can fuel disk regrowth, the significance of such accretion is typically theorized to depend on the halo mass of the group in which a galaxy resides (e.g., Birnboim & Dekel 2003; Kereš et al. 2005; Nelson et al. 2013). Thus, in such a scenario, the balance of galaxy morphological types might naturally be expected to shift as a function of group halo mass. As previously mentioned, in the traditional morphology-environment relation, P(M|E), we observe a changing balance between early and late types as a function of group halo mass, in the sense that late types become more prevalent with decreasing halo mass. This trend is the sense in which the early/late type balance would be expected to

vary if disk regrowth were to preferentially occur at low group halo mass, however it is also certainly the sense in which one would expect the relation to vary if disks are typically destroyed/quenched at high but not low group halo mass. Thus, while consistent with a halo-mass dependent disk regrowth scenario, the observed traditional morphology-environment relation does not clearly constrain its existence. We also note that the balance between early- and late-type frequencies we observe in the ECO sample varies relatively smoothly as a function of group halo mass, as has often been observed by other authors. This smooth variation could indicate a lack of sharp transitions in the onset of morphological transformation processes at particular mass scales, but alternatively it could imply that the traditional relation, in lumping all early and all late types together, washes out possible sharper trends that may occur for subpopulations of galaxies.

Considering this question from the perspective of an alternative formulation of the morphology-environment relation, P(E|M), another expectation of the disk regrowth model emerges. If disk regrowth were to proceed from blue early to blue late types in a particular regime, then the typical environments of blue early and blue late types in that regime should be similar as these galaxies would represent snapshots of pre- and post-transition states. Such behavior was hinted at in the observation of a possible "inverse morphology-density relation" at low stellar masses by KGB. As illustrated in Figs. 3.16 and 3.17, we find that blue early and blue late type galaxies in the low baryonic mass regime below $\sim 10^{10} M_{\odot}$ inhabit environments with similar typical group halo masses at constant baryonic mass and with typical environmental *densities* of blue early types similar or slightly lower than those of blue late types. The P(E|M) formulation of the morphology-environment relation then appears to be consistent with the scenario of disk regrowth in the low baryonic mass regime. If gas accretion adds to both galaxy baryonic and overall halo mass during the regrowth process, individual galaxies could move along the M_{halo} vs. M_{bary} relation, but relatively significant changes in typical population properties would be necessary to make the blue early and blue late type populations distinct in this space given the scatter within each population. The slight trend towards lower number density environments for blue early types compared to blue late types possibly points to a post-merger status for blue early types. In the spirit of the alternative formulation of the morphology-environment relation, consideration of the typical environments of various subclasses of galaxies leads to further insights regarding environmental thresholds in disk growth as discussed in the next section.

3.5.2 The Regime of Extreme Gas Richness and Recent Disk Growth

We have presented multiple results that add up to the impression that extremely gas rich galaxies and those potentially regrowing disks are preferentially found in the low group halo mass ($M_{halo} \lesssim 10^{11.5} M_\odot$) and low galaxy mass ($M_{bary}$ or $M_* \lesssim 10^{10} M_\odot$, near the "gas-richness threshold" stellar mass at $M_* \sim 10^{9.7} M_\odot$) regime. We note that this regime is approximately defined, as in some cases we observe a continuum of galaxy properties in our sample, whereas in others, typically involving central galaxies, we see more abrupt transitions in properties between well-defined regimes. We find that ECO catalog blue-sequence early-type galaxies become most common in this low mass regime (see Fig. 3.14) and that blue early types with large gas fractions ($M_{HI}/M_* > 1$) also occur most commonly below a group halo mass of $\sim 10^{11.5} M_\odot$ (see Fig. 3.21). This group halo mass regime is also where extreme gas-to-stellar mass ratios commonly emerge in our sample, with a relatively sharp uptick as can be seen in Fig. 3.18. Likewise, we find that early-type galaxies most commonly host recent, UV-detected star formation in the form of UV-B disks in this low group halo mass regime (see Fig. 3.22). Such UV-B disk host galaxies also tend to be more gas rich than those galaxies without UV-B disks. Moreover, we find that the majority of low-mass, blue-sequence early types in our ECO+G subsample host UV-B disks.

A possible explanation for this constellation of results is that this low galaxy mass and low group halo mass region of parameter space represents a preferred regime where gas is abundantly available to galaxies, fueling star formation that allows many early types to live on the blue sequence, develop UV-B disks, and potentially even regrow larger disk structures. The existence of such a gas and star formation rich regime could be a symptom of a large-scale cosmological accretion process that is particularly efficient at supplying gas into galaxies at low mass scales. One such theorized process is "cold-mode" gas accretion, thought to preferentially act at group halo mass scales below this $\sim 10^{11.5} M_\odot$ mass scale at $z \sim 0$ (e.g., the $\sim 10^{11.3} - 10^{11.5} M_\odot$ scale of Kereš et al. 2005; Kereš et al. 2009). This model has recently been challenged by simulation results using the AREPO code, which imply that cold-mode accretion is not as significant for galaxies residing in low mass halos as previously thought, however these results suggest that accretion of heated gas is a more significant contributor in this regime, causing the level of gas accretion into low mass halos to remain high (Nelson et al. 2013). As seen in the simulations of Zehavi et al. (2012), from $z \sim 1$ to the present the bulk of the stellar mass growth in low-mass halos ($M_{halo} \lesssim 10^{12} M_\odot$) is still due to star formation, while in high-mass halos, such growth is mainly due to mergers.

Within the galaxy baryonic mass range we consider, we find that blue early-type and UV-B

disk host galaxies are typically centrals in the $M_{halo} \lesssim 10^{11.5} M_{\odot}$ regime (see Figs. 3.13b and 3.22). We also find that the strong uptick in gas-dominated galaxy fraction in this regime is primarily a central galaxy phenomenon, which may point towards accretion fueling of central galaxies in these environments (see Fig. 3.19). However, we also note that in the lowest halo mass environments we probe there are relatively few satellite galaxies within our baryonic mass range, and therefore it is plausible that gas-dominated, disk-growing satellites with lower masses could be common in such environments as well. From simulations, typical $z \sim 0$ gas accretion rates for satellite galaxies may be lower than for central galaxies (e.g., Kereš et al. 2009), but gas accretion may still play an evolutionarily significant role for satellites (e.g., Dekel & Birnboim 2006; Simha et al. 2009).

3.6 Conclusions

In this work, we have considered two primary galaxy samples, the Environmental COntext (ECO) catalog, and the B-semester region of the REsolved Spectroscopy Of a Local VolumE (RESOLVE) survey. Both samples reach into the high-mass dwarf galaxy regime and span a variety of environments, with the larger ECO catalog sample including the greatest environmental diversity. Through comparison to the more complete RESOLVE-B catalog, we apply corrections for incompleteness effects in ECO, creating an approximately baryonic mass limited catalog down to $10^{9.3} M_{\odot}$. In this analysis, we have employed high-quality, custom-reprocessed optical, near-IR, and UV photometry along with morphological classifications, atomic gas mass estimates, and multiple metrics of galaxy environment.

Our key results are as follows.

- We observe a traditional morphology-environment relation, P(M|E), similar to the expected form but with offset amplitudes between the low and high baryonic mass galaxy samples in the sense that late types are more common at low mass.

- We find the form of the traditional morphology-environment relation to be consistent with the scenario that morphological transformation from early to late types (disk regrowth) could occur in a preferred low group halo mass regime, although this relation does not strongly constrain the existence of this scenario.

- We consider an alternative form of the morphology-environment relation, P(E|M), which is instructive as a way of quantifying the *typical* environments of galaxies of various classes. This formulation leads to the observation that typical blue early-type and blue late-type galaxy

group halo masses are similar at constant baryonic mass, which is again consistent with expectations from the disk regrowth scenario. Likewise, the typical environmental densities of blue early types are similar or slightly lower than those of blue late types at constant baryonic mass, potentially reflecting a post-merger state for blue early types.

- The P(E|M) formulation of the morphology-environment relation also reveals that for $M_{bary} \lesssim 10^{10} M_{\odot}$ centrals, there is no discernible relationship between group halo mass and morphology: the typical halo masses for all early types and all late types are the same.

- We find that the low group halo mass regime below $\sim 10^{11.5} M_{\odot}$ is associated with the emergence of blue-sequence early types, gas-dominated galaxies, and early-type UV-Bright disk hosts as common contributors to galaxy populations. These three sub-populations are closely linked in this regime, implying the low group halo mass regime is a preferred regime for ongoing, significant disk growth.

These results lend strong support to the idea that theorized morphological transformation from early to late types can occur, particularly where galaxy and group halo masses are low. To investigate even more direct signatures of disk regrowth, we next turn to the examination of detailed early-type galaxy kinematics in the context of the RESOLVE survey, where the availability of such kinematic information combined with the type of environmental information considered here creates a unique opportunity for understanding the connection between galaxy properties on small and large scales.

We would like to thank R. Gonzalez, N. Padilla, S. Khochfar, and E. Feigelson for helpful discussions. AJM acknowledges funding support from a NASA Harriett G. Jenkins Fellowship, a University of North Carolina Royster Society of Fellows Dissertation Completion Fellowship, a North Carolina Space Grant, and *GALEX* GI grants NNX07AT33G and NNX09AF69G. SJK, KDE, DVS, and MAN acknowledge support from the NSF CAREER grant AST-0955368. KDE and DVS acknowledge additional support from GAANN Fellowships and North Carolina Space Grants.

Funding for SDSS-III has been provided by the Alfred P. Sloan Foundation, the Participating Institutions, the National Science Foundation, and the U.S. Department of Energy Office of Science. The SDSS-III web site is `http://www.sdss3.org`. SDSS-III is managed by the Astrophysical Research Consortium for the Participating Institutions of the SDSS-III Collaboration including the University of Arizona, the Brazilian Participation Group, Brookhaven National Laboratory,

University of Cambridge, Carnegie Mellon University, University of Florida, the French Participation Group, the German Participation Group, Harvard University, the Instituto de Astrofisica de Canarias, the Michigan State/Notre Dame/JINA Participation Group, Johns Hopkins University, Lawrence Berkeley National Laboratory, Max Planck Institute for Astrophysics, Max Planck Institute for Extraterrestrial Physics, New Mexico State University, New York University, Ohio State University, Pennsylvania State University, University of Portsmouth, Princeton University, the Spanish Participation Group, University of Tokyo, University of Utah, Vanderbilt University, University of Virginia, University of Washington, and Yale University.

Based on observations made with the NASA Galaxy Evolution Explorer. *GALEX* is operated for NASA by the California Institute of Technology under NASA contract NAS5-98034.

This publication makes use of data products from the Two Micron All Sky Survey, which is a joint project of the University of Massachusetts and the Infrared Processing and Analysis Center/California Institute of Technology, funded by the National Aeronautics and Space Administration and the National Science Foundation.

Table 3.1. ECO Sample Properties

Gal. ID	RA (deg)	Dec (deg)	cz (km/s)	M_r	$\log \mathrm{M}_*/M_\odot$	$(u-r)^e$	$(u-J)^m$	$R_{50\%}$ ($''$)	$R_{90\%}$ ($''$)	M	F_M	Grp. ID	Grp. cz (km/s)	F_C	$\log \mathrm{M}_{halo}/M_\odot$	Dens.	F_A	F_{HI}	F_G	CC
ECO5536	130.689	28.521	5552.5	-18.82	9.17	1.12	2.67	5.1	11.6	L	1	5476	5557.0	1	11.29	0.61	0	1	0	1.05
ECO0486	130.781	18.222	6170.1	-20.33	10.19	1.59	3.68	14.3	29.2	L	2	1689	6170.1	1	11.55	0.48	0	1	0	1.02
ECO5668	130.922	28.623	5561.4	-18.36	8.83	0.95	1.77	15.0	38.7	L	1	5476	5557.0	0	11.29	0.62	0	1	0	1.07
ECO1118	131.035	34.717	4193.7	-21.36	10.43	1.16	3.23	23.7	43.0	L	2	2122	4193.7	1	11.96	0.19	0	1	0	1.05
ECO4664	131.058	22.137	4668.2	-18.72	8.77	0.92	1.93	4.4	10.5	L	1	4711	4668.2	1	11.16	0.22	0	2	0	1.07
ECO6374	131.090	9.538	3904.9	-18.07	8.85	0.89	···	13.4	27.2	L	2	2221	3937.9	0	11.78	0.84	1	1	0	1.05
ECO1217	131.129	18.286	6136.3	-20.96	10.05	1.31	3.01	10.6	27.5	L	1	277	6143.7	1	11.93	0.58	0	1	0	1.05
ECO6369	131.135	9.166	3935.2	-18.38	8.97	0.90	2.62	9.6	19.6	L	2	2221	3937.9	0	11.78	0.78	1	1	0	1.05
ECO1312	131.178	9.801	3929.6	-18.87	9.27	1.04	2.73	12.5	27.5	L	2	2221	3937.9	0	11.78	0.86	1	1	0	1.04
ECO1413	131.182	10.472	3937.0	-19.80	9.43	1.19	2.37	22.1	47.2	L	2	2255	3937.0	1	11.40	0.82	1	1	0	1.04
ECO1562	131.316	9.646	3982.2	-20.59	9.81	1.40	2.40	18.3	38.6	L	1	2221	3937.9	1	11.78	0.85	1	1	0	1.00
ECO2728	131.317	27.824	6388.7	-20.27	9.27	1.16	0.86	31.3	52.8	L	1	3200	6388.7	1	11.53	0.55	1	2	0	1.01
ECO2729	131.357	32.949	6396.6	-19.75	9.65	1.15	2.81	9.4	18.5	L	2	3201	6396.6	1	11.38	0.17	0	2	0	1.03
ECO5247	131.368	36.731	6706.5	-18.65	9.05	0.98	2.13	7.6	15.5	L	2	5147	6706.5	1	11.15	0.25	0	1	0	1.05
ECO1497	131.408	36.935	3904.8	-20.51	10.15	1.19	3.38	5.9	18.4	E	1	2306	3904.8	1	11.60	0.32	0	1	0	1.01

Note. — A portion of Table 3.1 is shown here for guidance regarding its form and content; this complete table will be made available as a machine-readable file. Velocities (cz) are given in local group corrected form. M indicates early or late type morphology, and F_M is a flag that indicates the source of the classification: 1 for quantitative cut and 2 for by eye from Lintott et al. (2011). Group ID numbers, center velocities (local group corrected), central/satellite designations, and halo masses are given by the Grp. ID, Grp. cz, F_C (1 indicates central), and $\log \mathrm{M}_{halo}/M_\odot$ columns. Dens. indicates normalized environmental density smoothed ∼1.43 Mpc scales. F_A is a flag with value equal to 1 where a galaxy belongs to the EC0+A sample. F_{HI} is a flag indicating whether: (1) photometric gas estimates or (2) gas measurements were used for each galaxy. F_G is a flag with value equal to 1 where a galaxy belongs to the EC0+G sample. CC indicates the completeness correction factor applied to each galaxy.

CHAPTER 4: SECONDARY DISKS AND DISK REGROWTH IN RESOLVE S0S

Early-type galaxies are predicted to regrow late-type disks in hierarchical models of galaxy formation, but observational confirmation of this process has thus far been largely indirect. We approach this problem kinematically by investigating direct evidence of disk regrowth in the form of extended secondary disks in S0 galaxies. This project is currently a work in progress, and in the following analysis, we use the data obtained for the project that currently exist in a final reduced form.

4.1 Introduction

A variety of observational evidence, involving the detection of photometric signatures of star formation and of gas reservoirs that fuel star formation, has recently emerged to support the predicted occurrence of stellar disk regrowth around E/S0 galaxies (e.g., KGB; Wei et al. 2010; Donovan et al. 2009; Cortese & Hughes 2009; Thilker et al. 2010; Moffett et al. 2012; Stark et al. 2013). Kinematic identification of disk regrowth signatures, through the presence of spatially extended secondary stellar disks, should provide a more direct approach to probing the existence of this phenomenon.

However, the incidence of extended secondary stellar disks in early-type galaxies, as traced by the presence of counterrotation, remains poorly constrained at present. Stellar-stellar counterrotation was first discovered in the central regions of Elliptical galaxies (Bender 1988; Franx & Illingworth 1988; Jedrzejewski & Schechter 1988) and was subsequently found to occur in a spatially extended sense in a number of individual early-type galaxies (e.g., Galletta 1996 and references therein). Kuijken et al. (1996) found a 24% frequency of *gas*-stellar counterrotation in 17 S0s, but in their full sample of 28 (including 6 gas-stellar counterrotators), they found no stellar-stellar counterrotators and estimated the incidence at <10%. Likewise, the SAURON project found little evidence for extended stellar counterrotation in E/S0s, though Emsellem et al. (2007) identify kpc-scale kinematically decoupled cores (KDCs), believed to form in late-stage merger remnants. Over a primarily lower mass range than either study, Kannappan & Fabricant (2001) found a 4/17 (24%) incidence of gas-stellar counterrotation in E/S0s, and 3/4 of the gas-stellar counterrotators display probable stellar-stellar counterrotation (KGB), implying that stellar-stellar counterrotation could be more

common at low stellar masses where disk regrowth is thought to be most active.

The environment distribution of galaxies hosting stellar-stellar counterrotation is also poorly constrained at present. However, since E/S0 disk regrowth may preferentially occur in low density environments where large gas reservoirs are common (see Chapter 3), it is natural to expect that stellar-stellar counterrotation could possibly display a similar environmental preference.

To examine direct kinematic signatures of stellar disk regrowth and constrain the incidence and demographics of stellar-stellar counterrotation, we have carried out deep spectroscopy of a broad sample of 59 S0 galaxies selected from a single volume-limited survey. We select our S0 sample to be broadly distributed in stellar mass and environment, allowing us to investigate potential mass- and environment-dependent rates of counterrotation. We also sample both red and blue S0 targets, since color information can help to distinguish extended counterrotation associated with disk regrowth from extended counterrotation that may be produced from specific merger conditions, as in the case of NGC 4550 a red-sequence counterrotator that is thought to have formed in a coplanar merger of oppositely rotating galaxies (Crocker et al. 2009).

In §4.2, we describe our sample, data, and analysis methods in detail. In §4.3, we report and discuss results from this analysis, including our observed total extended stellar-stellar counterrotation frequency of $25^{+12}_{-9}\%$ and the absence of statistically significant trends in counterrotation incidence with mass, environment, or color. In §4.4, we provide a brief summary and discuss avenues for future inquiry.

4.2 Data and Methods

Throughout this analysis, we calculate distances according to $D = cz/H_0$ and take the value of the Hubble constant to be $H_0 = 70\ km\ s^{-1}\ Mpc^{-1}$.

4.2.1 Sample

We select our sample from the REsolved Spectroscopy Of a Local VolumE (RESOLVE; Kannappan et al., in prep.) survey, a volume-limited survey of two regions of space with a total volume of $\sim$50,000 Mpc^3 in the cz range 4500 km/s to 7000 km/s. RESOLVE probes galaxies down into the high-mass dwarf regime, with a nominal baryonic mass limit of $\sim 10^9 M_\odot$, which inhabit a diversity of environments. We consider for selection RESOLVE galaxies that exhibit S0 morphology, i.e., a central bulge and smooth outer disk, as judged from Sloan Digital Sky Survey r-band images (Abazajian et al. 2009) and agreed upon by two separate classifiers (AM and M. Norris). We further

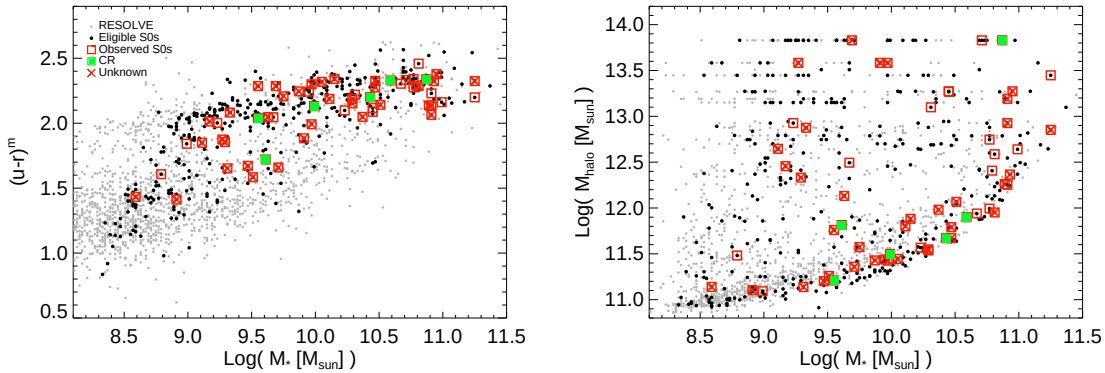

Figure 4.1 RESOLVE deep S0 spectroscopy sample in the parameter spaces of model color vs. stellar mass (left panel) and group halo mass vs. stellar mass (right panel). Small grey dots show all RESOLVE survey galaxies, and larger black dots indicate RESOLVE S0s eligible for the sample selection considered here (see §4.2.1 for details). Red boxes indicate observed deep S0 spectroscopy targets. Green filled boxes indicate identified stellar-stellar counterrotators, and red x's indicate targets with currently unknown counterrotation status due to either in-progress data reduction or insufficient final data quality (see Table 4.1 for details). Targets with unknown status are omitted from the calculation of all counterrotation statistics reported here.

require that our targets have photometrically estimated inclination angles <70° to avoid targeting galaxies that are too face on for obtaining reliable rotation measurements and have Tully-Fisher relation (Tully & Fisher 1977) estimated velocity width >120 km/s to avoid targeting galaxies for which we cannot resolve split velocity peaks with our observations.

The original goal of this project was to observe 72 RESOLVE S0s that satisfy the aforementioned criteria, allowing us to sample 3 separate bins in both environment and galaxy mass with 24 objects per bin for analyzing mass or environment separately and 8 objects per bin for analyzing mass and environment jointly. Due to weather- and instrument-related observing time losses, we have thus far observed 59 unique S0 targets for this program. Within the constraints of available observing time allocations, we have subselected targets from the potential RESOLVE S0 target pool in order to simultaneously sample the diversity of RESOLVE S0s in stellar mass, environment (quantified by group halo mass), and color parameters, where these values have been calculated according to the methods described in §3.3. This sample is distributed broadly over the ranges occupied by eligible RESOLVE S0s in mass, environment, and color parameters as illustrated in Fig. 4.1.

In this analysis, we consider a sample consisting of the 34 targets for which our final data reduction is complete. However, we find that our data quality is sufficient to confidently classify counterrotators using the methods described in §4.2.3 for only 24 of these targets. For 3 targets (rs1148, rf0413, and rf0096), the data in hand have such low S/N that we refrain from analyzing

them further here. For 2 of these targets, we have obtained less than half of the typical exposure time sought for our program, and for the other target, additional observations will be needed to improve the S/N to a usable level. For 7 targets we analyze that have currently uncertain counterrotation status, the uncertainty is typically due to relatively poor spatial sampling of individual high S/N binned spectra across the galaxy. For many of these targets, a confident counterrotation identification may be possible by an optimized method that is less reliant on the existence of many individual spatial sampling points, but for at least two targets (rs0328 and rs1228), additional observations are likely necessary to obtain confident classification results. Of the 10 targets with reduced data but uncertain classifications at present, 4 have had their S/N levels reduced by the presence of significant scattered light in our observations (see §4.2.2). For 25 additional targets with observations we have not yet reduced with our final pipeline, we believe our data quality will typically be high enough for analysis and counterrotation identification, barring two questionable cases where the total exposure times obtained are significantly below our usual exposure time objective (rs1190 and rf0455). In 14 of the not-yet-reduced observations that were taken in the early stages of this program, the data have lower resolution than is standard for our later data. However, we believe these lower-resolution data will be usable in our final analysis given appropriate treatment of the relevant counterrotation detection limits. Thus, we believe that a total of up to 7 of our 59 targets may require further observations in order to yield confident counterrotation classifications. The full details of our sample and observations are summarized in Table 4.1.

4.2.2 Observations and Data Reduction

We have used the 4.1m SOAR telescope and Goodman Spectrograph (Clemens et al. 2004) to carry out deep longslit or image slicer spectroscopic observations of our RESOLVE S0 sample. Typical major axis exposure times of $\sim$2 hours, carried out primarily in "darkest" sky conditions were necessary to measure stellar kinematics to sufficient galactocentric radii to identify extended secondary disk structures in our targets. Our standard observing pattern involves multiple 1200s major axis exposures with a comparison lamp spectrum between each exposure. To mitigate the effects of atmospheric differential refraction (see Filippenko 1982), we confine our typical observations to airmass $<$2 and further to airmass $<$1.2 for the broadest wavelength coverage observations (taken in the 1200 l/mm grating setup; see Table 4.1). Strict airmass requirements combined with long exposure times necessitates spanning most of our observations over multiple nights. On each night, we take bias, flat field, and scattered light "pseudo-dark" calibration frames. These pseudo-dark

calibrations are exposures taken in a dark dome with exposure times ideally matching the maximum exposure times of our science frames and were needed during periods when stray light signatures were observed in Goodman Spectrograph data. Since the level and structure of the stray light were both constant over the course of a given observing night, except on A-semester 2011 nights as noted in Table 4.1, subtracting these pseudo-dark calibration frames from the science frames in our data reduction procedure allowed generally clean removal of stray light from our data.

Our instrumental setup was chosen to target a wavelength range covering 4500-5550 Angstroms at minimum, allowing the examination of absorption line features that trace the stellar kinematics (Hβ, Mgb, Fe5270 and Fe5335). Due to evolving capabilities of the Goodman Spectrograph, we have used a variety of grating and slit combinations to achieve this wavelength coverage and our desired resolution targets. Our typical instrumental setup used the Goodman Spectrograph's 2100 l/mm VPH grating and 1.03" longslit, with resulting typical FWHM resolution $\sim$1 Angstrom or equivalent velocity resolution of $\sigma \sim 25$ km/s. A wider 1.68" longslit was chosen for the most massive targets so that their larger velocity widths could be similarly well sampled but observed more efficiently, requiring less observing time per object. Before the 2100 l/mm grating was installed on the Goodman Spectrograph, different longslits were chosen to approximate these same resolution constraints while using a 1200 l/mm grating. Lower-resolution observations taken prior to the B-semester of 2010 will also be used in forthcoming analysis for this project as appropriate (see full setup details in Table 4.1).

At the time of observation, initial binning in the spatial direction to $\sim$0.3" pixels was applied, which is well within the typical minimum seeing of $\sim$1" on our observing nights. Further spatial binning is applied in post processing using an adaptive binning algorithm that bins together individual spectral rows of our final reduced frames until a specified continuum S/N target is achieved. In this analysis, we use a S/N target of 10 per Angstrom, estimated using the final error frames that result from our data reduction procedure (see description below). Even though absorption line kinematics studies often target S/N $\gtrsim$ 20, lower S/N levels are reasonable for the cross-correlation analysis we perform (e.g., Kregel et al. 2004 and references therein), and several spatial sampling points are averaged together when interpreting our velocity dispersion measurements. Each adaptively binned spectral row we analyze is considered to lie at the galactocentric radius at which half its total flux was reached.

Our data are reduced with a custom IDL pipeline developed for RESOLVE SOAR/Goodman

spectroscopic data reduction, which consists of both customized IDL reduction routines and wrapper codes for standard IRAF routines. This pipeline has been optimized for processing Goodman Spectrograph data taken in stock RESOLVE survey configurations, and minor modifications to the pipeline procedures have been made to allow processing of our deep S0 data, with its variety of configurations that differ from typical RESOLVE survey products. The data reduction procedures include standard methods of overscan/bias subtraction, flat fielding, and wavelength calibration along with custom methods of exposure alignment and stacking, spatial curvature rectification, and sky subtraction originally developed by Kannappan (2001). We also apply cosmic ray removal using the Laplacian cosmic ray identification algorithm of van Dokkum (2001, L.A.Cosmic), which allows cosmic ray rejection even when insufficient numbers of exposures exist for rejection during the frame stacking process. For data taken on observing nights with detectable stray light, we subtract a combined pseudo-dark frame from the science frames. When pseudo-dark frames have been taken that match the exposure times of the science frames, we subtract the pseudo-dark levels in these frames directly, but otherwise we scale the pseudo-dark signal by the ratio of the science exposure time to the pseudo-dark exposure time. After pseudo-dark subtraction, we inspect the resulting science frames for under- or over-subtraction. If under- or over-subtraction has occurred based on the simple exposure time scaling of the pseudo-dark frame, we rescale the pseudo-dark frames accordingly and repeat the subtraction procedure. This approach typically removes the stray light signal from our data cleanly, adding only to our noise levels, except in cases noted in Table 4.1 where variable stray light levels and/or structure yield low-level residuals in the science frames after pseudo-dark subtraction.

We carefully track all sources of error associated with each final reduced science frame by combining error frames that include the bias variations, Poisson errors on pseudo-dark levels (where applicable), flat-field variations, and Poisson errors on signal in each science frame. The combined error frame associated with each science frame is then transformed in the same manner as the data when a wavelength solution is applied. The resulting error frame is also rectified in the same manner as the data when the spatial curvature correction is applied. Individual error frames are aligned and combined, adding in quadrature, to match the corresponding final stacked science frame. These final error frames are used in our adaptive spatial binning procedure as previously described.

4.2.3 Identification of Stellar-Stellar Counterrotation

To identify stellar-stellar counterrotation in our targets, we analyze the reduced, binned spectra in multiple spatial sampling regions along each target's major axis and extract stellar kinematics from both template cross-correlation and spectral fitting methods. As template spectra, we use the 0.55 Angstrom FWHM resolution stellar population synthesis models of Maraston & Strömbäck (2011), based on the ELODIE stellar library (Prugniel et al. 2007) and using a Kroupa IMF (Kroupa 2001). We consider a grid of simple stellar population templates with [Fe/H] options -0.3, 0, and 0.3 and age options 0.1, 0.3, 0.5, 1, 1.5, 2, 3, 4...15 Gyr.

To extract the detailed stellar velocity profiles of our targets, we use the IRAF rvsao package and the xcsao task (Kurtz et al. 1992) to cross-correlate our final spectra with the previously described grid of template spectra in Fourier space. Emission line regions are removed from the spectra and interpolated over in this analysis, and the continuum levels are also removed so that stellar absorption lines are the basis for comparison between observed and template spectra. The xcsao analysis yields a cross-correlation profile in velocity space, with peak height equal to the correlation R value, at each spatial sampling point and for each template spectrum. We examine the cross-correlation profile that results from comparison to the highest R value template spectrum in each spatial sampling region and construct velocity profile plots (see leftmost panels of Figs. 4.2-4.17). Galaxies that have counterrotating stellar components will display characteristic X-shaped structure in the velocity peaks in such plots (e.g., as shown in Fig. 4.13).

To provide a quantitative basis for our identification of stellar-stellar counterrotation, we also extract stellar rotation curve and velocity dispersion measurements by fitting template spectra to our observed spectra using the penalized pixel-fitting method implemented in the pPXF routine (Cappellari & Emsellem 2004). In this analysis, we mask regions of line emission from the input spectra, and since pPXF is computation time intensive, we restrict our template spectra set to full range of ages but only the [Fe/H] value that provided the best correlation with the central region of each galaxy in the xcsao analysis. The pPXF routine is allowed to mix the template spectra to create a composite population if such a population provides the best fit. To extract kinematic information, pPXF shifts template spectra by possible velocities and broadens them by possible velocity dispersions, fitting these templates to the observed spectra. We use the pPXF output stellar velocity dispersion measurements and their error bars as the basis for our quantitative counterrotator identification.

In a disk galaxy with a single rotating disk component, stellar velocity dispersion is expected

to be greatest in the central galaxy bulge region and to decrease with increasing galactocentric radius. When two significant extended counterrotating stellar disks are present, the stellar velocity dispersion can instead be seen to remain similar to the central value or even increase further at large radii. We define a "central" stellar velocity dispersion by the measurement-error-weighted average of velocity dispersion measurements obtained inside the $R_{50\%}/8$ (r-band) radius for each galaxy and an "outer" stellar velocity dispersion by the measurement-error-weighted average of velocity dispersion measurements obtained outside the $R_{50\%}/4$ radius or the more extended $R_{50\%}/2$ radius, where such measurements exist, for each galaxy. If the lower 1-sigma error bound of the outer stellar velocity dispersion is greater than or equal to the central velocity dispersion for a given galaxy, then we consider this galaxy to be a strong stellar-stellar counterrotator. The choice of central and outer region radii are motivated by the velocity dispersion variations with radius we observe (see rightmost panels of Figs. 4.2-4.17), where stellar velocity dispersion is typically at a maximum within $R_{50\%}/8$ and a minimum outside of $R_{50\%}/4$. We note that this quantitative identification method is also a work in progress and classifies two targets (rs1300 and rs1079) as counterrotators even though they do not display obvious X-shaped cross-correlation profile structure. This identification method may be optimized further with future analysis, potentially including consideration of the degree to which velocity profiles deviate from a Gaussian form.

4.3 Results and Discussion

Of the S0 targets for which we have final reduced data products in hand, we find that our data quality is high enough to perform the aforementioned analysis and counterrotation identification procedure, requiring multiple spatial sampling points across each galaxy, for 24 targets (see detailed cross-correlation and velocity/dispersion profiles in Figs. 4.2-4.17). Of the 24 confidently classified galaxies, we identify 6 targets that exhibit strong counterrotation signatures, satisfying our quantitative counterrotation metric and typically displaying characteristic X-shaped patterns in their velocity cross-correlation profiles (galaxies noted with green filled boxes in Figs. 4.1 and "C" in 4.2-4.17; see also Table 4.1). Thus, we find the frequency of strong stellar-stellar counterrotation among S0s in our sample to be $25^{+12}_{-9}\%$, which agrees with the stellar-stellar counterrotation frequency results of KGB but not Kuijken et al. (1996).

As can be seen in Figure 4.1, these stellar-stellar counterrotators are broadly distributed in the parameter spaces of color vs. stellar mass and group halo mass vs. stellar mass, although most appear to inhabit low group halo mass environments. Considering each of these parameters individually,

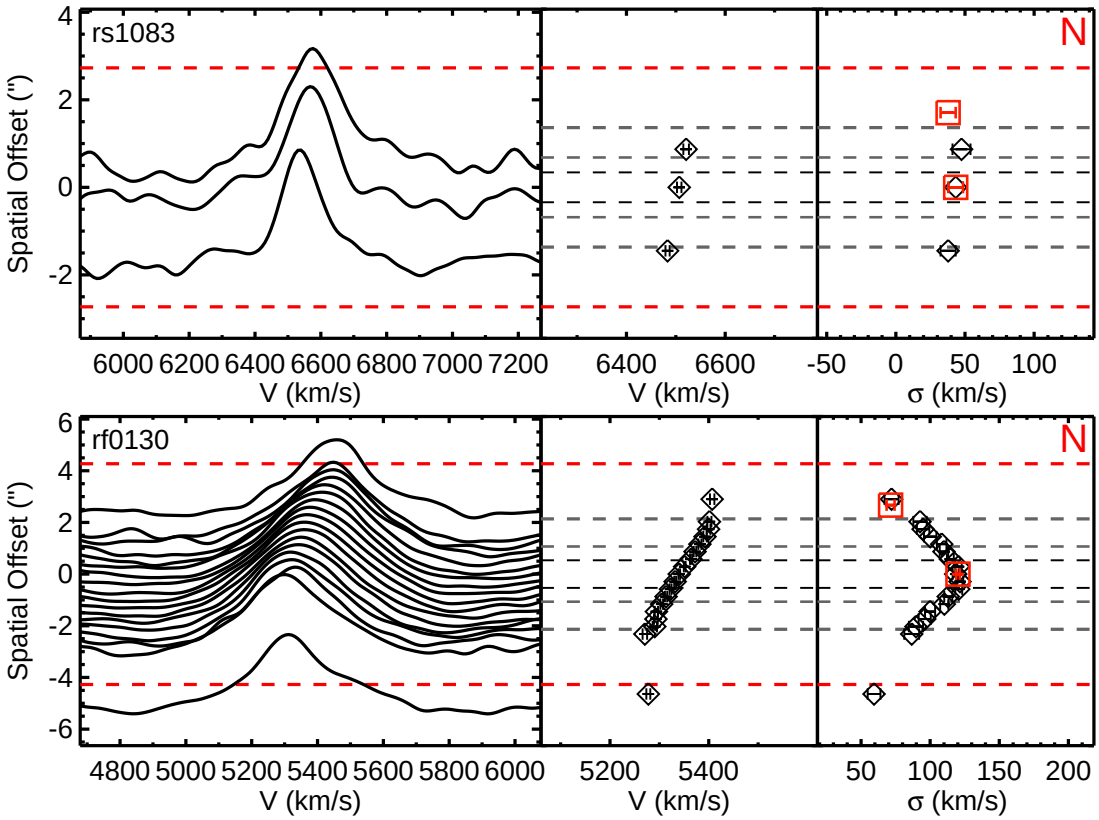

Figure 4.2 Stellar cross-correlation profiles (leftmost panels) plus rotation (center panels) and velocity dispersion (rightmost panels) measurements as a function of spatial offset from galaxy center for observed targets in the RESOLVE deep S0 spectroscopy sample. The dashed horizontal red lines indicate r-band $R_{50\%}$ radii, and successive grey/black horizontal dashed lines indicate the $R_{50\%}/2$, $R_{50\%}/4$, and $R_{50\%}/8$ radii. Large red square points on the rightmost panel indicate average central and outer velocity dispersion values (with 1-sigma error bars) used for classification of counterrotating galaxies (see §4.2.3). Counterrotation status is indicated by red letters "C" (counterrotating), "N" (not counterrotating), and "U" (uncertain) in the upper right corner of this panel.

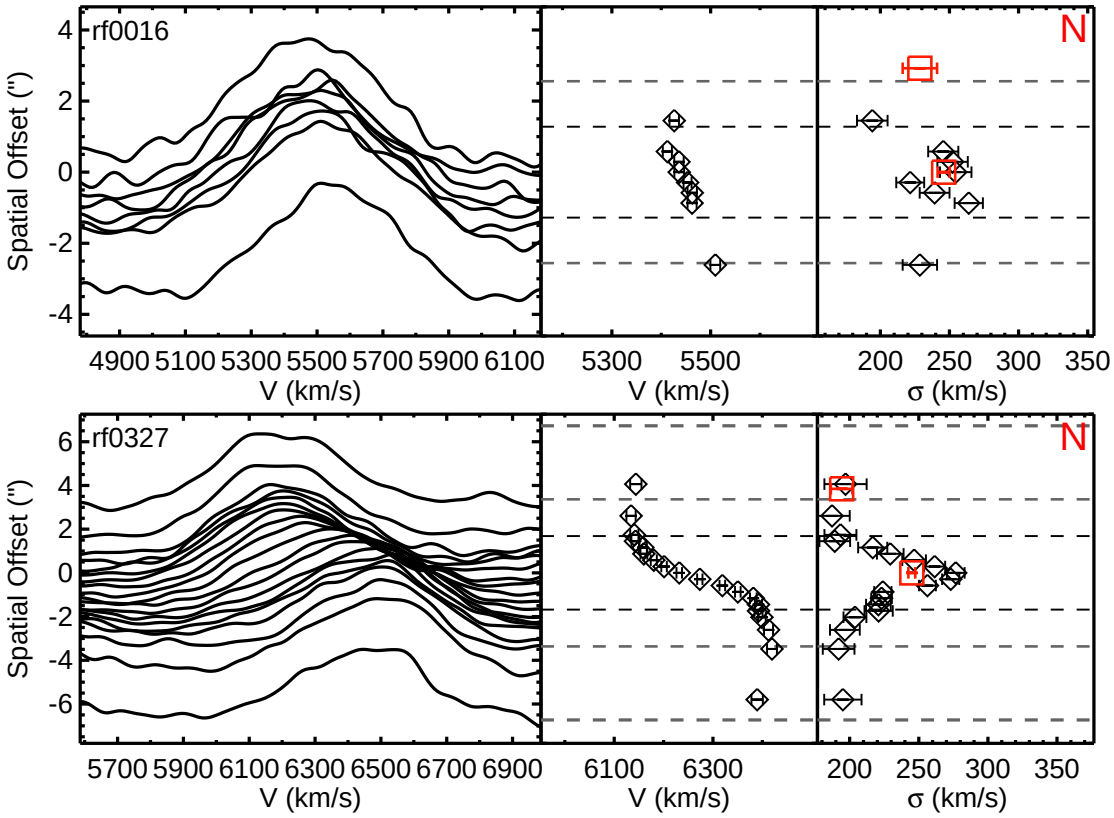

Figure 4.3 Cross-correlation profiles plus rotation/velocity dispersion measurements (cont.).

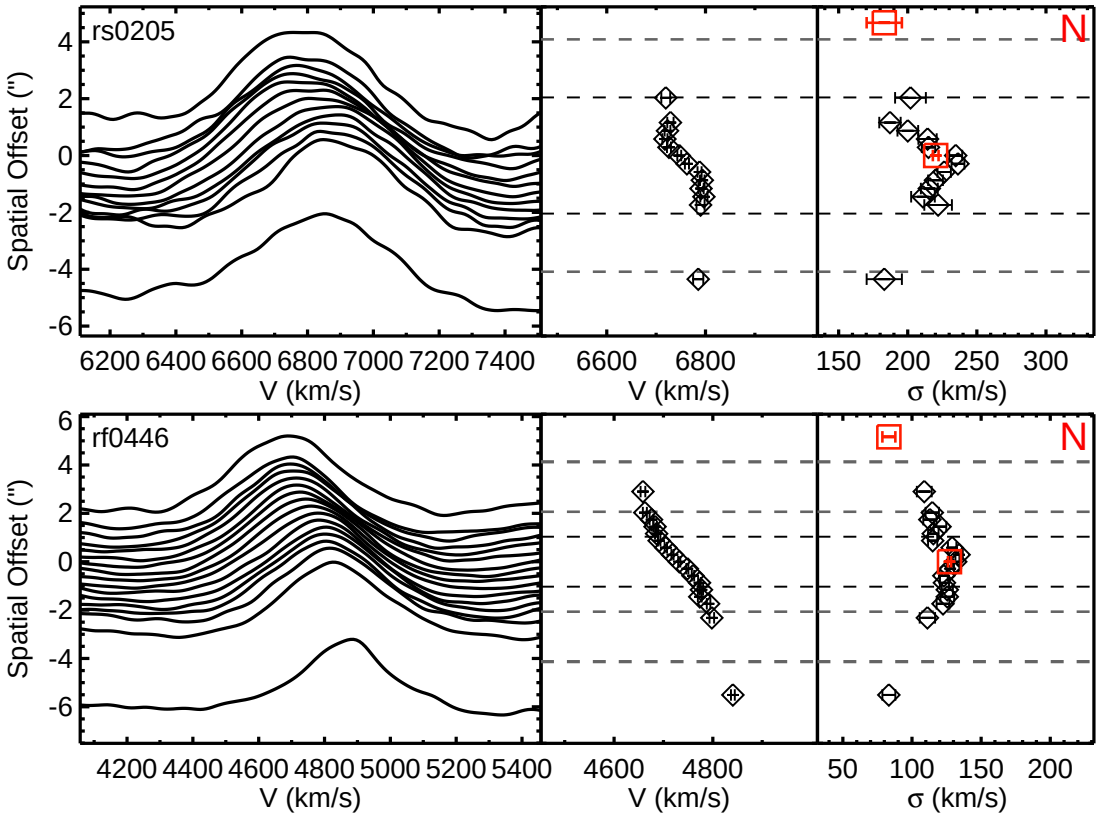

Figure 4.4 Cross-correlation profiles plus rotation/velocity dispersion measurements (cont.).

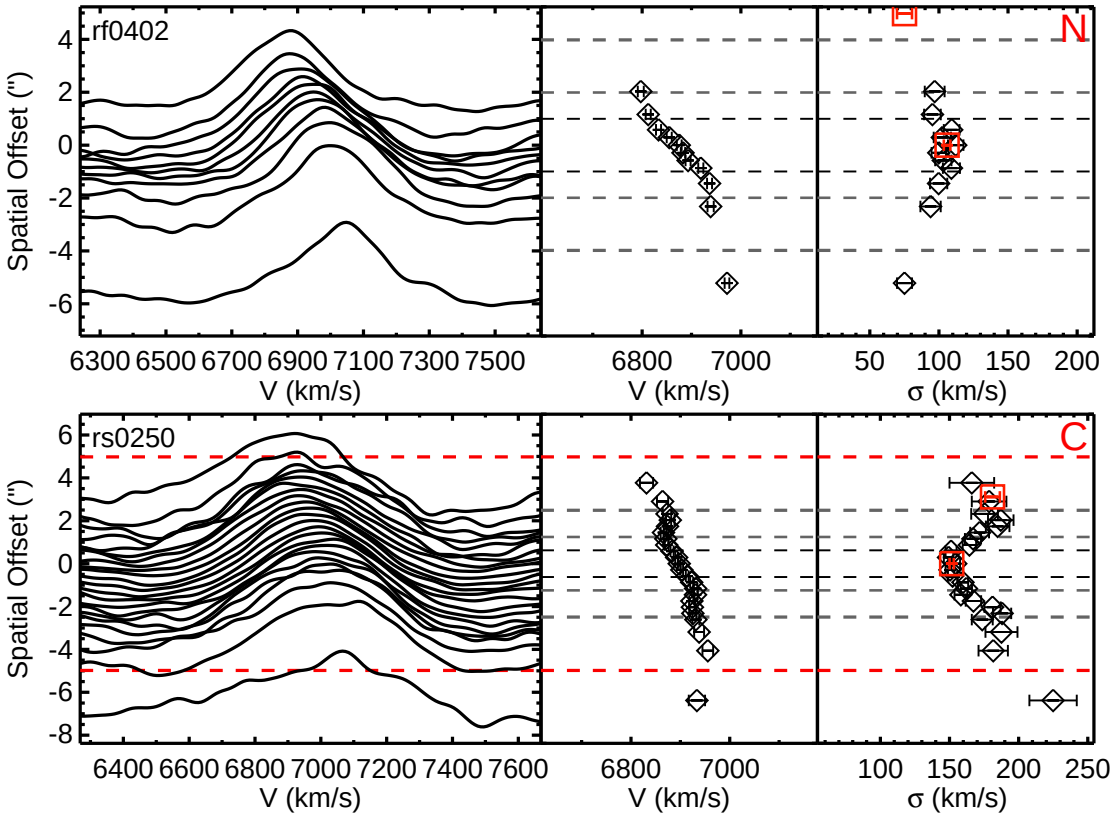

Figure 4.5 Cross-correlation profiles plus rotation/velocity dispersion measurements (cont.).

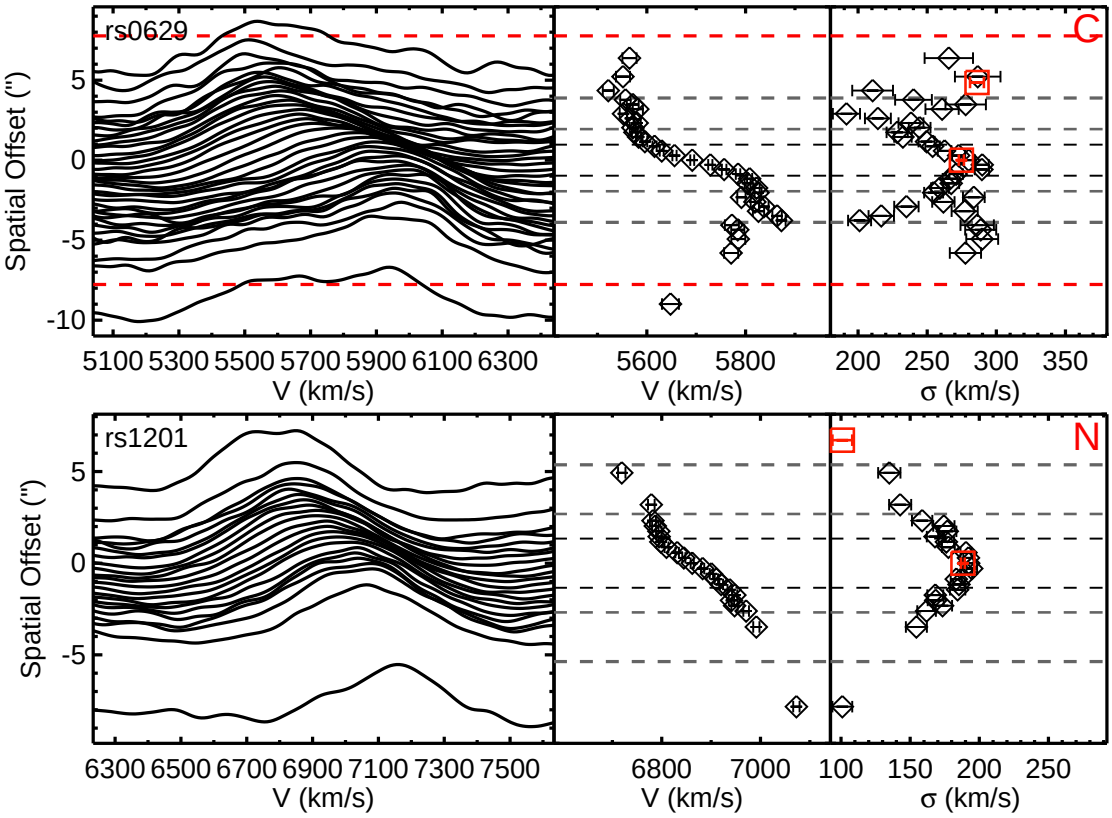

Figure 4.6 Cross-correlation profiles plus rotation/velocity dispersion measurements (cont.).

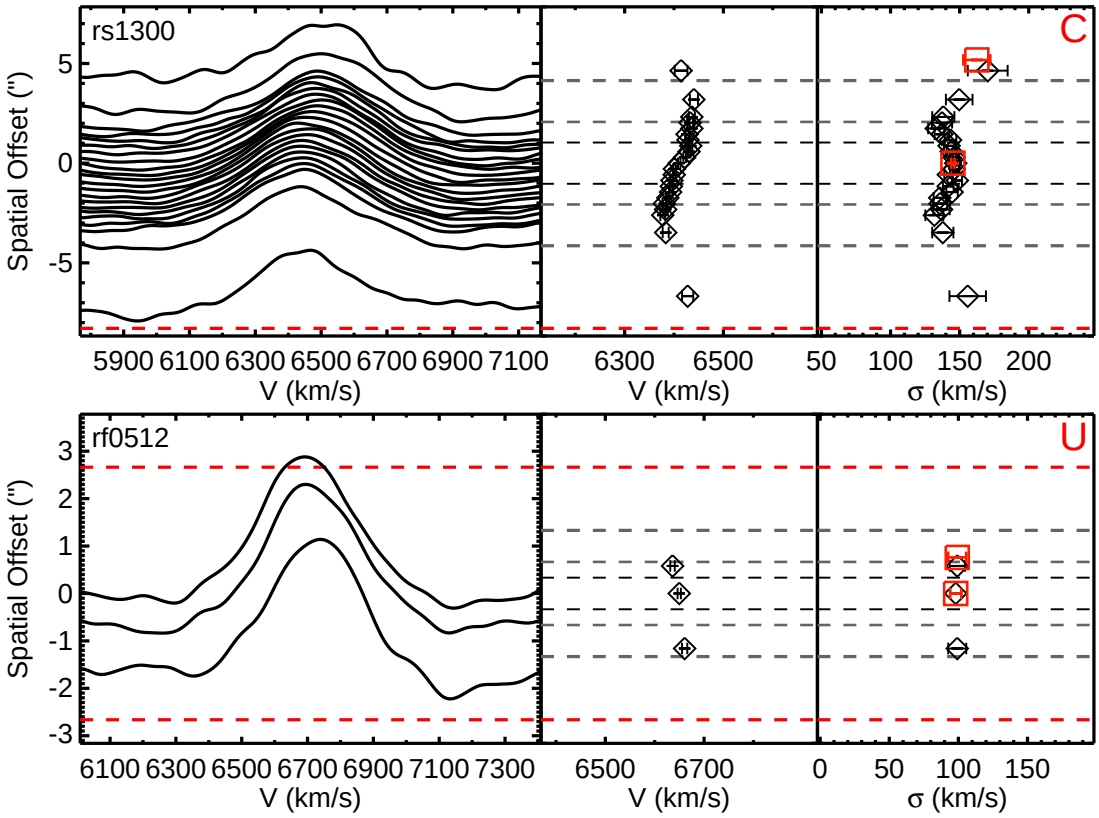

Figure 4.7 Cross-correlation profiles plus rotation/velocity dispersion measurements (cont.).

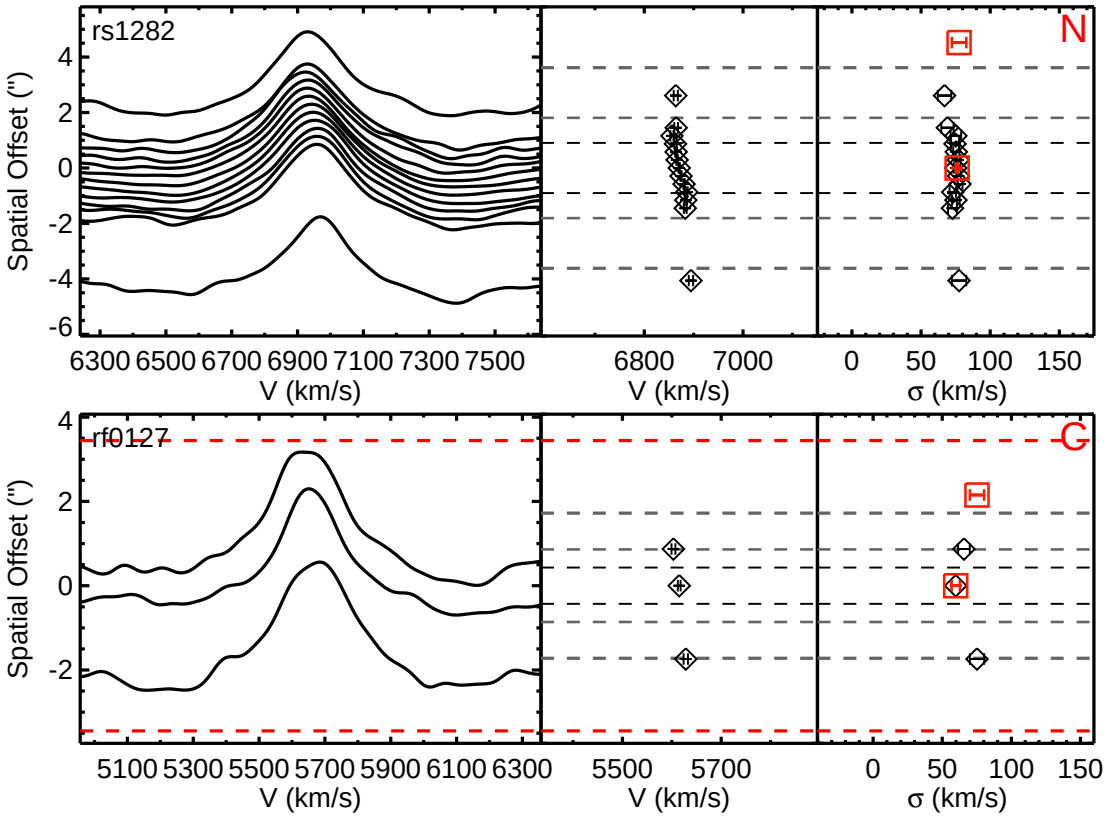

Figure 4.8 Cross-correlation profiles plus rotation/velocity dispersion measurements (cont.).

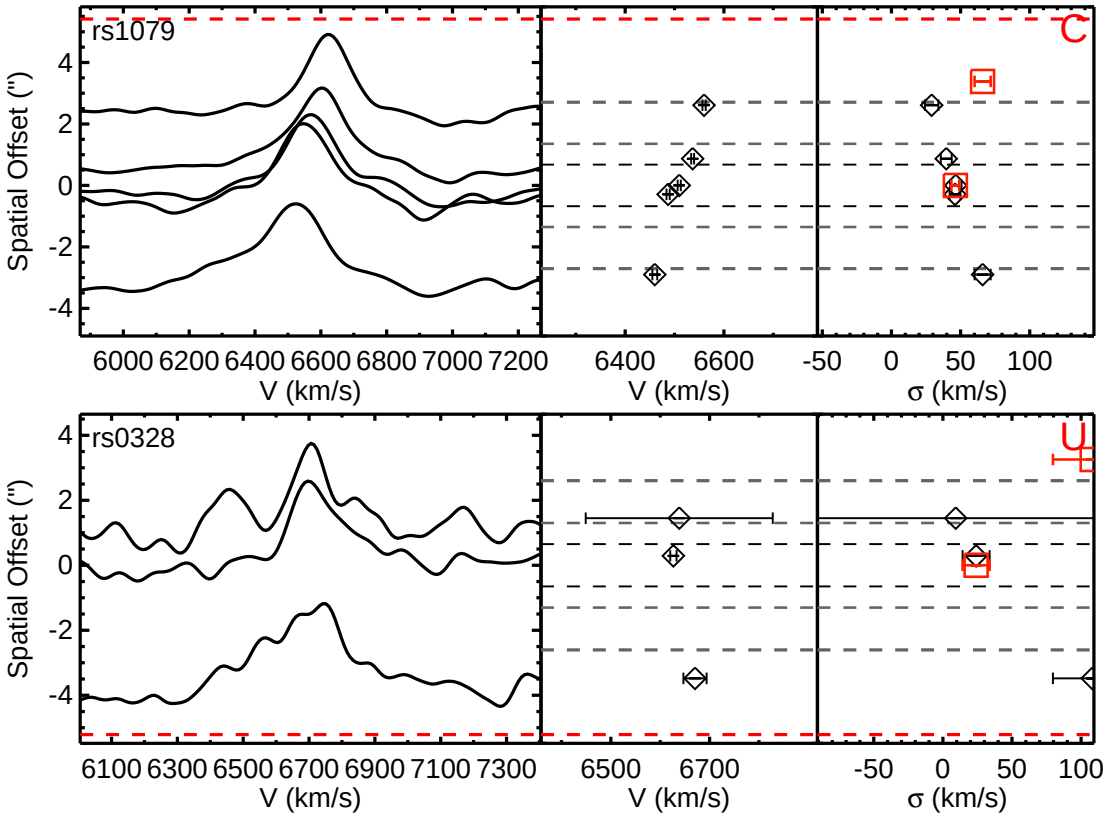

Figure 4.9 Cross-correlation profiles plus rotation/velocity dispersion measurements (cont.).

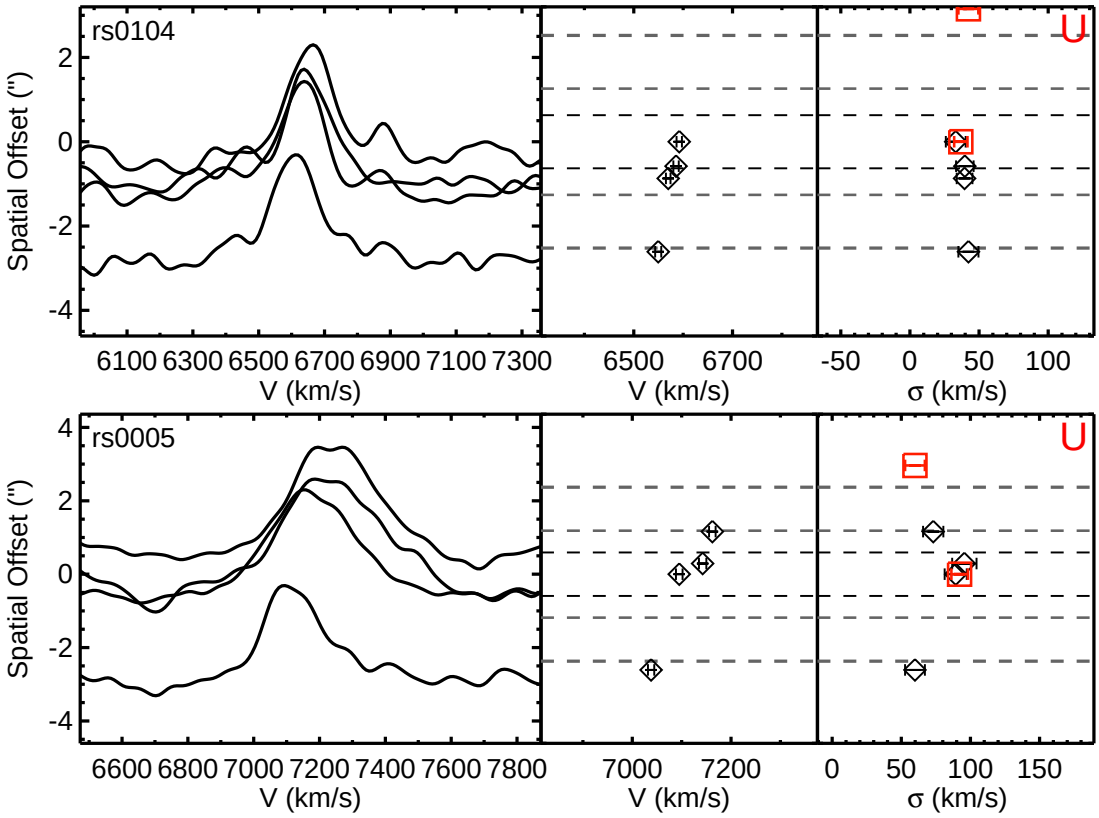

Figure 4.10 Cross-correlation profiles plus rotation/velocity dispersion measurements (cont.).

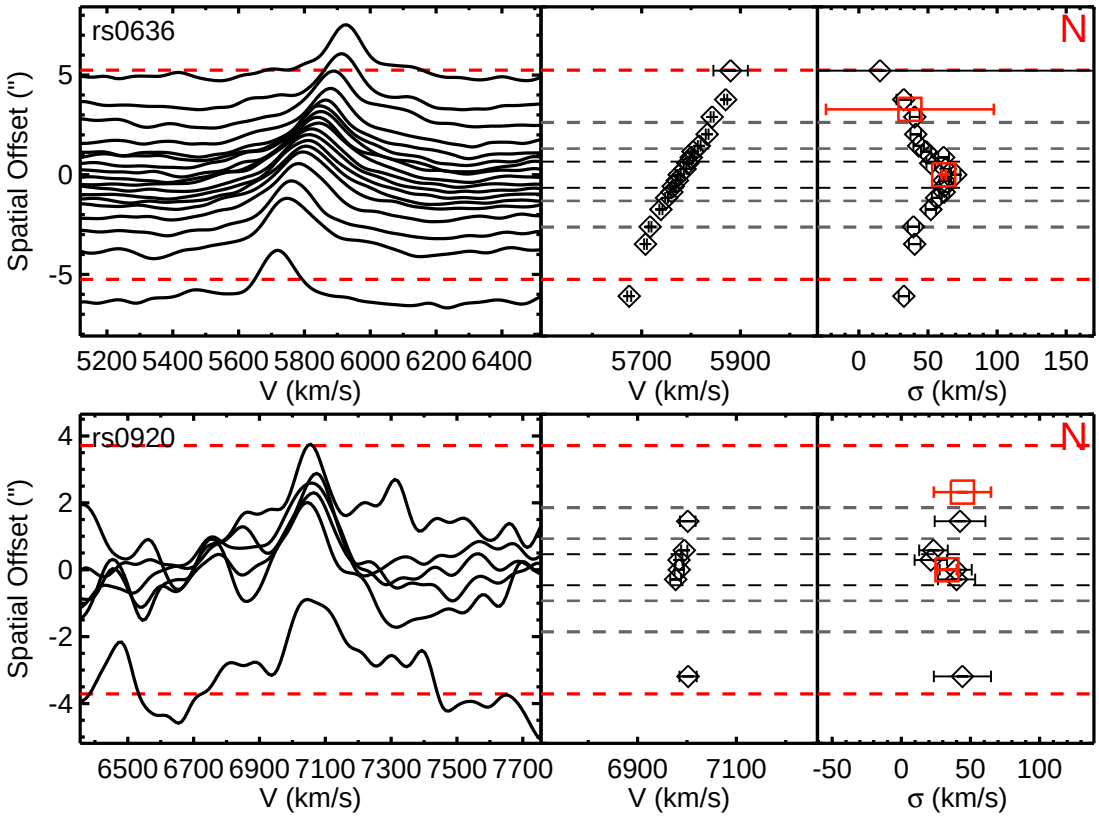

Figure 4.11 Cross-correlation profiles plus rotation/velocity dispersion measurements (cont.).

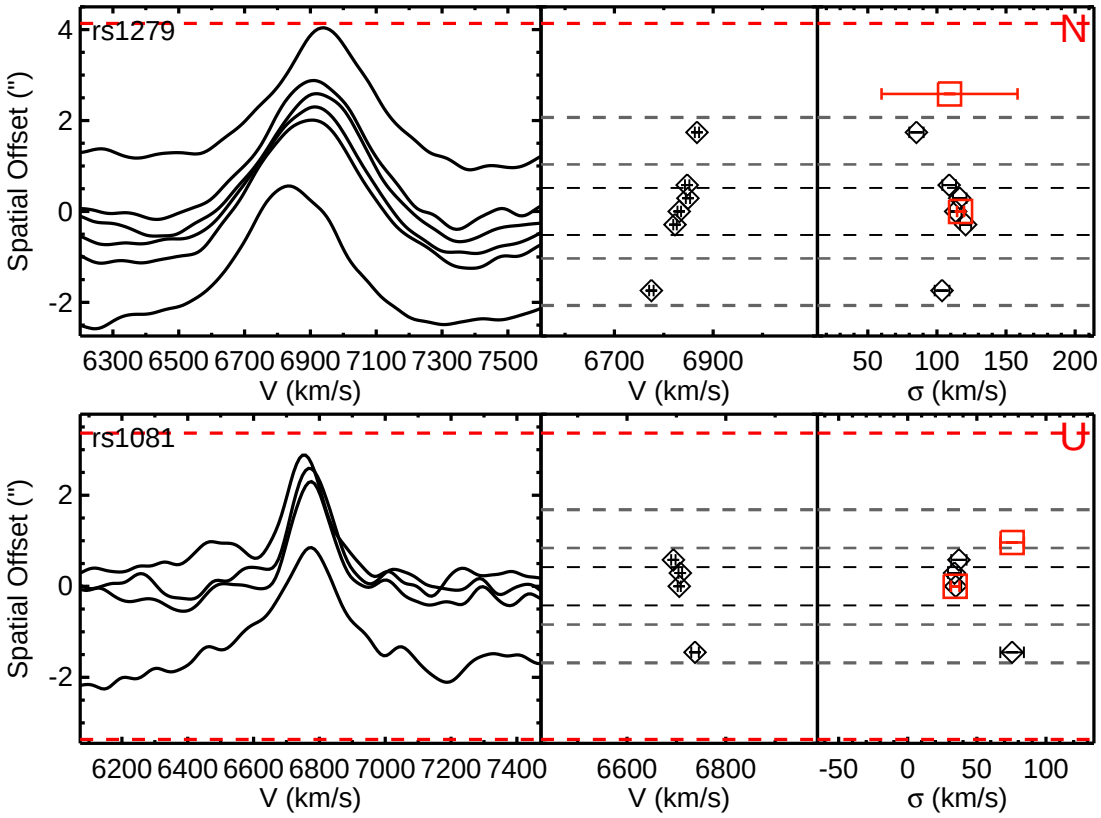

Figure 4.12 Cross-correlation profiles plus rotation/velocity dispersion measurements (cont.).

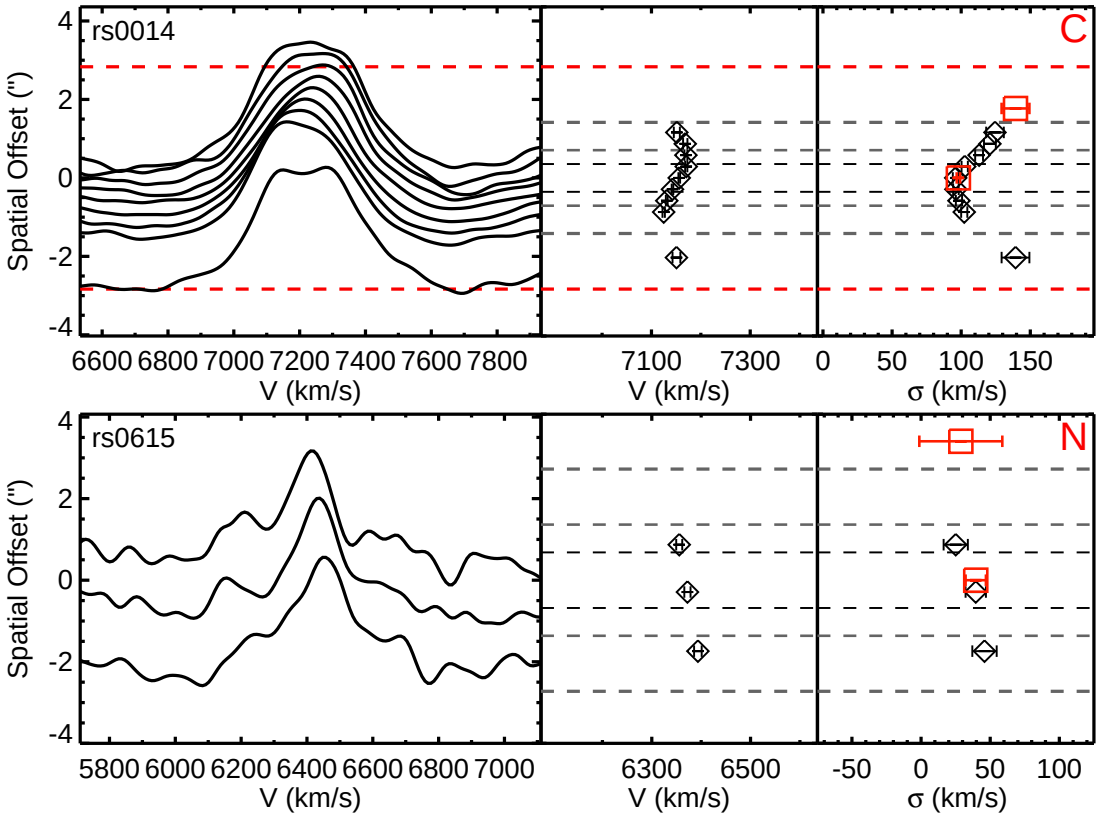

Figure 4.13 Cross-correlation profiles plus rotation/velocity dispersion measurements (cont.).

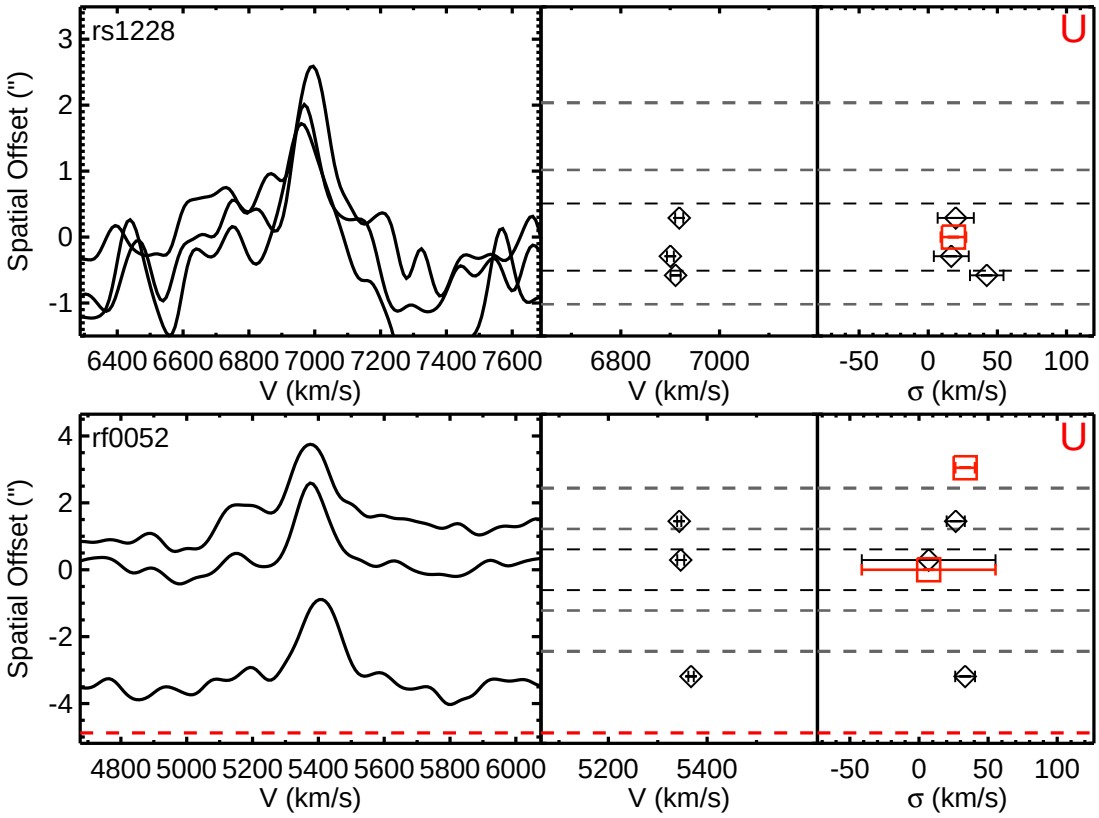

Figure 4.14 Cross-correlation profiles plus rotation/velocity dispersion measurements (cont.).

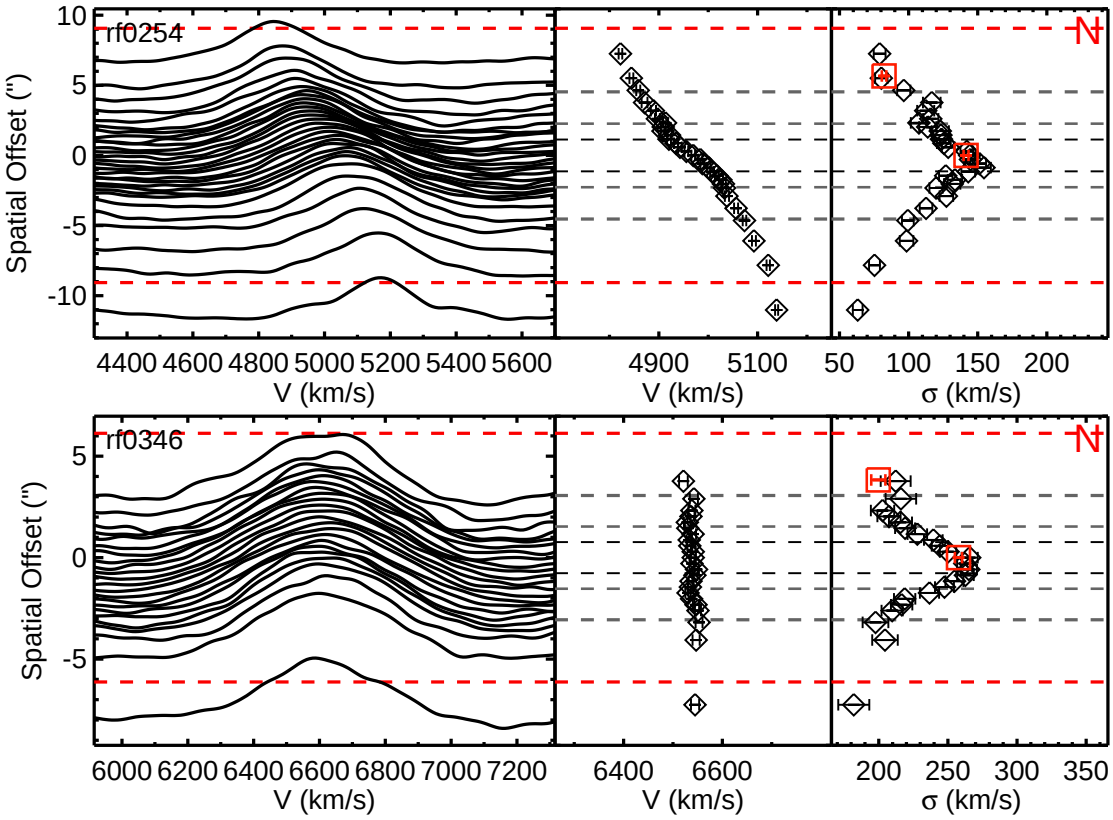

Figure 4.15 Cross-correlation profiles plus rotation/velocity dispersion measurements (cont.).

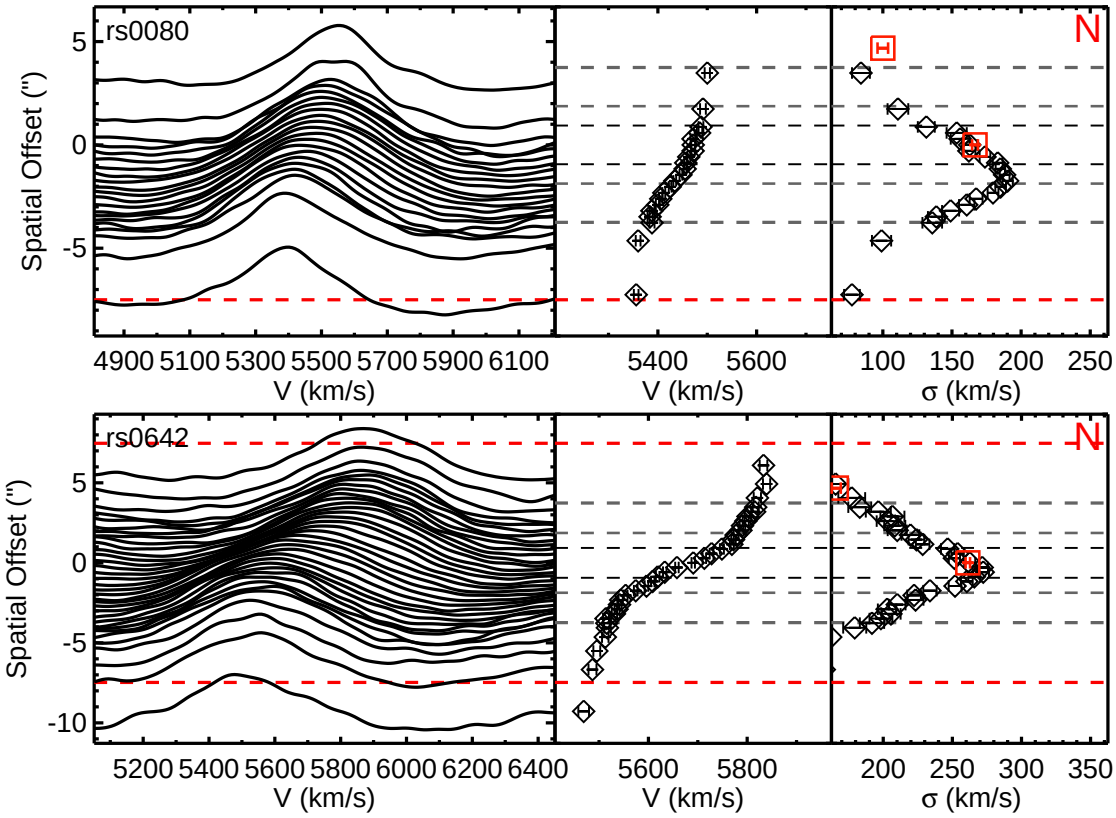

Figure 4.16 Cross-correlation profiles plus rotation/velocity dispersion measurements (cont.).

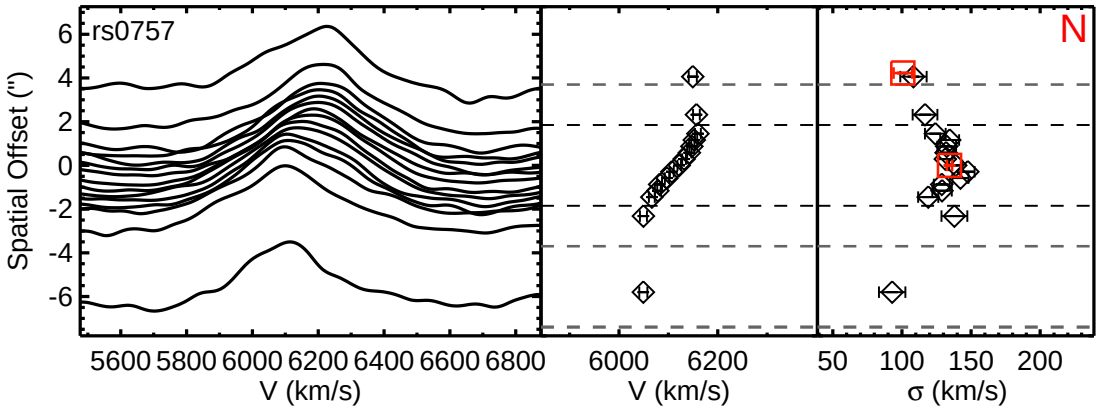

Figure 4.17 Cross-correlation profiles plus rotation/velocity dispersion measurements (cont.).

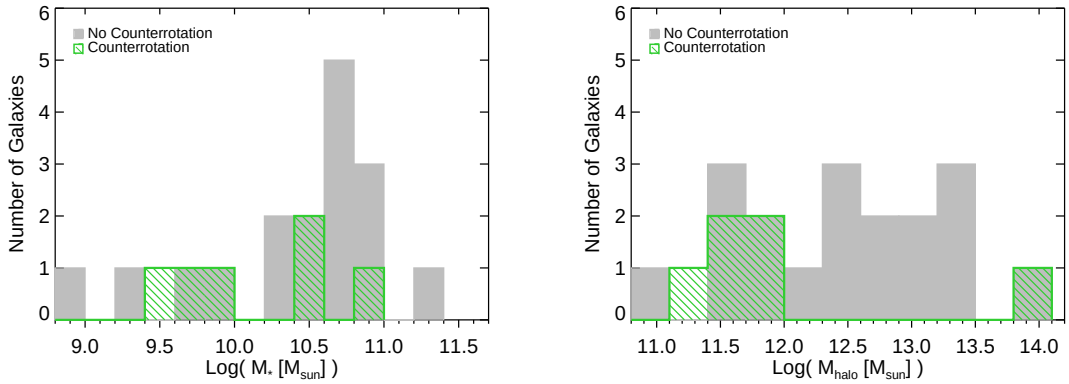

Figure 4.18 Distribution of counterrotating and non-counterrotating RESOLVE S0s in stellar mass (left panel) and group halo mass parameters (right panel). No statistically significant difference is found between the mass or environment distributions of counterrotators versus non counterrotators.

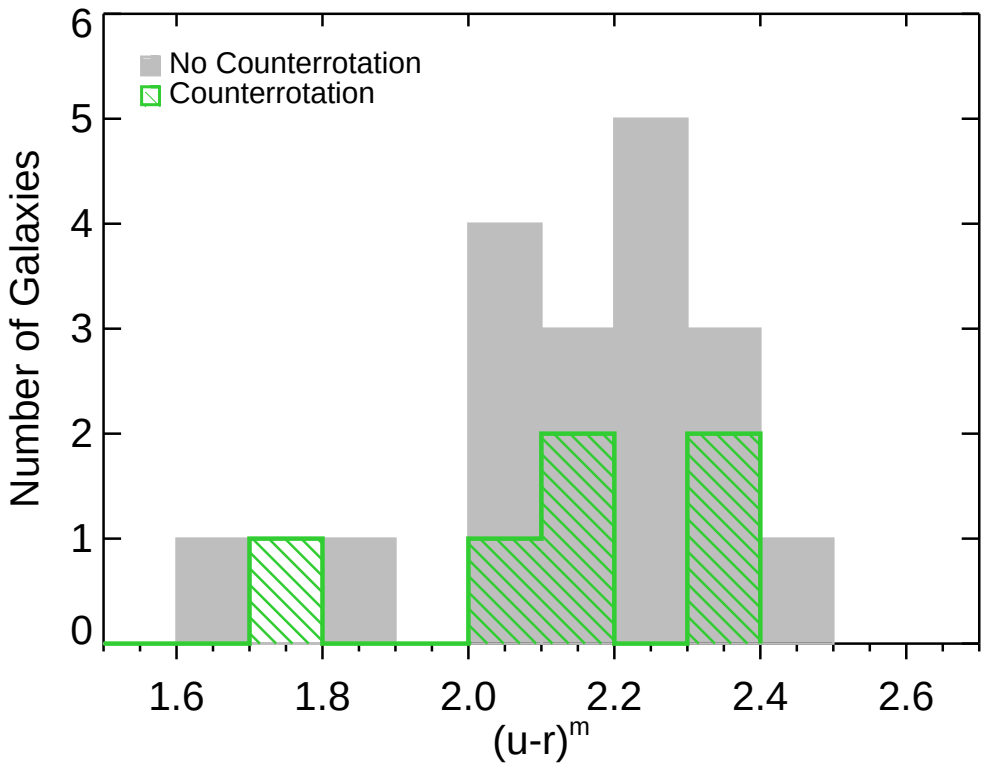

Figure 4.19 Distribution of counterrotating and non-counterrotating RESOLVE S0s in model color. No statistically significant difference is found between the color distributions of counterrotators versus non counterrotators.

we find no statistically significant difference, as judged using the Kolmogorov-Smirnov test, in the masses, environments, or colors of counterrotating galaxies compared to those that are not strongly counterrotating (see Figs. 4.18 and 4.19). As two of our counterrotators lie on the relatively high mass red sequence in color vs. stellar mass, a regime where star formation is typically quenched, it is possible that these counterrotating systems represent the end stage of a merger rather than true disk regrowth. However, nearly all of our counterrotators are found in low group halo mass environments where the availability of abundant gas appears connected to disk growth (see Chapter 3), potentially implying a gas accretion and subsequent in situ star formation origin for these objects. Although this environment distribution is suggestive, our counterrotators do not display a statistically significant preference for low group halo mass environments as a population. Similarly, Bettoni et al. (2001) find no significant difference between the environment distribution of a heterogeneous literature sample of 29 known stellar-stellar counterrotators of all morphological types and a non-counterrotating comparison sample, although they note that if any weak trend exists it is for *gas*-stellar counterrotators to occupy relatively low density environments.

4.4 Conclusions

In this work, we have analyzed deep stellar kinematic observations of a broad sample of RESOLVE S0 galaxies to look for signatures of stellar disk regrowth in the form of spatially extended secondary stellar disks. We find 6 strong stellar-stellar counterrotators in our sample, which translates to a $25^{+12}_{-9}\%$ counterrotation frequency. Compared to galaxies without strong counterrotation, we find that our stellar-stellar counterrotators display no statistically significant preference for particular stellar mass, environment, or color regimes.

Completing the remainder of the data reduction for our target galaxies is clearly the next step in improving the sample statistics, and additional observations may also be sought in the future to improve the quality of some of the data in hand and bring our sample closer to its originally intended size. To obtain better constraints on the demographics of stellar disk regrowth through secondary disk detection, another important topic for future investigation is quantifying the limits of our ability to detect secondary disk components with a variety of masses, orientations, and characteristic velocities. Some of our sample galaxies may potentially host secondary stellar disks that remain undetected with the "strong counterrotation" metric considered here. Thus, an analysis that uses model galaxies with diverse secondary disk configurations to generate synthetic data matching our observational configurations is necessary to fully probe the parameter space of situations in which

secondary disk signatures may elude kinematic detection. Furthermore, such an analysis will allow us to understand the extent to which secondary disk structures can be detected in standard lower S/N RESOLVE survey data products, potentially allowing the investigation of both gas-stellar and stellar-stellar counterrotation incidence in a much larger sample containing all galaxy morphological types.

We acknowledge the use of both UNC-guaranteed and NOAO-awarded observing time allocations in this work (NOAO programs 2010A-0110, 2010B-0594, and 2011A-0164). We thank C. Maraston for her guidance in the use of the Maraston & Strömbäck (2011) stellar population models. We also thank all contributors to the development and testing of the RESOLVE survey data reduction pipeline and RESOLVE team members that have participated in the reduction of deep S0 data for this project (E. Snyder and D. Rosenberg). Based on observations obtained at the Southern Astrophysical Research (SOAR) telescope, which is a joint project of the Ministério da Ciência, Tecnologia, e Inovação (MCTI) da República Federativa do Brasil, the U.S. National Optical Astronomy Observatory (NOAO), the University of North Carolina at Chapel Hill (UNC), and Michigan State University (MSU).

Table 4.1 RESOLVE Deep S0 Spectroscopy Sample

Name	$\log M_*/M_\odot$	$\log M_{halo}/M_\odot$	$(u-r)^m$	Obs. Dates	Setup	FWHM A	Exp. Time	CR Flag
rs1083	9.0	11.1	1.8	2011-04-30*/2011-05-03*/2011-05-29*	2100 l/mm + 1.03" LS	1.02	2.0 hr	N
rf0130	10.5	13.3	2.1	2010-09-07/2010-09-08	1200 l/mm + 0.46" LS	1.23	2.0 hr	N
rf0016	10.8	12.4	2.3	2010-09-07	1200 l/mm + 0.46" LS	0.99	1.3 hr	N
rf0327	10.9	12.3	2.2	2010-09-07/2010-09-08	1200 l/mm + 0.46" LS	1.19	2.0 hr	N
rs0205	11.0	12.6	2.2	2011-05-01*	2100 l/mm + 1.68" LS	1.21	1.0 hr	N
rf0446	10.3	13.1	2.2	2010-10-07/2010-10-08	2100 l/mm + 1.03" LS	1.25	2.0 hr	N
rf0402	10.5	13.3	2.1	2010-10-05/2010-10-06/2010-10-07	2100 l/mm + 1.03" LS	1.14	2.0 hr	N
rs0250	10.4	11.7	2.2	2011-04-04/2011-04-03	2100 l/mm + 1.68" LS	1.22	2.0 hr	C
rs0629	10.9	13.8	2.3	2011-04-30*	2100 l/mm + 1.68" LS	1.20	1.0 hr	C
rs1201	10.8	12.6	2.5	2011-03-05	2100 l/mm + 1.68" LS	1.23	1.0 hr	N
rs1300	10.6	11.9	2.3	2011-05-03*/2011-04-04/2011-04-30*	2100 l/mm + 1.68" LS	1.24	2.3 hr	C
rf0512	9.8	11.6	2.2	2010-10-07/2010-10-08	2100 l/mm + 1.03" LS	1.30	1.7 hr	U
rs1282	10.2	11.6	2.1	2011-04-03/2011-03-05	2100 l/mm + 1.68" LS	1.24	2.0 hr	N
rf0127	9.6	11.8	1.7	2010-10-05	2100 l/mm + 1.03" LS	1.12	0.7 hr	C
rs1079	9.6	11.2	2.0	2011-04-03/2011-04-04	2100 l/mm + 1.68" LS	1.22	2.0 hr	C
rs0328	8.9	11.1	1.4	2011-03-05/2011-03-04	2100 l/mm + 1.03" LS	1.06	2.0 hr	U
rs0104	9.5	11.2	1.7	2011-04-04/2011-04-30*/2011-05-03*	2100 l/mm + 1.03" LS	1.00	1.3 hr	U
rs0005	9.9	11.4	2.2	2011-03-05/2011-04-03	2100 l/mm + 1.03" LS	1.04	2.0 hr	U
rs0636	9.7	12.5	2.0	2012-04-20	2100 l/mm + 1.0" IS	1.02	1.7 hr	N
rs0920	8.8	11.5	1.6	2011-05-29*/2011-05-30*	2100 l/mm + 1.03" LS	1.04	1.7 hr	N
rs1279	10.0	11.4	2.2	2011-04-30*/2011-05-02	2100 l/mm + 1.68" LS	1.21	1.3 hr	N
rs1081	9.1	12.6	1.8	2011-05-02/2011-05-03*	2100 l/mm + 1.03" LS	0.98	2.3 hr	U
rs0014	10.0	11.5	2.1	2011-05-01*/2011-05-02	2100 l/mm + 1.68" LS	1.20	2.0 hr	C
rs0615	9.2	12.9	2.0	2011-05-03*	2100 l/mm + 1.03" LS	0.97	1.0 hr	N
rs1228	9.3	12.9	2.1	2011-05-01*/2011-05-02/2011-05-03*/2011-05-30*	2100 l/mm + 1.03" LS	1.01	2.0 hr	U
rf0052	9.2	12.5	2.0	2010-11-04/2010-11-05	2100 l/mm + 0.84" LS	0.98	2.0 hr	U
rf0254	10.7	11.9	2.3	2010-10-06/2010-10-08	2100 l/mm + 1.03" LS	1.15	2.0 hr	N
rf0346	11.2	13.4	2.2	2010-10-05/2010-10-07	2100 l/mm + 1.03" LS	1.24	2.0 hr	N
rs0080	10.8	12.0	2.3	2011-04-03/2011-04-04	2100 l/mm + 1.68" LS	1.23	0.7 hr	N
rs0642	10.7	13.8	2.3	2011-04-03/2011-04-04/2011-05-01*	2100 l/mm + 1.68" LS	1.26	2.0 hr	N
rs0757	10.8	12.7	2.3	2011-05-03*	2100 l/mm + 1.68" LS	1.21	1.0 hr	N
rf0094	10.9	13.2	2.1	2011-08-28	2100 l/mm + 1.35" LS	1.31	1.3 hr	NR
rf0138	11.0	13.3	2.4	2011-10-26	2100 l/mm + 1.68" LS	1.60	1.3 hr	NR
rs0612	10.9	12.9	2.1	2009-02-27	600 l/mm + 1.03" LS	4.31	2.0 hr	NR
rs0688	11.2	12.9	2.3	2010-03-13	1200 l/mm + 1.03" LS	2.66	3.0 hr	NR
rs0992	10.9	12.4	2.3	2009-04-19	600 l/mm + 1.03" LS	4.67	2.0 hr	NR
rf0423	10.9	12.3	2.1	2010-09-07/2010-10-08/2011-10-26	1200 l/mm + 0.46" LS	1.21	2.0 hr	NR
rs0113	10.3	11.5	2.2	2009-03-27	600 l/mm + 1.03" LS	4.50	2.0 hr	NR
rs0155	10.5	12.1	2.1	2009-03-29	600 l/mm + 1.03" LS	4.56	2.0 hr	NR
rs0253	10.5	11.7	2.3	2009-03-29	600 l/mm + 1.03" LS	4.56	2.0 hr	NR
rs0282	9.7	11.4	1.7	2010-05-06/2010-05-07	1200 l/mm + 1.03" LS	2.47	3.0 hr	NR
rs0595	10.1	11.8	2.2	2009-03-28	600 l/mm + 1.03" LS	4.54	2.0 hr	NR
rs0784	10.5	11.8	2.3	2010-03-12	1200 l/mm + 1.03" LS	2.67	3.0 hr	NR
rs0951	10.3	11.5	2.2	2010-04-10/2010-04-11	1200 l/mm + 1.03" LS	2.53	3.0 hr	NR
rs1046	10.4	12.0	2.0	2009-03-27	600 l/mm + 1.03" LS	4.50	2.0 hr	NR
rs1190	9.9	13.6	1.9	2012-04-19	2100 l/mm + 1.0" IS	1.05	1.0 hr	NR
rs1196	10.1	11.4	2.3	2010-04-20/2010-05-07	1200 l/mm + 1.03" LS	2.44	3.0 hr	NR
rf0234	9.3	12.3	1.9	2011-08-28/2011-10-26	2100 l/mm + 1.35" LS	1.28	1.7 hr	NR
rs1148	9.3	13.6	1.9	2011-05-01*	2100 l/mm + 1.03" LS	1.21	0.7 hr	U
rf0274	9.6	12.1	2.0	2010-10-08/2010-11-09/2011-10-26	2100 l/mm + 1.03" LS	1.16	1.3 hr	NR
rs1292	10.0	11.4	2.0	2010-07-08	1200 l/mm + 1.03" LS	2.52	2.0 hr	NR
rf0413	8.6	11.1	1.4	2010-10-07/2010-10-08	2100 l/mm + 1.03" LS	1.11	2.0 hr	U
rf0455	9.3	11.1	1.7	2010-11-04/2010-11-09/2011-08-28	2100 l/mm + 0.84" LS	1.17	0.7 hr	NR
rf0096	9.6	11.8	2.3	2010-11-04/2010-11-05	2100 l/mm + 0.84" LS	0.95	0.7 hr	U
rs0131	10.8	12.0	2.3	2010-03-12/2010-03-13	1200 l/mm + 1.03" LS	2.56	3.0 hr	NR
rs0517	9.5	11.3	1.6	2012-04-19	2100 l/mm + 1.0" IS	1.02	1.3 hr	NR
rs0682	10.1	11.9	2.3	2012-03-25/2012-03-26	2100 l/mm + 1.0" IS	1.01	1.7 hr	NR
rs0695	9.7	13.8	2.3	2012-04-19	2100 l/mm + 1.0" IS	1.02	1.7 hr	NR
rs1174	10.0	13.6	2.3	2012-03-25/2012-03-26	2100 l/mm + 1.0" IS	1.01	1.7 hr	NR

Summary of RESOLVE deep S0 spectroscopy sample properties and observations. *Observing nights on which variable stray light was present in Goodman Spectrograph data, leaving low-level stray light residuals even after our pseudo-dark subtraction procedure. CR Flag column indicates stellar-stellar counterrotation status, where "C" indicates a counterrotating galaxy, "N" indicates a non-counterrotating galaxy, "U" indicates a galaxy with reduced data but uncertain counterrotation status due to insufficient data quality, and "NR" indicates a galaxy that currently lacks final reduced data products enabling counterrotation analysis. Targets rs1148, rf0413, and rf0096 currently have reduced data of such low quality that we refrain from including them in the counterrotation identification plots shown here.

CHAPTER 5: CONCLUSIONS AND FUTURE WORK

The results from this work provide observational support for the predicted disk regrowth process. We find that recent disk growth in the form of UV-detected disks is surprisingly common in low galaxy mass and low group halo mass E/S0 galaxies. Such UV disks represent relatively significant growth ($\gtrsim$10% by mass) and are also associated with large gas reservoirs that may continue to fuel star formation. The low group halo mass regime below $\sim 10^{11.5} M_{\odot}$ is associated with both frequent gas and disk building activity, raising the possibility that such activity is linked to a low halo mass threshold for effective gas accretion.

Two of the major methodological themes of this work are developing quantitative/automated analysis methods and implementing strategies to mitigate systematics that may arise from automated data processing and selection methods. Such considerations are of particular importance as our field enters the era of big data, with increasingly large data streams mandating automated approaches to data analysis. Only with careful attention to the optimization of such methods and their possible systematics can we take full advantage of the opportunity to study ever larger statistical samples and to develop a detailed accounting of the properties of galaxy populations that can confirm or confront existing galaxy evolution theories.

In my future work, I intend to continue investigation of the link between gas/stellar disk growth and gas accretion processes, focusing on observational tests of predicted gas accretion into galaxies originating from large-scale filamentary structures. Testing this scenario requires the development of new metrics of large-scale, filamentary environment for application in large galaxy samples like ECO. In part due to the difficulty of identifying complicated filamentary structures in observed galaxy distributions, the degree to which galaxy properties are shaped by their positions within large-scale filamentary structure is an aspect of galaxy evolution that has not been well studied to date. One potential approach to identifying filaments in observed catalogs is to modify a method that performs well in identifying smaller-scale observed structures, e.g., the friends-of-friends algorithm of Berlind et al. (2006), and quantify the degree of filamentarity of structures with Shapefinder functions, measures of shape constructed from Minkowski functionals (e.g., Sahni et al. 1998). An

alternative approach is to focus not on identifying individual filaments but on quantifying the filamentarity of particular galaxy populations. Comparing the spatial distributions of galaxies that are gas-dominated or disk-building with mock galaxy samples randomly distributed in space according to only their known local environment preferences (as calibrated from Chapter 3) could allow determination of whether or not such populations have more filamentary distributions than are expected from only local environment trends and chance alignments.

The newly created ECO catalog enables a multitude of other projects relating to the effects of environment on galaxy evolutionary processes, both as a standalone sample and as a source for the full environmental context surrounding RESOLVE. I am already involved with several ongoing collaborations using ECO. These projects include the dissertation work of K. Eckert focused on determining conditional galaxy mass functions and relating them to group halo mass, the dissertation work of D. Stark focused on investigating the connection between gas accretion processes and large-scale environment, and the senior thesis work of A. Baker focused on developing a new dynamical group halo mass estimator. In general, I expect to continue work on the relationship between galaxy evolutionary processes and environment with S. Driver and other members of the GAMA survey team while at the University of Western Australia.

I also plan to follow up on a project for which new *GALEX* UV imaging data on a unique bar and double ring galaxy that may represent a short-lived phase in the morphological transformation process was obtained (program GI5-042, PI A. Moffett). I co-mentored undergraduate student D. Bradley in a project focused on age dating features in this galaxy and identifying analogs in large galaxy samples. This project yielded intriguing results on the rarity and interaction status of such objects, motivating further investigation. A public outreach add-on grant to the *GALEX* program also allowed us to collaborate with the Renaissance Computing Initiative and Morehead Planetarium and Science Center to create an interactive educational display outside the UNC Remote Observing Center that communicates multi-wavelength astronomy and galaxy evolution concepts as well as results from our disk growth research.

Finally, I intend to continue work on the ongoing RESOLVE S0 secondary disk project, completing the reduction and analysis of data already in hand as well as creating synthetic galaxy observations to fully quantify the degree to which secondary stellar disks are detectable in our deep longslit data. Another goal is to use the S0 counterrotation data to separate and age-date the multiple disk stellar populations in counterrotators. I co-mentored undergraduate student C. Bradfield in a project focused on performing such a decomposition for a test case, which will require further

follow up to apply to larger galaxy samples.

APPENDIX A: RESOLVE MORPHOLOGY CLASSIFICATION

RESOLVE survey galaxies have been morphologically classified by eye. This effort involved a team of RESOLVE survey classifiers (S. Kannappan, M. Norris, A. Moffett, K. Eckert, D. Stark, J. Burchett, K. Hall, A. Baker) who were first trained by classifying a set of galaxies with known types. This training set consists of a sub-selection of the Nearby Field Galaxy Survey (NFGS, Jansen et al. 2000a,b) that was chosen to mimic the overall stellar mass distribution of the RESOLVE survey galaxies. The NFGS galaxies were classified using a simplified de Vaucoleurs system. For training purposes, the original NFGS typing images were blurred to mimic the effective resolution that would be seen if these galaxies were placed at the far edge of the RESOLVE volume.

Monochromatic SDSS g-band images were used for the classifications and displayed through a custom interface, allowing multiple image scaling and zoom levels to be viewed at once. The classifiers were each paired with a partner such that every RESOLVE galaxy would be independently classified twice, and a subset of representative training set galaxies were re-injected randomly into the classification lists to check for systematic typing offsets and classification drift. In addition to morphological classification, classifiers were asked to identify bars, rings, potential interactions, and galaxies for which the inclinations made classification decisions difficult.

After each set of galaxies was classified, the results from paired classifiers were compared, and a list of "discrepant" classifications was generated. We chose to define classifications as discrepant if they disagreed by two full numerical morphological types or more in general or if they disagreed by a tighter one-type limit in the important early-late type division regime or by one and a half types in the Sa/b-Sc regime. This selection led to lists of ∼70-120 galaxies for which each classification pair reconciled their classifications. Images for these galaxies along with the classifications previously entered by each classifier were examined and discussed by the paired classifiers, resulting in a single reconciled type for each discrepant galaxy.[1] If the two classifications for a given galaxy were not considered discrepant, the final morphological type was assigned by averaging the two assigned numerical types. Analysis of the small subset of training sample re-classifications performed alongside the RESOLVE classifications yields no evidence for systematic offsets with respect to the reference types (typical offsets are within a single numerical type) nor for significant classification drift over time (see Figs. A.1 and A.2). The apparent tendency towards classifying training set galaxies in the Sa-Sb range as later types, as seen in Fig. A.1, appears to result from a small number of Sa-Sb

[1]Since some RESOLVE galaxies are sufficiently small that typical SDSS g-band resolutions do not allow detailed structure, or even bulge vs. disk structures to be confidently distinguished, classifiers were also asked to note when their classification decisions were adversely affected by insufficient resolution with a '?' flag.

training set galaxies that legitimately resemble later-type spirals.

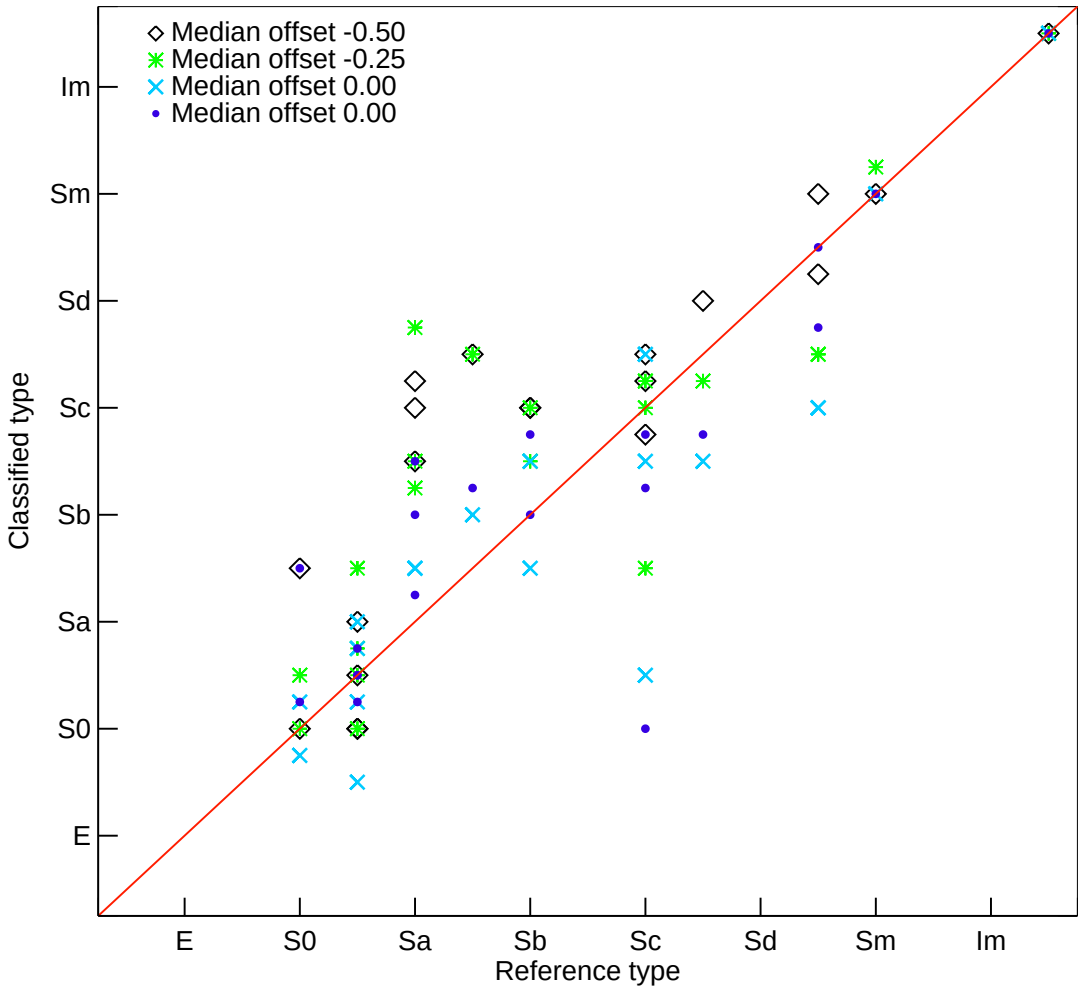

Figure A.1 Comparison of training set galaxy classifications from re-injection into the RESOLVE classification lists with NFGS reference types. Individual determinations from each classifier pair are marked with different symbols, and their median offsets from the reference types are indicated in the legend. The red line marks a one-to-one correspondence.

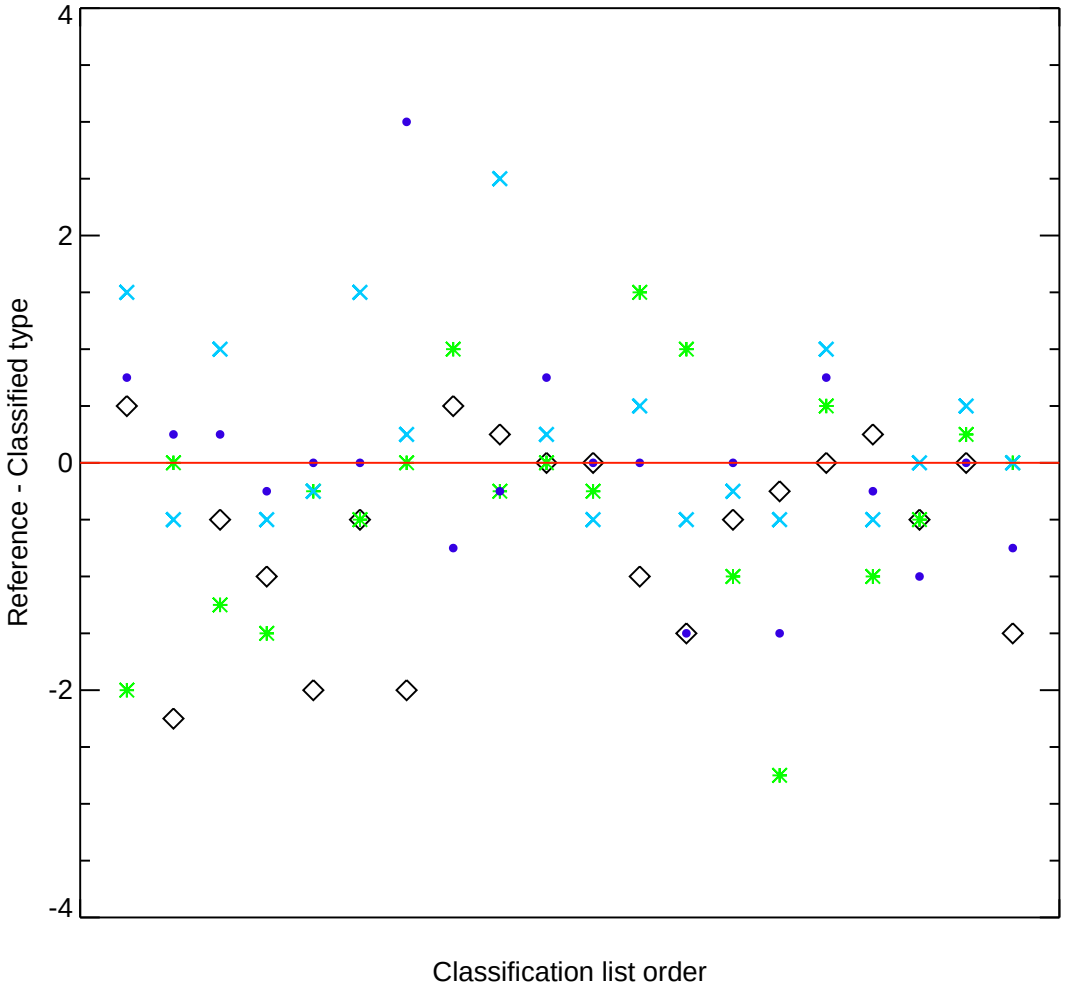

Figure A.2 Illustration of the lack of systematic drift in the RESOLVE galaxy classifications over time. The differences between NFGS reference types and classifications from their re-injection into the RESOLVE classification lists are shown as a function of classification order. Individual determinations from each classifier pair are marked with different symbols, and the red line marks zero difference.

BIBLIOGRAPHY

Abazajian, K., Adelman-McCarthy, J. K., Agüeros, M. A., et al. 2004, AJ, 128, 502

Abazajian, K. N., Adelman-McCarthy, J. K., Agüeros, M. A., et al. 2009, ApJS, 182, 543

Adelman-McCarthy, J. K., Agüeros, M. A., Allam, S. S., et al. 2006, ApJS, 162, 38

—. 2008, ApJS, 175, 297

Aihara, H., Allende Prieto, C., An, D., et al. 2011, ApJS, 193, 29

Bamford, S. P., Nichol, R. C., Baldry, I. K., et al. 2009, MNRAS, 393, 1324

Barnes, J. E. 2002, MNRAS, 333, 481

Basilakos, S., Plionis, M., Kovač, K., & Voglis, N. 2007, MNRAS, 378, 301

Baugh, C. M., Cole, S., & Frenk, C. S. 1996, MNRAS, 283, 1361

Bender, R. 1988, A&A, 202, L5

Berlind, A. A., & Weinberg, D. H. 2002, ApJ, 575, 587

Berlind, A. A., Frieman, J., Weinberg, D. H., et al. 2006, ApJS, 167, 1

Bertin, E., & Arnouts, S. 1996, A&ASS, 117, 393

Bettoni, D., Galletta, G., & Prada, F. 2001, A&A, 374, 83

Birnboim, Y., & Dekel, A. 2003, MNRAS, 345, 349

Blanton, M. R., & Berlind, A. A. 2007, ApJ, 664, 791

Blanton, M. R., Eisenstein, D., Hogg, D. W., Schlegel, D. J., & Brinkmann, J. 2005, ApJ, 629, 143

Blanton, M. R., Hogg, D. W., Bahcall, N. A., et al. 2003, ApJ, 594, 186

Boissier, S., Gil de Paz, A., Boselli, A., et al. 2008, ApJ, 681, 244

Boselli, A., & Gavazzi, G. 2006, PASP, 118, 517

Bower, R. G., & Balogh, M. L. 2004, Clusters of Galaxies: Probes of Cosmological Structure and Galaxy Evolution, 325

Bravo-Alfaro, H., Cayatte, V., van Gorkom, J. H., & Balkowski, C. 2000, AJ, 119, 580

Bruzual, G., & Charlot, S. 2003, MNRAS, 344, 1000

Bush, S. J., Cox, T. J., Hernquist, L., Thilker, D., & Younger, J. D. 2008, ApJL, 683, L13

Calvi, R., Poggianti, B. M., Fasano, G., & Vulcani, B. 2012, MNRAS, 419, L14

Cameron, E. 2011, PASA, 28, 128

Cappellari, M., & Emsellem, E. 2004, PASP, 116, 138

Cardelli, J. A., Clayton, G. C., & Mathis, J. S. 1989, ApJ, 345, 245

Cayatte, V., Kotanyi, C., Balkowski, C., & van Gorkom, J. H. 1994, AJ, 107, 1003

Chabrier, G. 2003, PASP, 115, 763

Christlein, D., & Zabludoff, A. I. 2005, ApJ, 621, 201

Clemens, J. C., Crain, J. A., & Anderson, R. 2004, in Society of Photo-Optical Instrumentation Engineers (SPIE) Conference Series, Vol. 5492, Society of Photo-Optical Instrumentation Engineers (SPIE) Conference Series, ed. A. F. M. Moorwood & M. Iye, 331–340

Colless, M., Dalton, G., Maddox, S., et al. 2001, MNRAS, 328, 1039

Cortese, L., Catinella, B., Boissier, S., Boselli, A., & Heinis, S. 2011, MNRAS, 415, 1797

Cortese, L., & Hughes, T. M. 2009, MNRAS, 400, 1225

Couch, W. J., Barger, A. J., Smail, I., Ellis, R. S., & Sharples, R. M. 1998, ApJ, 497, 188

Crocker, A. F., Jeong, H., Komugi, S., et al. 2009, MNRAS, 393, 1255

Davies, R. D., & Lewis, B. M. 1973, MNRAS, 165, 231

Davies, R. L., Efstathiou, G., Fall, S. M., Illingworth, G., & Schechter, P. L. 1983, ApJ, 266, 41

Davis, M., & Geller, M. J. 1976, ApJ, 208, 13

Dekel, A., & Birnboim, Y. 2006, MNRAS, 368, 2

Donovan, J. L., Serra, P., van Gorkom, J. H., et al. 2009, AJ, 137, 5037

Dressler, A. 1980, ApJ, 236, 351

Dressler, A., Smail, I., Poggianti, B. M., et al. 1999, ApJS, 122, 51

Drinkwater, M. J., Gregg, M. D., Holman, B. A., & Brown, M. J. I. 2001, MNRAS, 326, 1076

Driver, S. P., Hill, D. T., Kelvin, L. S., et al. 2011, MNRAS, 413, 971

Efron, B. 1983, Journal of the Americal Statistical Association, 78, 316

Eggen, O. J., Lynden-Bell, D., & Sandage, A. R. 1962, ApJ, 136, 748

Emsellem, E., Cappellari, M., Krajnović, D., et al. 2007, MNRAS, 379, 401

Falco, E. E., Kurtz, M. J., Geller, M. J., et al. 1999, PASP, 111, 438

Filippenko, A. V. 1982, PASP, 94, 715

Franx, M., & Illingworth, G. D. 1988, ApJL, 327, L55

Galletta, G. 1996, in Astronomical Society of the Pacific Conference Series, Vol. 91, IAU Colloq. 157: Barred Galaxies, ed. R. Buta, D. A. Crocker, & B. G. Elmegreen, 429

Gavazzi, G. 1987, ApJ, 320, 96

Gil de Paz, A., Madore, B. F., Boissier, S., et al. 2005, ApJL, 627, L29

Giovanelli, R., & Haynes, M. P. 1983, AJ, 88, 881

—. 1985, ApJ, 292, 404

Goto, T., Yamauchi, C., Fujita, Y., et al. 2003, MNRAS, 346, 601

Governato, F., Willman, B., Mayer, L., et al. 2007, MNRAS, 374, 1479

Grogin, N. A., & Geller, M. J. 1999, AJ, 118, 2561

Gunn, J. E., & Gott, III, J. R. 1972, ApJ, 176, 1

Haynes, M. P., & Giovanelli, R. 1984, AJ, 89, 758

Haynes, M. P., Giovanelli, R., & Chincarini, G. L. 1984, ARA&A, 22, 445

Haynes, M. P., Giovanelli, R., Martin, A. M., et al. 2011, AJ, 142, 170

Helsdon, S. F., & Ponman, T. J. 2003, MNRAS, 339, L29

Hibbard, J. E., & Mihos, J. C. 1995, AJ, 110, 140

Hogg, D. W., Blanton, M. R., Eisenstein, D. J., et al. 2003, ApJL, 585, L5

Hopkins, P. F., Cox, T. J., Younger, J. D., & Hernquist, L. 2009, ApJ, 691, 1168

Hoyle, B., Masters, K. L., Nichol, R. C., Jimenez, R., & Bamford, S. P. 2012, MNRAS, 423, 3478

Hubble, E., & Humason, M. L. 1931, ApJ, 74, 43

Huchra, J., Davis, M., Latham, D., & Tonry, J. 1983, ApJS, 52, 89

Jansen, R. A., Fabricant, D., Franx, M., & Caldwell, N. 2000a, ApJS, 126, 331

Jansen, R. A., Franx, M., Fabricant, D., & Caldwell, N. 2000b, ApJS, 126, 271

Jarrett, T. H., Chester, T., Cutri, R., et al. 2000, AJ, 119, 2498

Jedrzejewski, R., & Schechter, P. L. 1988, ApJL, 330, L87

Jones, D. H., Read, M. A., Saunders, W., et al. 2009, MNRAS, 399, 683

Kannappan, S. J. 2001, PhD thesis, HARVARD UNIVERSITY

—. 2004, ApJL, 611, L89

Kannappan, S. J., & Fabricant, D. G. 2001, AJ, 121, 140

Kannappan, S. J., & Gawiser, E. 2007, ApJL, 657, L5

Kannappan, S. J., Guie, J. M., & Baker, A. J. 2009, AJ, 138, 579

Kannappan, S. J., & Wei, L. H. 2008, in American Institute of Physics Conference Series, Vol. 1035, The Evolution of Galaxies Through the Neutral Hydrogen Window, ed. R. Minchin & E. Momjian, 163–168

Kannappan, S. J., Stark, D. V., Eckert, K. D., et al. 2013, ArXiv e-prints, arXiv:1308.3292

Kauffmann, G., White, S. D. M., Heckman, T. M., et al. 2004, MNRAS, 353, 713

Kauffmann, G., Heckman, T. M., White, S. D. M., et al. 2003, MNRAS, 341, 33

Kauffmann, G., Heckman, T. M., Budavári, T., et al. 2007, ApJS, 173, 357

Kawata, D., & Mulchaey, J. S. 2008, ApJL, 672, L103

Kennicutt, Jr., R. C. 1983, AJ, 88, 483

Kereš, D., Katz, N., Fardal, M., Davé, R., & Weinberg, D. H. 2009, MNRAS, 395, 160

Kereš, D., Katz, N., Weinberg, D. H., & Davé, R. 2005, MNRAS, 363, 2

Koopmann, R. A., & Kenney, J. D. P. 1998, ApJL, 497, L75

Kregel, M., van der Kruit, P. C., & Freeman, K. C. 2004, MNRAS, 351, 1247

Kroupa, P. 2001, MNRAS, 322, 231

Kuijken, K., Fisher, D., & Merrifield, M. R. 1996, MNRAS, 283, 543

Kurtz, M. J., Mink, D. J., Wyatt, W. F., et al. 1992, in Astronomical Society of the Pacific Conference Series, Vol. 25, Astronomical Data Analysis Software and Systems I, ed. D. M. Worrall, C. Biemesderfer, & J. Barnes, 432

Lacey, C., & Cole, S. 1993, MNRAS, 262, 627

Larson, R. B. 1969, MNRAS, 145, 405

Lemonias, J. J., Schiminovich, D., Thilker, D., et al. 2011, ApJ, 733, 74

Leroy, A. K., Walter, F., Brinks, E., et al. 2008, AJ, 136, 2782

Lewis, I., Balogh, M., De Propris, R., et al. 2002, MNRAS, 334, 673

Li, C., Kauffmann, G., Fu, J., et al. 2012, MNRAS, 424, 1471

Lintott, C., Schawinski, K., Bamford, S., et al. 2011, MNRAS, 410, 166

Maia, M. A. G., & da Costa, L. N. 1990, ApJ, 352, 457

Maraston, C., & Strömbäck, G. 2011, MNRAS, 418, 2785

Marino, A., Rampazzo, R., Bianchi, L., et al. 2011, MNRAS, 411, 311

Martin, A. M., Giovanelli, R., Haynes, M. P., & Guzzo, L. 2012, ApJ, 750, 38

Meyer, M. J., Zwaan, M. A., Webster, R. L., Brown, M. J. I., & Staveley-Smith, L. 2007, ApJ, 654, 702

Moffett, A. J., Kannappan, S. J., Baker, A. J., & Laine, S. 2012, ApJ, 745, 34

Moffett, A. J., Kannappan, S. J., Laine, S., et al. 2010, in Astronomical Society of the Pacific Conference Series, Vol. 423, Galaxy Wars: Stellar Populations and Star Formation in Interacting Galaxies, ed. B. Smith, J. Higdon, S. Higdon, & N. Bastian, 346

Moore, B., Lake, G., & Katz, N. 1998, ApJ, 495, 139

Morganti, R., de Zeeuw, P. T., Oosterloo, T. A., et al. 2006, MNRAS, 371, 157

Morrissey, P., Conrow, T., Barlow, T. A., et al. 2007, ApJS, 173, 682

Naab, T., Jesseit, R., & Burkert, A. 2006, MNRAS, 372, 839

Nair, P. B., & Abraham, R. G. 2010, ApJS, 186, 427

Nelson, D., Vogelsberger, M., Genel, S., et al. 2013, MNRAS, 429, 3353

O'Connell, R. W. 1999, ARA&A, 37, 603

Oosterloo, T., Morganti, R., Crocker, A., et al. 2010, MNRAS, 409, 500

Oosterloo, T. A., Morganti, R., Sadler, E. M., van der Hulst, T., & Serra, P. 2007, A&A, 465, 787

Papastergis, E., Martin, A. M., Giovanelli, R., & Haynes, M. P. 2011, ApJ, 739, 38

Paturel, G., Petit, C., Prugniel, P., et al. 2003, A&A, 412, 45

Poggianti, B. M., Smail, I., Dressler, A., et al. 1999, ApJ, 518, 576

Poggianti, B. M., Fasano, G., Bettoni, D., et al. 2009, ApJL, 697, L137

Postman, M., & Geller, M. J. 1984, ApJ, 281, 95

Prugniel, P., Soubiran, C., Koleva, M., & Le Borgne, D. 2007, VizieR Online Data Catalog, 3251, 0

Quintero, A. D., Berlind, A. A., Blanton, M., & Hogg, D. W. 2006, ArXiv Astrophysics e-prints, arXiv:astro-ph/0611361

Sage, L. J., & Welch, G. A. 2006, ApJ, 644, 850

Sahni, V., Sathyaprakash, B. S., & Shandarin, S. F. 1998, ApJL, 495, L5

Salim, S., & Rich, R. M. 2010, ApJL, 714, L290

Salpeter, E. E. 1955, ApJ, 121, 161

Schawinski, K., Lintott, C., Thomas, D., et al. 2009, MNRAS, 396, 818

Schlegel, D. J., Finkbeiner, D. P., & Davis, M. 1998, ApJ, 500, 525

Scoccimarro, R. 1998, MNRAS, 299, 1097

Shimasaku, K., Fukugita, M., Doi, M., et al. 2001, AJ, 122, 1238

Simha, V., Weinberg, D. H., Davé, R., et al. 2009, MNRAS, 399, 650

Skibba, R. A., Bamford, S. P., Nichol, R. C., et al. 2009, MNRAS, 399, 966

Skrutskie, M. F., Cutri, R. M., Stiening, R., et al. 2006, AJ, 131, 1163

Solanes, J. M., Manrique, A., García-Gómez, C., et al. 2001, ApJ, 548, 97

Springel, V. 2005, MNRAS, 364, 1105

Stark, D. V., Kannappan, S. J., Wei, L. H., et al. 2013, ApJ, 769, 82

Steinmetz, M., & Navarro, J. F. 2002, , 7, 155

Strateva, I., Ivezić, Ž., Knapp, G. R., et al. 2001, AJ, 122, 1861

Tegmark, M., Blanton, M. R., Strauss, M. A., et al. 2004, ApJ, 606, 702

Thilker, D. A., Bianchi, L., Boissier, S., et al. 2005, ApJL, 619, L79

Thilker, D. A., Bianchi, L., Meurer, G., et al. 2007, ApJS, 173, 538

Thilker, D. A., Bianchi, L., Schiminovich, D., et al. 2010, ApJL, 714, L171

Thomas, D., Maraston, C., Schawinski, K., Sarzi, M., & Silk, J. 2010, MNRAS, 404, 1775

Toomre, A. 1977, in Evolution of Galaxies and Stellar Populations, ed. B. M. Tinsley & R. B. G. Larson, D. Campbell, 401

Toomre, A., & Toomre, J. 1972, ApJ, 178, 623

Tran, K.-V. H., Simard, L., Zabludoff, A. I., & Mulchaey, J. S. 2001, ApJ, 549, 172

Tully, R. B., & Fisher, J. R. 1977, A&A, 54, 661

van den Bergh, S. 1976, ApJ, 206, 883

van Dokkum, P. G. 2001, PASP, 113, 1420

van Gorkom, J. H. 2004, Clusters of Galaxies: Probes of Cosmological Structure and Galaxy Evolution, 305

Warmels, R. H. 1988, A&ASS, 72, 427

Wei, L. H., Kannappan, S. J., Vogel, S. N., & Baker, A. J. 2010, ApJ, 708, 841

Welikala, N., Connolly, A. J., Hopkins, A. M., & Scranton, R. 2009, ApJ, 701, 994

Whitmore, B. C. 1995, in Astronomical Society of the Pacific Conference Series, Vol. 70, Groups of Galaxies, ed. O.-G. Richter & K. Borne, 41

Whitmore, B. C., Gilmore, D. M., & Jones, C. 1993, ApJ, 407, 489

Wilman, D. J., & Erwin, P. 2012, ApJ, 746, 160

Wyder, T. K., Martin, D. C., Schiminovich, D., et al. 2007, ApJS, 173, 293

Yang, Y., Zabludoff, A. I., Zaritsky, D., & Mihos, J. C. 2008, ApJ, 688, 945

York, D. G., Adelman, J., Anderson, Jr., J. E., et al. 2000, AJ, 120, 1579

Zaritsky, D., & Christlein, D. 2007, AJ, 134, 135

Zehavi, I., Patiri, S., & Zheng, Z. 2012, ApJ, 746, 145